TÉCNICO LISBOA

Mesons in a Covariant Constituent-Quark Formalism

Sofia Isabel Cardoso de Almeida Leitão

Dissertação para a obtenção do Grau de Mestre em

Engenharia Física Tecnológica

Júri

Presidente: Prof. Doutor Mário João Martins Pimenta
Orientador: Prof. Doutora Maria Teresa Haderer de la Peña Stadler
Coorientador: Prof. Doutor Alfred Stadler
Vogal: Prof. Doutor Jorge Manuel Rodrigues Crispim Romão
Vogal: Prof. Doutor Pedro José de Almeida Bicudo

Novembro 2012

Agradecimentos

Gostaria de agradecer aos meus orientadores, os Doutores Teresa Peña e Alfred Stadler pelo apoio que me deram no processo que foi elaborar esta tese. Igualmente pela constante disponibilidade que sempre para comigo tiveram, quer fosse para a discussão de um *avanço* ou de um *recuo*.

Dedico esta tese à minha querida família (a todos, sem excepção) e à pessoa que me fez perceber que o valor de um ser humano não está no resultado daquilo que faz, antes sim daquilo que não desiste de fazer.

Por último, agradeço ao mar pela sua imensidão, beleza e infinita paciência.

Resumo

Nesta tese são estudados um dos mais pequenos, ainda assim mais complexos, sistemas conhecidos na Natureza: os mesões. O grande interesse destes estudos teóricos sobre mesões advém de poderem permitir a identificação de possíveis estados exóticos nos resultados da actividade experimental já realizada ou planeada. Os mesões constituídos por quarks leves são sistemas relativistas e, por isso, o nosso objectivo é modelar estas partículas à luz de um formalismo covariante de quarks constituintes baseado na *Covariant Spectator Theory* (CST)-Teoria Covariante da Partícula Espectadora. Uma das características apelativas deste formalismo é a possibilidade de incorporar, simultânea e consistentemente, o confinamento e a quebra espontânea da simetria quiral.

Começamos por considerar os sistemas mesónicos com uma abordagem inteiramente não relativista através da equação de Schrödinger, onde são calculados os espectros de massa e funções de onda, para referência. Verificámos que a descrição não-relativista no sector de mesões com quarks pesados é válida. O estudo foi feito no espaço das configurações e posteriormente no espaço dos momentos, para um estado de momento angular arbitrário, pois o espaço dos momentos é o espaço natural para definir a energia cinética e interações relativistas. O aparecimento de singularidades no kernel das equações exigiu o desenvolvimento de técnicas originais e sofisticadas para a sua remoção, bem como a implementação de métodos numéricos que foram comparados e testados para alta precisão. Salienta-se que as técnicas de subtração apresentadas tornaram possível resolver o problema do confinamento no espaço dos momentos sem utilizar nos cálculos numéricos um parâmetro de blindagem ("*screening*"), como é pratica usual na literatura.

A metodologia desenvolvida no domínio não relativista é depois generalizada para o caso relativista, onde é resolvida a equação para a função de vértice de duas partículas (equação 1CS) através do uso de *splines*. Adicionalmente é mostrado o limite de uma partícula desta equação, tomando razões de massa sucessivamente maiores, o que reproduz os resultados da equação de Dirac para uma partícula. De forma análoga, ilustra-se a redução ao caso não-relativista da equação 1CS que, no limite das massas muito grandes, reproduz os resultados da equação de Schrödinger. A obtenção numérica deste limite fundamenta, pelos seus resultados, a generalização relativista da interação de confinamento escolhida.

Como conclusão, enumeram-se as principais aplicações do modelo e listam-se os aspectos a desenvolver, trabalho este que se encontra actualmente em curso.

Palavras-Chave: Mesões, Teoria de Campo Efectiva, Teoria Covariante da Partícula Espetadora (CST), Modelo de Gross & Milana, *Splines*.

Abstract

The objective of this thesis is a theoretical study of one of the smallest, yet rather complex, systems known in nature: the mesons.

Theoretical studies of mesonic states are of great interest, namely, for the identification of exotic mesons that may emerge from spectroscopic data collected in current and planned experimental activities. Mesons made of light quarks have to be described relativistically and in this work we study a particular covariant framework, the Covariant Spectator Theory (CST), and show how it is suitable for these studies since it incorporates consistently confinement and spontaneous chiral symmetry breaking.

We start by treating the mesons as valence quark-antiquark pairs interacting through a static potential, and we solve the corresponding nonrelativistic Schrödinger equation, for reference. We compute mass spectra and wave functions. This first set of calculations confirmed that a nonrelativistic description is adequate for the heavy mesonic sector, while it is not valid for mesons made of light quarks. Because relativistic kinetic energy and interactions are naturally given in momentum space, we perform those calculations in momentum space and for general angular momentum states, in preparation for the relativistic calculations. The momentum-space calculations have difficulties originated by singularities in the kernel. We introduced new numerical methods involving sophisticated subtraction methods which enable us to solve the linear confinement problem in momentum space without using a screening parameter – a common practice in the literature. We also implemented and compared powerful numerical methods aiming at high precision.

The definition of the confinement potential in the non-relativistic domain is then generalized to the relativistic case, where we solved the two-body spectator equation for the vertex function by applying the method of *splines*. Additionally, it is shown that the one-body limit of this equation is the Dirac equation, for the light quark moving in the presence of the infinitely heavy one, when one takes the ratio between the two constituent masses tend to infinity. It is also seen that results from the relativistic equation coincide with the non-relativistic Schrödinger results when both masses are very large. The success in obtaining this limit confirms that our choice for the relativistic generalization of the confinement interaction is robust.

Finally, the main applications of the model are described and procedures to improve upon the 1CS equation are presented. Some of these aspects are currently under development.

Keywords: Mesons, Effective Quantum Field Theory, Covariant Spectator Theory (CST), Gross & Milana's Model, *Splines*.

Contents

List of Figures

List of Tables

List of Abbreviations

GM Gross and Milana

CST Covariant Spectator Theory

LQCD Lattice Quantum Chromodynamics

QCD Quantum Chromodynamics

CQM Constituent-Quark Models

1CS One-channel two-body vertex spectator equation

2CS Two-channel two-body vertex spectator equation

Chapter 1

Introduction

'The journey from Kamakura to Kyoto takes twelve days. If you travel for eleven but stop with only one day remaining, how can you admire the moon over the capital?'
Writings of Nichiren Daishonin, p.1027

'Our treasure lies in the beehive of our knowledge. We are perpetually on the way thither, being by nature winged insects and honey gatherers of the mind.'
Friedrich Nietzsche

1.1 Motivation

The objective of this thesis is a theoretical study of one of the smallest, yet rather complex, systems known in nature: the mesons.

Mesons are hadronic particles composed of quarks and gluons, bound together by the strong interaction. Their study is interesting not only for the understanding of the effective nuclear force between nucleons in nuclei – which is in part interpreted as meson exchange processes – but also to get more insight into the unique properties of the elementary strong interaction. In fact, an open question of great importance is to understand the connection between the strong interaction acting between elementary quarks, as described by gluon exchange, and the emergence of confinement in hadrons. The answer to this question elucidates on how complex systems can be constructed from elementary ones. It should be emphasized that the confinement interaction has a unique many-body dynamics compared with the dynamics involved in the clustering of nucleons to nuclei or in the clustering of atoms to molecules. This is due to the self-interacting non-linear character of the gluons in non-abelian QCD. It is also worth mentioning that although QCD is believed to be the fundamental field theory of the strong interaction, because of the large value of its coupling constant in the low and medium energy regime, it becomes very difficult to solve it, because one cannot use perturbation theory. It is thus necessary to develop other approaches.

Our main and general motivation in this work is to create, in the near future, a unified and consistent relativistic model for mesons as quark-antiquark bound states that can be applied to both heavy and light mesons. The model should satisfy a number of important requirements: (i) the formalism used should be covariant, which is essential for the description of systems composed of light quarks; (ii) the quarks should be strictly confined; (iii) the structure and mass of the constituent quarks themselves, i.e., their self-energy, should be described consistently through the same confining interaction that acts between pairs of quarks; and (iv) the model should reflect the requirements of chiral symmetry (i.e. when the bare mass of a quark q_i approaches zero, a massless $q_i\bar{q}_i$ bound state must emerge).

In the process, knowledge on both the Dirac structure of the effective confinement interaction and the form of the low energy effective one-gluon-exchange interaction is to be gained.

This is of great interest because it will support the analysis of emerging spectroscopic data collected in current and planned experimental activities in Europe and in the USA, for a extensive search for exotic mesons, with a structure that is not reduced to a quark-antiquark pair. Moreover, there are two other possible applications that we can highlight: i) the computation of the pion transition form factor, a necessary input for the hadronic contribution to the anomalous magnetic moment of the muon, which is nowadays being investigated for possible signs of Physics beyond the Standard Model ref.[1]; ii) the production of lepton pairs whose precise knowledge is mandatory in the search for the quark-gluon plasma ref.[2].

In this thesis we will use the Covariant Spectator Theory (CST) formalism (ref.[4], [5], [6]). CST is based on Relativistic Quantum Field Theory which has been widely and very successfully used in different types of few-body systems, namely problems involving few nucleons. For a recent review of the CST theory one should see ref.[7]. CST has unique properties since it is entirely covariant and allows us to the treat confinement and spontaneous breaking of chiral symmetry in a consistent way.

In a work called "Covariant, chirally symmetric model of mesons" (ref.[3]), labeled as GM model throughout this dissertation, Gross and Milana applied it for the first time to the study of mesons. The work was ideally thought to describe all the mesonic spectrum, from the π to the Υ, providing a robust and useful theoretical basis in which interesting mesonic properties can be computed. However, in the numerical calculations performed so far, the constituent quark mass has been treated as a constant (ref.[3, 8, 9]) or as a phenomenological function not related to the kernel (ref.[10]). On of our aims is to correct this deficiency in future work.

This thesis is constructed in a "step-by-step" way, without avoiding any technical numerical difficulties which arise very quickly, even in simpler approaches than the GM model, and by treating them extensively and testing the numerical methods. Finding new and more efficient solutions to some of these technical difficulties is one of the major contributions of this thesis which, undoubtedly, serves as the unavoidable preparatory work to establish, in the near future, a code for reliable predictions of masses of pure $q\bar{q}$ pairs, which is in order for a definite identification of hybrid states.

1.2 From the Yukawa's prediction to present day challenges

Figure 1.1: Hideki Yukawa.*"Suppose there is something which a person cannot understand. He happens to notice the similarity of this something to some other thing which he understands quite well. By comparing them he may come to understand the thing which he could not understand up to that moment. If his understanding turns out to be appropriate and nobody else has ever come to such an understanding, he can claim that his thinking was really creative".* Creativity and Intuition: A Physicist Looks at East and West (1973), p.144.

For many ages, an important aim of science has been to explain the phenomena we observe in terms of the properties of fundamental particles. In modern physics this problem is still crucially importance [1]. During the last sixty, seventy years, particles called "mesons" turned out to be particularly interesting. The mesons are particles heavier than the electrons but lighter than the nuclei of the hydrogen atoms, i.e. the protons.

The mesons were entirely unknown until Hideki Yukawa in 1934 predicted their existence on the basis of a theoretical investigation of the nuclear forces. This achievement brought him the Nobel Prize in Physics in 1949.

From earlier research by Heisenberg and others one knew that an atomic nucleus, i.e. the central core of an atom, was composed of protons and other particles which have the same mass as the protons but no charge, the neutrons. These building blocks of the atomic nuclei were called "nucleons" and were held together by the so-called nuclear forces.

Attacking the problem of the origin and nature of those forces, which are of short-range, Yukawa used the electromagnetic field as a model. He found that this field could be modified so as to give forces which have a short range. He therefore assumed that the new field corresponded to the nuclear forces. Each field of force is, according to modern theories, associated with some kind of particles. Yukawa discovered that there was a simple relation between the range of these forces and the mass of the corresponding particles. However, the name of "mesons" for these particles was not introduced until later.

Specifically for the strong nuclear force, Yukawa proposed that an unknown particle, now called a **pion**, was exchanged between nucleons, transmitting the force between them. The pion has mass, and therefore an energy $\Delta E = mc^2$, and can only be created in a virtual process occurring for a sufficiently short period of time, given by the Heisenberg uncertainty principle

$$\Delta E \Delta t \geq \frac{h}{4\pi}, \tag{1.1}$$

The larger the mass, the greater ΔE, and the shorter is the time Δt during which it can exist. This means that the range of the force is limited, because the particle can only travel a finite distance in

[1] Nowadays, one of the most thrilling breakthroughs of Physics is just taking place in the LHC in CERN, with the discovery of the Higgs boson, predicted by Peter Higgs in ref.[11].

a finite amount of time. In fact, the maximum distance is $d \approx c\Delta t$, where c is the speed of light. So taking the range of the strong nuclear force to be about 1 fermi $(10^{-15}m)$, the time during which the pion exists is approximately:

$$\Delta t \approx \frac{d}{c} = \frac{10^{-15}m}{3.0 \times 10^{8}\, ms^{-1}} \approx 3.3 \times 10^{-24}s \tag{1.2}$$

and ΔE is

$$\Delta E \approx \frac{6.63 \times 10^{-34} J.s}{4\pi\,(3.3 \times 10^{-24}s)}. \tag{1.3}$$

Solving this and converting the energy to MeV gives

$$\Delta E \approx \left(1.6 \times 10^{-11} J\right) \frac{1MeV}{1.6 \times 10^{-13} J} = 100MeV \tag{1.4}$$

and so the mass of the pion should be of the order of

$$m \approx 100MeV/c^2. \tag{1.5}$$

This is about 200 times the mass of an electron and about one-tenth the mass of a nucleon. No such particles were known at the time Yukawa made his bold proposal, and one pertinent question that arose then was how its existence could be verified if the pion, being a virtual particle, was impossible to be seen directly? The answer is that if a sufficient amount of energy was transfered to the nucleus, it should be possible, in principle, to free the pion, that is, to create its mass from an external energy input. This could be accomplished by collisions of energetic particles with nuclei, but energies greater than 100 MeV were required to conserve both energy and momentum. At the time Yukawa thought about it and emphasized that these particles were expected to appear in the cosmic radiation, in which particles of great energy had been previously found.

His prediction turned out to be correct and, in 1937, the study of the cosmic radiation gave the first experimental evidence of the existence of mesons. This evidence was given by Anderson and Neddermeyer ref.[12] and other American physicists. Since that time, the mesons in the cosmic radiation have been studied. These investigations have been guided by the theory of Yukawa. A new period in meson research began about three years later. The British physicist Powell and his collaborators ref.[13] then found that there existed two kinds of mesons. The mesons of one kind were those found in 1937, whereas the mesons of the other kind were somewhat heavier and different also in other aspects.

These experimental investigations have shown that the masses of both kinds of mesons agree with Yukawa's prediction as far as the order of magnitude is concerned. The heavier mesons, but not the lighter ones (which are in reality muons), had an interaction with the nucleons about as strong as Yukawa had postulated. The fact that particles of this kind have been found experimentally provided a brilliant vindication of Yukawa's fundamental ideas. The electric charge of both kinds of mesons agreed with Yukawa's prediction. It had also been experimentally confirmed, that the mesons could exist only for a very short time. A heavy meson lives only for about one hundredth of a millionth of a second and is then transformed into a light meson and probably a neutrino.

Soon afterward, accelerators of sufficient energy were creating pions, and other mesons, in the laboratory under controlled conditions.

From its early prediction in 1934 until today, our knowledge of the mesons has evolved significantly. In fact, now the mesons are classified as hadronic systems composed by quarks and antiquarks, and gluons, bound together by the strong interaction. Their study is interesting not only for the understanding of the nuclear force (just as Yukawa predicted, mesons are the mediators of the nuclear

force), but also to get more insight about the unique properties of the strong interaction, since meson structure and spectrum is determined by the form of the confinement interaction, not exactly known yet in detail.

The study of mesonic properties is carried out following roughly two main complementary theoretical approaches. The first one starts from the basic quark and gluon degrees of freedom, whose interaction is described by the accepted framework of QCD. To go beyond a perturbative approach a big theoretical effort is nowadays devoted to the understanding of the hadron structure using LQCD calculations. This is a numerical approach that discretizes the evolution equations of QCD on a four-dimensional space-time lattice space and solves them by means of Monte Carlo techniques. Here, many important results have been obtained and more are expected in the future by the use of more powerful computers. Nevertheless, the goal of simulations corresponding to the physical small pion masses presumably will still require some time, and in the meanwhile one has to rely on models, eventually based on QCD or LQCD.

The second approach, which can be denoted as "phenomenological", predicts hadron properties that are "built" from theoretical frameworks based on general parameterizations of quarks and gluons dynamics. The idea of quarks as constituent particles of hadrons was introduced in the 60's, before their experimental discovery. A large variety of models have been built and applied to describe hadron properties. An important class is provided by CQM [2], in which quarks are considered as effective internal degrees of freedom.

The modern version of the nonrelativistic CQM considers a confinement potential characterized by a Coulomb-like term and a linear one, which is inspired on lattice calculations. In the last years, CQM have been considerably refined to include further elements, related to spin-orbit, spin-spin and tensor interactions, and in spite of their simplicity, they can feature a fairly good agreement with the experimental results. In general, the different theoretical approaches are not sharply separated. On the contrary, they are strongly interconnected.

Due to the non-Abelian characteristic of the strong interaction, also gluons are self-interacting carriers of the force, which causes a very rich variety of hadron structures. Glueballs made entirely of gluons, hybrids consisting on a $q\bar{q}$ pair combined to an excited gluon, or multi-quarks states exist. A clear and unambiguous observation of these states will be an important confirmation of the validity of the theoretical framework. However, there is still much to be learned in descriptions of pure $q\bar{q}$ states, for solid steps into the knowledge of hybrids.

It is crucial to have good experimental results that open the door to a better understanding of the systems under consideration.

The majority of results gathered until now have been obtained using e^+e^- colliders in experiments like BaBar (Stanford), Belle (KEK), BES (Beijing), CLEO (Cornell). These, on one hand, have determined big progresses in the field, while, on the other hand, have discovered a large number of states with properties that cannot be easily and exhaustively explained by any theory.

There are essentially two main active areas of research:

- Exotic States in the low energy regime;
- Heavy Mesons in the high energy domain.

Considering the first one, one of the first claim for the existence of a non $q\bar{q}$ meson, namely a 1^{-+} resonance, was made by the BNL experiment E852 (ref.[14]). Similar results and confirmations were then obtained by other experiments, for example in a recent paper from the COMPASS collaboration (ref.[15]).

In order to overcome the limitations arising in the low energy region, the spectroscopy activity has moved to higher energies. Large data sets have been collected at e^+e^- machines by BaBar, Belle,

[2] GM model belongs to this category.

CLEO, and BES collaborations, but also the Tevatron experiments, CDF and D0, have contributed significantly. Plenty of mesons of both kinds have been produced at e^+e^- machines studying different processes:

- B-meson decays;
- inclusive charmonium (bottomonium) production;
- associate charmonium production;
- two photon collisions;
- initial state radiation.

In the near future, besides e^+e^- experiments other type of machines namely, hadronic machines such as the LHC, will provide other results. While LHCb has been designed with the intention of performing spectroscopic studies; ALICE, ATLAS and CMS can also provide additional results.

For the low energy region (below 2 GeV) a new set of data will be provided by the GlueX experimental program (ref.[16]), foreseen for the upgraded 12 GeV JLAB machine.

Finally, probably the most ambitious and complete spectroscopy future project is represented by the PANDA (ref.[17]) experiment at FAIR (ref.[18]). FAIR is a new international Facility for Antiproton and Ion Research under construction at GSI. In PANDA, a wide scientific program including meson spectroscopy from light to charm quark sector, baryon/antibaryon production, charm in nuclei, and strangeness physics with particular attention to the systems with strangeness $S = -2$, will be carry out. Antiproton-proton annihilations have proven to produce large quantities of exotic states (ref.[19, 20]) with yields comparable to ordinary mesons. This is due to the fact that the annihilation process create highly dense matter where gluons proliferate and multiply.

Chapter 2

Nonrelativistic calculation of the meson spectra

'Sometimes attaining the deepest familiarity with a question is our best substitute for actually having the answer.'
Brian Greene

In this chapter we will start with a very simple approach to the problem of modeling mesons: we will treat them as simple valence quark-antiquark pairs interacting through a static potential in a nonrelativistic regime. We are interested in computing the wavefunctions, the binding energies and the corresponding mass spectra and, in order to do so, we will solve the familiar Nonrelativistic Schrödinger Equation (NRSE). Already from such a relatively simple analysis, a number of interesting conclusions can be drawn. But the main purpose of this study is that it serves as preparation for later, more advanced calculations: by testing various numerical techniques in a more easily controlled nonrelativistic environment it lays the groundwork for applications of the most successful numerical methods in the more complicated, relativistic framework of the Covariant Spectator Theory.

The first natural question that arises when one proposes this type of description is whether it is reasonable at all to describe mesons nonrelativistically, and if so in what energy regime. So, before we proceed we will discuss this point by means of a simple estimate:

We can imagine, in a somewhat crude approximation, a meson as some kind of "confining" sphere inside of which the constituent quark and the antiquark can move freely, but from which they cannot escape. This way, the momentum and the position of a quark (antiquark) inside the meson are of the order of

$$\begin{aligned} p &= \bar{p} \pm \Delta p \\ x &= \bar{x} \pm \Delta x \end{aligned}, \tag{2.1}$$

where the bar on top of the variable means its average value and Δ its uncertainty. If we place the origin of our reference frame in the meson sphere's center, the average momentum and position are zero, so the order of magnitude is given by the respective uncertainties only:

$$\begin{aligned} p &\approx \Delta p \\ x &\approx \Delta x \equiv R, \end{aligned} \tag{2.2}$$

where the uncertainty of the quark's position was identified with the "characteristic size" R of the meson, in this case the radius of the corresponding sphere.

Considering now the Uncertainty Principle,

$$\Delta x \Delta p \sim h\,, \tag{2.3}$$

we find the following relation:

$$p = \frac{h}{R}. \tag{2.4}$$

Relativistic effects become important when a particle's kinetic energy is no longer negligible compared to the energy of its rest mass. So we have to find out under which conditions $p^2/2m$ becomes comparable with mc^2. Using the above estimate for the momentum we find

$$\frac{p^2}{2m} = \frac{h^2}{2mR^2} \sim mc^2 \quad \text{if} \quad R^2 \sim \frac{h^2}{2m^2c^2}\,.$$

Taking into account that an increasing radius R leads to a decrease of the kinetic energy, and neglecting the unimportant factor of 2, we can express our result in terms of the Compton wavelength $\lambda_C = h/mc$ as follows:

- if $R \gg \lambda_C$, relativistic effects will not be very important;
- if $R \sim \lambda_C$, relativistic effects are not negligible;
- if $R \ll \lambda_C$, relativistic effects are large.

Here we have to distinguish between the *current* or *bare* mass m_0, which refers to the mass of the quark (antiquark) by itself, and the *constituent* mass m that refers to the current quark (antiquark) mass plus the mass of the gluon fields surrounding it. An estimate of the *constituent* quark mass can be found of by dividing the mass of a known meson by 2 or the mass of a nucleon by 3.

As a rough estimate for the typical size of a meson we can use

$$R \sim 1\,fm\,. \tag{2.5}$$

quark	m_0 (MeV/c^2)
u	2.4
d	4.8
s	104
c	1270
b	4200
t	171200

Table 2.1: Bare quark masses ref.[22].

Comparing the values of tables 2.1 and 2.2 one notes that for the heavy-meson sector (cases c and b), the constituent quark mass is closer to the bare quark mass than for the lighter sector (cases u, d, and s), thus reflecting the larger "dressing" effects present in the latter.

We also see that the Compton wavelengths of u, d, s quarks (and antiquarks, which have the same mass) are clearly larger than their characteristic size, and relativistic effects are important. The b, and t [1] quarks have considerably smaller Compton wavelengths, which—according to our simple estimate—allows us to treat them in a nonrelativistic approximation. The $c\bar{c}$ mesons are in the transition zone, where moderate relativistic effects may be noticeable. However, they are usually also treated as nonrelativistic systems.

[1] We did not consider the case $t\bar{t}$ because it has a very reduced probability of appearing in Nature, as discussed in ref. [23]. This is due to the very short lifetime of these particles that decay almost immediately after being produced.

Particle	q	$m_h\ (MeV/c^2)$	$m_q\ (MeV/c^2)$	$\lambda_C(fm)$
$n(uud)$	u	938.2	312.3	3.973
$n(udd)$	d	939.6	313.7	3.955
$\phi(s\bar{s})$	s	1020	610	2.034
$J/\psi(c\bar{c})$	c	3096.2	1548.1	0.8014
$\Upsilon(b\bar{b})$	b	9460.4	4730.2	0.2623

Table 2.2: Constituent quark masses m_q and corresponding Compton wavelengths λ_C for the quarks. In the first and third columns we indicate the hadron and its mass m_h (ref.[22]), from which we estimated the constituent quark mass.

2.1 Solving the NRSE in r-space

The starting point for calculating the wavefunctions and eigenvalues of quarkonium states is the time-independent Nonrelativistic Schrödinger Equation (NRSE) with a central potential:

$$H = \frac{p_1^2}{2m_1} + \frac{p_2^2}{2m_2} + V_0\left(|\vec{r}_1 - \vec{r}_2|\right) = \frac{P^2}{2M} + \frac{p^2}{2\mu} + V_0\left(|\vec{r}|\right) = H_{cm} + H_{rel} \tag{2.6}$$

where we have separated the relative motion Hamiltonean H_{rel} from the center of mass Hamiltonean H_{cm}:

$$\begin{aligned} H_{cm} &= \frac{P^2}{2M}, & H_{rel} &= \frac{p^2}{2\mu} + V_0\left(|\vec{r}|\right), \\ P &= p_1 + p_2, & p &= \frac{m_1 p_1 - m_2 p_2}{m_1 + m_2}, \\ \vec{R} &= \frac{m_1\vec{r}_1 - m_2\vec{r}_2}{m_1 + m_2}, & \vec{r} &= \vec{r}_1 - \vec{r}_2, \\ M &= m_1 + m_2, & \mu &= \frac{m_1 m_2}{m_1 + m_2}. \end{aligned} \tag{2.7}$$

and $m_1 \equiv m_{q_i}$ and $m_2 \equiv m_{\bar{q}_j}$, for $i,\ j = u,d,s,c,b,t$.

In the center-of-mass frame, one obtains the coordinate space Schrödinger equation for the relative motion only:

$$\left[-\frac{\nabla^2}{2\mu} + V_o(r)\right]\psi(\vec{r}) = E\psi(\vec{r}). \tag{2.8}$$

For a radially symmetric potential the wavefunctions written in spherical coordinates are:

$$\psi(r,\theta,\phi) = R_{nl}(r)Y_{lm}(\theta,\phi). \tag{2.9}$$

The radial wavefunctions satisfy the equation

$$\left[-\frac{1}{2\mu}\left(\frac{\partial^2}{\partial r^2} + \frac{2}{r}\frac{\partial}{\partial r}\right) + \frac{l\,(l+1)}{2\mu r^2} + V_0(r)\right]R_{nl}(r) = E_{nl}R_{nl}(r). \tag{2.10}$$

We introduce as usual the reduced radial wavefunction

$$u_{nl}(r) = rR_{nl}(r), \tag{2.11}$$

that are solutions of

$$\left[-\frac{1}{2\mu}\frac{d^2}{dr^2}+\frac{l(l+1)}{2\mu r^2}+V_0(r)\right]u_{nl}(r)=E_{nl}u_{nl}(r), \tag{2.12}$$

with the normalization condition

$$\begin{aligned}\int d^3r\,|\psi(\vec{r})|^2 &= \int d\Omega dr r^2\,(R_{nl}(r))^2\,|Y_{ml}(\theta,\phi)|^2=1,\\ \int dr r^2\,(R_{nl}(r))^2 &= \int dr\,(u_{nl}(r))^2=1.\end{aligned} \tag{2.13}$$

2.1.1 The Coulomb-plus-Linear Potential

Various quark interaction models have been used over the years. In the region tested by experiments most of these models coincide, in their general form. Some models are purely phenomenological (e.g. ref.[28]) and others are guided by perturbative QCD for its short-range part. Since color charges are subject to confinement, a phenomenological long-range part has to be added to account for confinement (e.g. see ref.[29],[30]). Indeed, in the limit of static quarks, the quark-anti-quark potential from Nambu-Bethe-Salpeter amplitudes obtained in lattice QCD simulations suggest that the interquark potential has a linear behaviour at large separation distances r (e.g. ref.[31]).

One of the most commonly used potentials is therefore the so called Coulomb-plus-Linear potential. The leading term of the quark-antiquark potential arising from a perturbative QCD calculation is essentially Coulomb-like

$$V_{0,pert}(r)=-\frac{4\alpha_s}{3r}, \tag{2.14}$$

and the $\frac{4}{3}$ factor comes from the color interaction.

For large distances, however,

$$V_{conf}(r)=\sigma r, \tag{2.15}$$

is expected to be a reasonable choice for the long range part of the potential. The potential we use in Eq.2.12 to obtain eigenvalues and wavefunctions for the $q\bar{q}$ bound states will then be given by the Coulomb-plus-Linear potential

$$V_0(r)=V_{0,pert}(r)+V_{conf}(r)+C=-\frac{4\alpha_s}{3r}+\sigma r+C. \tag{2.16}$$

The Coulomb-plus-linear potential (Fig.2.1), sometimes referred to as Cornell potential or funnel potential, has first been proposed by the Cornell group (ref.[29],[30],[32]) to reproduce the charmonium spectrum.

According to a recent LQCD lattice calculation (ref.[24]),

$$V(r)=-\frac{A}{r}+\sigma r, \qquad A=0.26, \qquad \sigma=0.89\,GeV/fm, \qquad C=0. \tag{2.17}$$

We explore in the next sections the two limiting cases of the Cornell potential: the Pure Linear Potential and the Pure Coulomb-type Potential.

Pure Linear potential

We start with a pure linear potential of the form

$$V(r)=\sigma r. \tag{2.18}$$

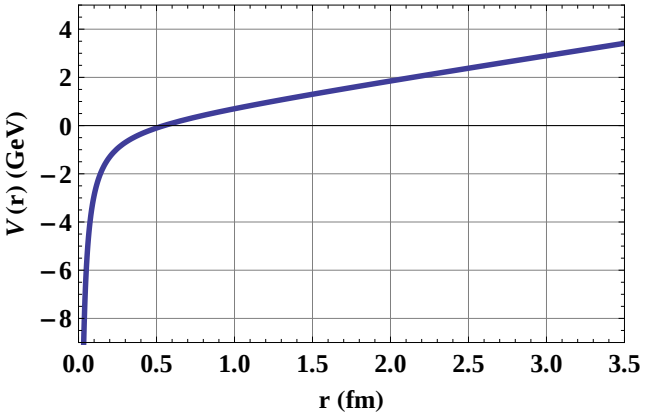

Figure 2.1: Coulomb-plus-Linear Potential with parameters $\alpha_s = 0.3$, $\sigma = 1.0 GeV/fm$.

Setting

$$\rho = r\left(\frac{1}{2\mu\sigma}\right)^{-1/3} \qquad \text{and} \qquad \varepsilon_{nl} = \frac{E_{nl}}{\sigma}\left(\frac{1}{2\mu\sigma}\right)^{-1/3} \tag{2.19}$$

leads to the dimensionless equation

$$-\frac{d^2u_{nl}}{d\rho^2} + \left[\frac{l(l+1)}{\rho^2} + \rho\right] u_{nl} = \varepsilon_{nl} u_{nl}\,. \tag{2.20}$$

The boundary conditions imposed are that the wavefunction vanishes at the origin and at infinity, i.e.,

$$u_{nl}(\rho = 0) = 0, \qquad u_{nl}(\rho = \infty) = 0. \tag{2.21}$$

For the s-wave ($l = 0$) case, Eq.2.20 reduces to

$$-\frac{d^2u_{nl}}{d\rho^2} + \rho u_{nl} = \varepsilon_{nl} u_{nl} \tag{2.22}$$

that has the following analytic solution:

$$u_{l=0}(\rho) = Ai(\rho - \varepsilon), \tag{2.23}$$

where Ai is the well-known regular Airy function. The binding energies are:

$$\varepsilon_{l=0} = -z_n, \tag{2.24}$$

and z_n, for n=1,2,3.. are the zeros of the Airy function Ai.

For $l \neq 0$; there is not an analytic solution, so we have to solve Eq.2.20 numerically. The procedure is explained in Appendix C.

Pure Coulomb-type potential

This case is also interesting because it is very similar to the familiar problem of solving the Schrödinger equation for the hydrogen atom, where the potential is given (in SI units) by:

$$V(r) = -\frac{e^2}{4\pi\varepsilon_0}\frac{1}{r}. \tag{2.25}$$

The NRSE for the hydrogen atom is[2]

$$-\frac{\hbar^2}{2\mu}\frac{d^2}{dr^2} + \left[-\frac{e^2}{4\pi\varepsilon_0}\frac{1}{r} + \frac{\hbar^2}{2\mu}\frac{l(l+1)}{r^2}\right] u = Eu\,. \tag{2.26}$$

Setting

$$\kappa \equiv \frac{\sqrt{-2\mu E}}{\hbar}, \qquad \rho \equiv \kappa r, \qquad \rho_0 \equiv \frac{\mu e^2}{2\pi\varepsilon_0\kappa} \tag{2.27}$$

we find the dimensionless equation

$$\frac{d^2u_{nl}}{d\rho^2} = \left[1 - \frac{\rho_0}{\rho} + \frac{l(l+1)}{\rho^2}\right] u_{nl}\,. \tag{2.28}$$

Once again, in order to solve this equation we used the method explained in Appendix C.

2.1.2 Results

In the case of a pure linear potential, table 2.3 shows our numerical results for the first 3 partial waves, and in each case for the lowest 5 energy states. The s-wave results are compared to the exact solutions, and one can see that they match for the first 3 states up to the sixth decimal place. As expected, the agreement deteriorates for the higher excited states, but globally our numerical method appears to be efficient.

The corresponding wavefunctions are displayed in figs. 2.2–2.5. We make the following observations:

1. They show the usual pattern that each step higher in the radial excitation level n increases the number of nodes in the wavefunction by one; the appearance of nodes makes different radial states orthogonal, as they should.

2. Fig.2.5 exhibits clearly that for a given radial excitation n the wavefunction components corresponding to increasing values of angular momentum l extend to larger and larger distances in configuration space, confirming that the higher l the more peripheral a state is.

The calculations of the energy levels of the hydrogen atom served to test the accuracy of our method for higher partial waves than $l = 0$. This pure Coulomb case is convenient because all energy levels are known analytically. We see from table 2.4 that the agreement of our numerical results with the exact ones is not as good as for the linear potential, but they are still satisfactory for the level of accuracy we are interested in. We can conclude that our method is reliable also for higher partial waves. For the case of the interaction between quarks in a meson, the Coulomb potential has its

[2]Here μ is the reduced mass of the electron-proton system. In the meson problem μ is the reduced mass of the $q\bar{q}$ pair.

origin not in the electromagnetic but in the strong interaction. The corresponding NRSE is obtained by simply replacing $-\frac{e^2}{4\pi\varepsilon_0} \to A$, where A is a constant describing the strength of the potential.

Next, in tables 2.5, 2.6 and 2.7 we make a comparison between our predicted meson masses and the experimental observed ones. The mass spectrum was obtained from the eigenvalues through the relation valid for the linear potential case:

$$M_{meson} = m_{q_i} + m_{\bar{q}_j} + E_{nl} = m_{q_i} + m_{\bar{q}_j} + \varepsilon_{nl}\sigma \left(\frac{\hbar^2}{2\mu\sigma}\right)^{1/3}. \tag{2.29}$$

Naturally, some states cannot be predicted from our simple model because it does not include any treatment of the spin or isospin dependence of the interation, neither any other fine structure effects. For instance, we cannot distinguish between a 1^1S_0 state (corresponding to $\eta_c(1S)$), from a 1^3S_1 state (corresponding to $J/\Psi(1S)$).

To overcome this, and in order to make a comparison between our predictions and the experimental results, we grouped mesons with the same radial-n and angular momentum l-states together and represented them as an "average meson" with a mass and a width taken as the mean and the standard deviation of the meson masses in the group. We define Δ as the relative difference of our predictions from this "averaged" meson (meson*), which is labeled by its spectroscopic features, $1S_{exp}$,$1P_{exp}$, $2P_{exp}$, etc. ...

The pure linear potential parameters could be fixed by performing a fit to each flavor case, by the least mean squares method. We obtained:

- bottomonium: σ=0.18GeV/fm
- charmonium: σ=0.154GeV/fm;
- mixed-flavor mesons ($b\bar{c}$, $b\bar{s}$, $c\bar{s}$): σ=0.179GeV/fm,

The results obtained show that the agreement with experiments worsens for the mesons composed of lighter quarks. For the bottomonium the deviations are always less than 4% whereas for the mesons of charm+strange type the deviations may reach 40%. It is also worth noticing that we have different σ parameters for different flavor cases, but, at the same time, the heavy meson sector is expected not to be sensitive to the linear part of the potential since the heavy mesons are deeply bound. Is there a contradiction? No, because our calculations did not include the Coulomb-like potential or funnel behavior, and this interaction term is increasingly important as the quarks get heavier. Thus, the varying slope of the Coulomb-like potential, as one goes nearer and nearer the origin $r \approx 0$, can only be "mocked" up with different linear potentials. Naturally, the largest slope σ is found for the bottomonium case, the most strongly bound meson. The lesson to be learnt is that the heavy-meson spectrum is not suitable to fix the confinement strength alone. The Coulomb-like part is to be included in the interaction, and importantly, the light meson sector has to be considered in the fit. For this a relativistic treatment is unavoidable, as we discussed already.

Eigenvalue	Exact	$l=0$	$l=1$	$l=2$
ε_{1l}	2.338107	2.338107	3.361254	4.248182
ε_{2l}	4.087949	4.087949	4.884452	5.629709
ε_{3l}	5.520560	5.520560	6.207632	6.868961
ε_{4l}	6.786708	6.786793	7.406265	8.012763
ε_{5l}	7.944134	7.947376	8.528377	9.117374

Table 2.3: Results for the eigenvalues ε_{n0} of the NRSE in configuration space with a linear potential. The column labeled "Exact" for $l=0$ shows the zeros of the Airy function (with the opposite sign), the other results were calculated numerically with the method described in Appendix C, for a mesh of 2000 points.

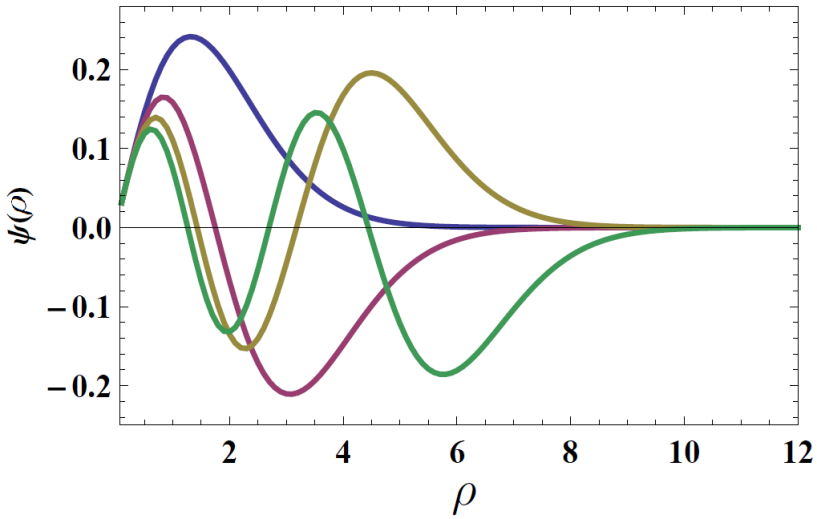

Figure 2.2: Wavefunctions of the first four $l=0$ energy states of the NRSE equation with a pure linear potential. The blue line represents the case $n=1$, red $n=2$, yellow $n=3$, and green $n=4$. The parameters used were: $\sigma = 1.0\,GeV/fm$ and $m_1 = m_2 = m_b = 4.65 GeV/c^2$.

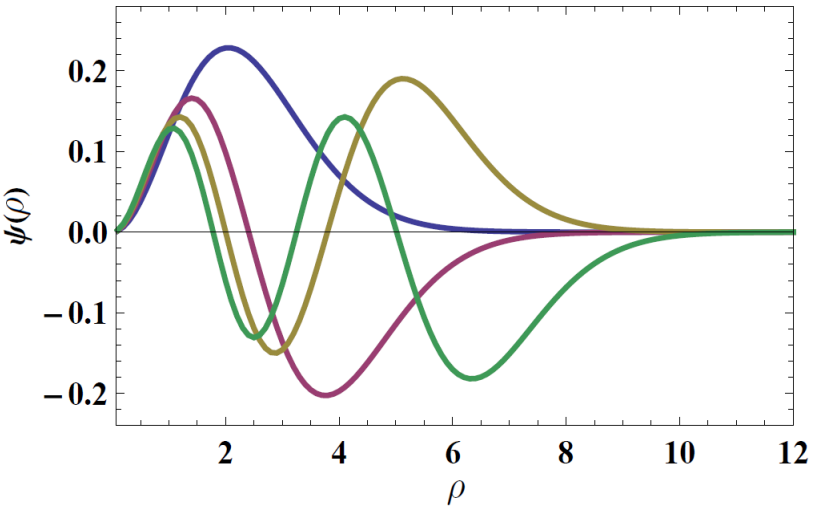

Figure 2.3: Wavefunctions of the first four $l=1$ energy states of the NRSE equation with a pure linear potential. The blue line represents the case $n=1$, red $n=2$, yellow $n=3$, and green $n=4$. The parameters used were: $\sigma = 1.0\,GeV/fm$ and $m_1 = m_2 = m_b = 4.65 GeV/c^2$.

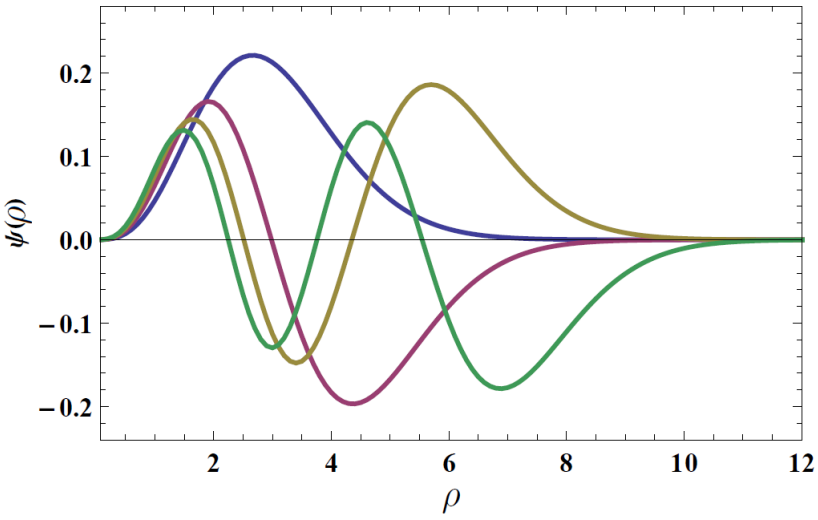

Figure 2.4: Wavefunctions of the first four $l = 0$ energy states of the NRSE equation with a pure linear potential. The blue line represents the case $n = 1$, red $n = 2$, yellow $n = 3$, and green $n = 4$. The parameters used were: $\sigma = 1.0\,GeV/fm$ and $m_1 = m_2 = m_b = 4.65 GeV/c^2$.

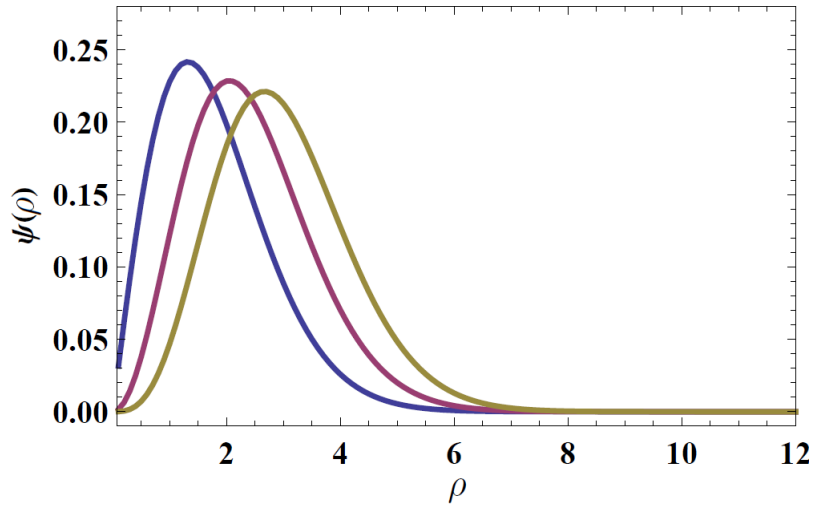

Figure 2.5: Comparison of the wavefunctions with $n = 1$ for $l = 0$ $l = 1$ and $l = 2$ (from left to right). The parameters used were: $\sigma = 1.0\,GeV/fm$ and $m_1 = m_2 = m_b = 4.65 GeV/c^2$.

E_i (eV)	$l=0$	$l=1$	$l=2$	$l=0$	$l=1$	$l=2$
E_1	-13.6057	-	-	-13.6066	-	-
E_2	-3.04142	-3.04142	-	-3.04165	-3.04166	-
E_3	-1.51174	-1.51174	-1.51174	-1.51185	-1.51184	-1.51185
E_4	-0.85036	-0.85036	-0.85036	-0.85041	-0.85042	-0.85042
E_5	-0.54423	-0.54423	-0.54423	-0.54466	-0.54468	-0.54462

Table 2.4: Results of the NRSE in configuration space with a Coulomb potential. The energy levels are calculated for the hydrogen atom. On the left side we list the exact values (see ref.[21]) and on the right our numerical results.

Meson (ref. [26])	$m_{exp.}(GeV/c^2)$	*Meson*$*$	$m_{exp.}(GeV/c^2)$	$m_{pred.}(GeV/c^2)$	$\Delta(\%)$
$\eta_b(1S)$	9.3909 ± 0.0003				
$\Upsilon(1S)$	9.4603 ± 0.0003	$1S_{exp}$	9.4256 ± 0.0347	9.7560	3.5
$\chi_{b_0}(1P)$	9.8594 ± 0.0004				
$\chi_{b_1}(1P)$	9.89828 ± 0.00026				
$h_b(1P)$	9.8986 ± 0.0014	$1P_{exp}$	9.89212 ± 0.03272	9.9555	0.6
$\chi_{b_2}(1P)$	9.9122 ± 0.0003				
$\Upsilon(2S)$	10.0233 ± 0.0003	$2S_{exp}$	10.0233 ± 0.0003	10.0972	0.3
$\Upsilon(1D)$	10.1637 ± 0.0014	$1D_{exp}$	10.1637 ± 0.0014	10.1285	0.7
$\chi_{b_0}(2P)$	10.2325 ± 0.0040				
$\chi_{b_1}(2P)$	10.25546 ± 0.0002	$2P_{exp}$	10.2522 ± 0.4	10.5106	2.5
$\chi_{b_2}(2P)$	1.026865 ± 0.0002				
$\Upsilon(3S)$	10.3552 ± 0.0050	$3S_{exp}$	10.3552 ± 0.0050	10.3766	0.2
$\Upsilon(4S)/\Upsilon(10580)$	10.5794 ± 0.0012				
$\Upsilon(10860)$	10.876 ± 0.011	$3S_{exp}$	10.8211 ± 0.2417	10.6236	1.8
$\Upsilon(11020)$	11.019 ± 0.008				

Table 2.5: Experimental mass spectra of bottomonium (mesons composed of $b\bar{b}$).

Meson (ref.[26])	$m_{exp.}(GeV/c^2)$	*Meson*$*$	$m_{exp.}(GeV/c^2)$	$m_{pred.}(GeV/c^2)$	$\Delta(\%)$
$\eta_c(1S)$	2.981 ± 0.0001				
$J/\psi(1S)$	3.096916 ± 0.000001	$1S_{exp}$	3.0390 ± 0.0580	3.1691	4.2
$\chi_{c_0}(1P)$	3.41475 ± 0.00031				
$\chi_{c_1}(1P)$	3.51066 ± 0.00007				
$h_c(1P)$	3.52541 ± 0.00016	$1P_{exp}$	3.50176 ± 0.08701	3.44002	1.8
$\chi_{c_2}(1P)$	3.5562 ± 0.0001				
$\eta_c(2S)$	3.6389 ± 0.0013				
$\psi(2S)$	3.686109 ± 0.000130	$2S_{exp}$	3.662505 ± 0.023605	3.63244	0.8
$\psi(3770)$	3.77315 ± 0.00033	?			
$\chi_{c_2}(2P)$	3.9272 ± 0.0026	$2S_{exp}$	3.850175 ± 0.07703	3.843340	0.2
$\psi(4040)$	4.039 ± 0.001	?			
$\psi(4160)$	4.153 ± 0.003	? $3P_{exp}$	4.096 ± 0.057	4.0118	2.1
$X(4260)$	4.253 ± 0.009	?			
$X(4360)$	4.361 ± 0.013	?			
$\psi(4415)$	4.421 ± 0.004	?			
$X(4660)$	4.664 ± 0.012	?			

Table 2.6: Experimental mass spectra of charmonium (mesons composed of $c\bar{c}$).

Meson (ref.[26])	$m_{exp.}(GeV/c^2)$	*Meson*$*$	$m_{exp.}(GeV/c^2)$	$m_{pred.}(GeV/c^2)$	$\Delta(\%)$
bottom+charm					
$B_c^{\pm}$	6.277 ± 0.006	$B\bar{c}_{exp}$	6.277 ± 0.006	6.668	5.9
bottom+strange					
B_s^0	5.36677 ± 0.00024				
B_s^*	5.4154 ± 0.0023	$B\bar{s}_{exp}$	5.613 ± 0.246	6.386	12.1
$B_{s1}^0(5830)$	5.8294 ± 0.0007				
$B_{s2}^{*0}(5840)$	5.8397 ± 0.0006				
charm+strange					
$D_s^{\pm}$	1.96849 ± 0.00032				
$D_s^{*\pm}$	2.1123 ± 0.0005	$D_{0_{exp}}$	2.1324 ± 0.1845	3.0390	29.8
$D_{s_0}^*(2317)$	2.3178 ± 0.0006				
$D_{s_1}^{\pm}(2460)$	2.4596 ± 0.0006				
$D_{s_1}(2536)$	2.53512 ± 0.00013	$D_{1_{exp}}$	2.49736 ± 0.0378	3.7694	33.7
$D_{s_2}^*(2573)$	2.5719 ± 0.0008	$D_{2_{exp}}$	2.5719 ± 0.0008	4.2881	40.0

Table 2.7: Experimental mass spectra of mixed-composed mesons ($bottom + charm$, $bottom + strange$ and $charm + strange$).

2.2 Solving the NRSE in p-space

In the last section, the NRSE was solved numerically in configuration space for two interesting types of potentials. In this section we will solve the same equation again, but this time in momentum space. There are three main reasons to invest some time and effort in this problem:

1. Generalization to the relativistic case: When we try to attack the problem of bound-states relativistically it is much easier to do so in momentum space, where retardation and non-locality effects are better handled. For example, even the most straightforward relativistic generalization of the kinetic-energy operator is very cumbersome in configuration space, but rather simple in momentum space (ref.[27]).

2. Intermediate step before the study of a specific covariant model: Certain aspects of the covariant model we want to apply in a later stage are built in close analogy with the nonrelativistic case. For instance, the precise definition of the linear potential, when one moves from configuration to momentum space, is very subtle, and it is useful to learn how to do it properly in the nonrelativistic regime first and then move to a covariant framework.

3. Possibility of testing new numerical methods: Since the binding energies calculated in momentum space must be the same as the ones we already obtained in configuration space, we are able to test the accuracy of our numerical methods. It is also a very instructive exercise in another aspect: the technical difficulties that appear in the nonrelativistic case, namely the appearance of singularities, are the same as in the relativistic case. By using a nonrelativistic framework first we can study them in isolation, without having to deal with additional complications of purely relativistic origin (negative-energy solutions, etc...).

2.2.1 Finding a "suitable" linear potential in momentum space

In this section we are interested in preparing the path for a relativistic generalization of our model of mesons. To accomplish that, just as argued above, we need to move to momentum space. In the next and subsequent chapters, we will then be able to study mesons in a covariant manner, following the core ideas of the Covariant Spectator Theory (CST) and, more specifically, the model developed by Gross and Milana (ref.[3]). In their model they use a linear confining potential to represent the interquark interaction. Thus, the first challenge is to understand how to convert the well-known linear potential in configuration space into an equivalent form in momentum space. However there is a problem since the linear potential [3]

$$\tilde{V}(\mathbf{r}) = \sigma r \tag{2.30}$$

cannot be Fourier-transformed into momentum space because the corresponding integral does not exist. Instead, one can start with the screened potential

$$\tilde{V}_{S,\varepsilon}(\mathbf{r}) = \sigma r e^{-\varepsilon r} = \sigma \frac{\partial^2}{\partial \varepsilon^2} \frac{e^{-\varepsilon r}}{r}, \tag{2.31}$$

which turns into the linear potential in the limit $\varepsilon \to 0$. Its Fourier transform is

$$\begin{aligned} V_{S,\varepsilon}(\mathbf{q}) &= \int d^3 r e^{i\mathbf{q}.\mathbf{r}} \tilde{V}_{S,\varepsilon}(\mathbf{r}) = \sigma \frac{\partial^2}{\partial \varepsilon^2} \int d^3 r e^{i\mathbf{q}.\mathbf{r}} \frac{e^{-\varepsilon r}}{r} \\ &= -\frac{8\pi\sigma}{\left(q^2+\varepsilon^2\right)^2} + \frac{32\pi\sigma\varepsilon^2}{\left(q^2+\varepsilon^2\right)^3}. \end{aligned} \tag{2.32}$$

We define the two separate terms as

$$V_{A,\varepsilon}(\mathbf{q}) = -\frac{8\pi\sigma}{\left(q^2+\varepsilon^2\right)^2}, \qquad V_{B,\varepsilon}(\mathbf{q}) = \frac{32\pi\sigma\varepsilon^2}{\left(q^2+\varepsilon^2\right)^3}. \tag{2.33}$$

The inverse transform reproduces of course the original coordinate-space potential.

$$\int \frac{d^3 q}{(2\pi)^3} e^{-i\mathbf{q}.\mathbf{r}} V_{s,\varepsilon}(\mathbf{q}) = \tilde{V}_{s,\varepsilon}(\mathbf{r}). \tag{2.34}$$

In particular since $\tilde{V}_{s,\varepsilon}(0) = 0$, we get the condition

$$\int \frac{d^3 q}{(2\pi)^3} V_{s,\varepsilon}(\mathbf{q}) = 0. \tag{2.35}$$

One might be tempted to take the limit $\varepsilon \to 0$ immediately in $V_{A,\varepsilon}$ and $V_{B,\varepsilon}$. This can be done without problems for $V_{A,\varepsilon}$,

$$\lim_{\varepsilon\to 0} V_{A,\varepsilon}(\mathbf{q}) \equiv V_A(q) = -\frac{8\pi\sigma}{q^4}, \tag{2.36}$$

but for $V_{B,\varepsilon}$ the situation is slightly more complicated:

$$\lim_{\varepsilon\to 0} V_{B,\varepsilon}(\mathbf{q}) \equiv V_B(q) = \begin{cases} 0, & q \neq 0 \\ \infty, & q = 0 \end{cases} \tag{2.37}$$

[3] In this section, the tilde distinguishes the configuration-space from the momentum-space potential.

$V_{B,\varepsilon}$ has properties similar to those of a delta function, although not exactly.[4]

It is instructive to transform $V_{A,\varepsilon}(\mathbf{q})$ and $V_{B,\varepsilon}(\mathbf{q})$ back to coordinate space. We obtain

$$\tilde{V}_{A,\varepsilon}(\mathbf{r}) = \int \frac{d^3q}{(2\pi)^3} e^{-i\mathbf{q}.\mathbf{r}} V_{A,\varepsilon}(\mathbf{q}) = -\frac{\sigma}{\varepsilon} e^{-\varepsilon r}, \tag{2.38}$$

and

$$\tilde{V}_{B,\varepsilon}(\mathbf{r}) = \int \frac{d^3q}{(2\pi)^3} e^{-i\mathbf{q}.\mathbf{r}} V_{B,\varepsilon}(\mathbf{q}) = \left(\frac{\sigma}{\varepsilon} + \sigma r\right) e^{-\varepsilon r}. \tag{2.39}$$

Clearly the sum of $\tilde{V}_{A,\varepsilon}$ and $\tilde{V}_{B,\varepsilon}$ reproduces $\tilde{V}_{S,\varepsilon}$. Expanding the exponentials for small ε one gets

$$\tilde{V}_{A,\varepsilon}(\mathbf{r}) + \tilde{V}_{B,\varepsilon}(\mathbf{r}) = \left[-\frac{\sigma}{\varepsilon} + \sigma r + \mathscr{O}(\varepsilon)\right] + \left[\frac{\sigma}{\varepsilon} + \sigma r - \sigma r + \mathscr{O}(\varepsilon)\right], \tag{2.40}$$

from which we can see that (i) the behavior linear in r emerges from $\tilde{V}_{A,\varepsilon}$, and not from $\tilde{V}_{B,\varepsilon}(\mathbf{r})$ as a superficial look at eq. (2.39) might suggest; and (ii) that the role of $\tilde{V}_{B,\varepsilon}(\mathbf{r})$ is to provide a $\dfrac{\sigma}{\varepsilon}$ that cancels the constant $-\dfrac{\sigma}{\varepsilon}$ in $\tilde{V}_{A,\varepsilon}(\mathbf{r})$.

We can conclude that $\tilde{V}_{B,\varepsilon}(\mathbf{r})$ can be replaced by any other function that behaves for small ε like $\sigma/\varepsilon + \mathscr{O}(\varepsilon)$ to obtain the same limit. The simplest and obvious choice is

$$\tilde{V}_{C,\varepsilon}(\mathbf{r}) = \frac{\sigma}{\varepsilon}, \tag{2.41}$$

and we define a new screened linear potential

$$\tilde{V}_{L,\varepsilon}(\mathbf{r}) = \tilde{V}_{A,\varepsilon}(\mathbf{r}) + \tilde{V}_{C,\varepsilon}(\mathbf{r}) = \frac{\sigma}{\varepsilon}\left(1 - e^{-\varepsilon r}\right), \tag{2.42}$$

which we can also write as

$$\tilde{V}_{L,\varepsilon}(\mathbf{r}) = \tilde{V}_{A,\varepsilon}(\mathbf{r}) - \tilde{V}_{A,\varepsilon}(0). \tag{2.43}$$

Fig.(2.6) illustrates the qualitative bahaviour of the various r-space potentials for a finite value of ε.

One could have started out directly by proposing Eq. (2.42) as screened linear potential. However, the detour through Eq.(2.31) was useful because it motivates the structure in which a singular potential is regularized by a subtraction term, both in $r-$space, as in Eq.(2.43), and in momentum space, which we will derive shortly.

There is an important argument why the form of Eq.(2.42) is preferable over Eq.(2.31): as long as ε is kept finite (and it may later turn out necessary not to go completely to the limit $\varepsilon \to 0$), $\tilde{V}_{L,\varepsilon}(\mathbf{r})$ can have real bound states, while in the case of $\tilde{V}_{S,\varepsilon}(\mathbf{r})$ barrier penetration prevents that rigorous bound states can be formed.

[4] One definition of the $\delta(x)$ function is $\delta(x) = \lim_{\varepsilon\to 0} \dfrac{1}{\pi}\dfrac{\varepsilon}{\varepsilon^2 + x^2}$, which differs from Eq.2.33.

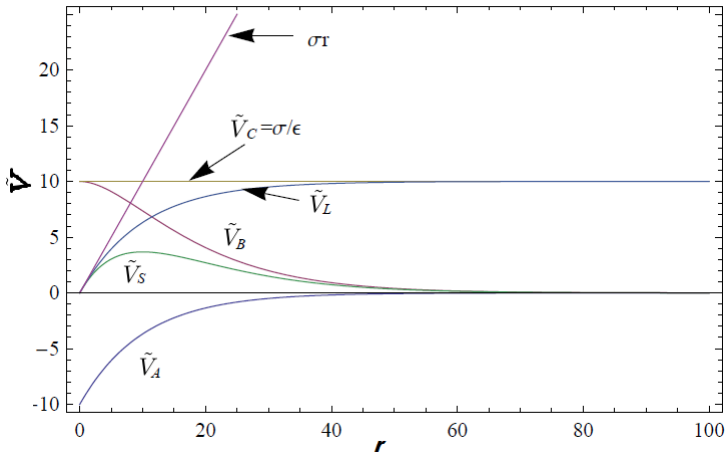

Figure 2.6: Sketches of the various $\varepsilon-$dependent coordinate-space potentials.

Now the momentum-space form of our new screened linear potential can be written down:

$$\begin{aligned} V_{L,\varepsilon}(q) &= \int d^3r \tilde{V}_{L,\varepsilon}(\mathbf{r}) e^{i\mathbf{q}.\mathbf{r}} \\ &= \int d^3r \left[\tilde{V}_{A,\varepsilon}(\mathbf{r}) - \tilde{V}_{A,\varepsilon}(0)\right] e^{i\mathbf{q}.\mathbf{r}} \\ &= \int d^3r \tilde{V}_{A,\varepsilon}(\mathbf{r}) e^{i\mathbf{q}.\mathbf{r}} - (2\pi)^3 \delta^{(3)}(\mathbf{q}) \tilde{V}_{A,\varepsilon}(0) \\ &= V_{A,\varepsilon}(q) - (2\pi)^3 \delta^{(3)}(\mathbf{q}) \int \frac{d^3q'}{(2\pi)^3} V_{A,\varepsilon}(q'). \end{aligned} \tag{2.44}$$

If one takes the limit $\varepsilon \to 0$ here, one gets a potential that is singular at $\mathbf{q} = 0$, but with a "built-in"' subtraction that regularizes integrations over the singularity.

$$\begin{aligned} V_L(q) &= \lim_{\varepsilon \to 0} \left[V_{A,\varepsilon}(q) - (2\pi)^3 \delta^{(3)}(\mathbf{q}) \int \frac{d^3q'}{(2\pi)^3} V_{A,\varepsilon}(q') \right] \\ &= V_A(q) - (2\pi)^3 \delta^{(3)}(\mathbf{q}) \int \frac{d^3q'}{(2\pi)^3} V_A(q'). \end{aligned}$$

This form of the potential prevents the existence of a barrier penetrating effect, leading to non-zero decay width instead of true bound-states. Moreover, it has a practical advantage: in numerical calculations there is no need for a finite screening parameter ε and therefore we do not have to perform studies of the convergence of the results with decreasing values of ε.

2.2.2 The partial-wave decomposition

The next step is to write down a version of the NRSE equation in momentum space that allow us to calculate all states of the mesonic spectra with non-zero orbital angular momentum. This implies that we have to decompose the momentum-space Schrödinger equation into partial waves for the linear potential

$$V_L(\mathbf{q}) = \lim_{\varepsilon \to 0} \left[V_A(\mathbf{q}) - (2\pi)^3 \delta^{(3)}(\mathbf{q}) \int \frac{d^3\mathbf{q}'}{(2\pi)^3} V_A(\mathbf{q}') \right], \tag{2.45}$$

where $\mathbf{q}$ is the momentum transfer, and from here on we drop the ε from $V_{A,\varepsilon}$ in favor of the simplified notation

$$V_A(\mathbf{q}) = -\frac{8\pi\sigma}{(\mathbf{q}^2+\varepsilon^2)^2}\,. \tag{2.46}$$

With this potential, the Schrödinger equation becomes

$$\frac{p^2}{2m_R}\langle\mathbf{p}|\psi\rangle + \int\frac{d^3k}{(2\pi)^3}\langle\mathbf{p}|V_L|\mathbf{k}\rangle\langle\mathbf{k}|\psi\rangle = E\langle\mathbf{p}|\psi\rangle\,, \tag{2.47}$$

or, after substituting (2.45),

$$\frac{p^2}{2m_R}\langle\mathbf{p}|\psi\rangle + \int\frac{d^3k}{(2\pi)^3}\langle\mathbf{p}|V_A|\mathbf{k}\rangle\left(\langle\mathbf{k}|\psi\rangle - \langle\mathbf{p}|\psi\rangle\right) = E\langle\mathbf{p}|\psi\rangle\,. \tag{2.48}$$

The limit $\varepsilon\to 0$ can be performed, and we see that the matrix element of V_A,

$$\langle\mathbf{p}|V_A|\mathbf{k}\rangle = -\frac{8\pi\sigma}{(\mathbf{k}-\mathbf{p})^4} = -\frac{8\pi\sigma}{(k^2+p^2-2pkx)^2} = V_A(p,k,x)\,, \tag{2.49}$$

with $x=\hat{\mathbf{k}}\cdot\hat{\mathbf{p}}$, depends only on the magnitudes k and p and the angle between $\mathbf{k}$ and $\mathbf{p}$. Such a function can be expanded into a series of Legendre polynomials,

$$V_A(p,k,x) = \sum_{n=0}^{\infty} c_n(p,k)P_n(x)\,. \tag{2.50}$$

The expansion coefficients can be deduced using the orthogonality relation

$$\int_{-1}^{1} dx P_n(x)P_{n'}(x) = \frac{2}{2n+1}\delta_{nn'}\,. \tag{2.51}$$

They are given through

$$c_n(p,k) = \frac{2n+1}{2}\int_{-1}^{1} dx P_n(x)V_A(p,k,x)\,. \tag{2.52}$$

In this context, it is useful to rewrite the expansion in terms of spherical harmonics, applying the addition theorem

$$P_n(\hat{\mathbf{k}}\cdot\hat{\mathbf{p}}) = \frac{4\pi}{2n+1}\sum_{m_n=-n}^{n} Y^*_{nm_n}(\hat{\mathbf{k}})Y_{nm_n}(\hat{\mathbf{p}})\,. \tag{2.53}$$

Now we can write

$$\langle\mathbf{p}|V_A|\mathbf{k}\rangle = V_A(p,k,x) = \sum_{nm_n}\frac{4\pi}{2n+1}c_n(p,k)Y^*_{nm_n}(\hat{\mathbf{k}})Y_{nm_n}(\hat{\mathbf{p}})\,, \tag{2.54}$$

or, after redefining the expansion coefficient through

$$\langle p\,nm_n|V_A|k\,nm_n\rangle = \frac{4\pi}{2n+1}c_n(p,k) = 2\pi\int_{-1}^{1} dx P_n(x)V_A(p,k,x)\,, \tag{2.55}$$

we get

$$\langle\mathbf{p}|V_A|\mathbf{k}\rangle = \sum_{nm_n}\langle p\,nm_n|V_A|k\,nm_n\rangle Y^*_{nm_n}(\hat{\mathbf{k}})Y_{nm_n}(\hat{\mathbf{p}})\,. \tag{2.56}$$

Next, we also expand the wave function into spherical harmonics,

$$\begin{aligned}\langle\mathbf{p}|\psi\rangle &= \sum_{l'm'}\langle\hat{\mathbf{p}}|l'm'\rangle\langle p\,l'm'|\psi\rangle = \sum_{l'm'}Y_{l'm'}(\hat{\mathbf{p}})\langle p\,l'm'|\psi\rangle\\ \langle\mathbf{k}|\psi\rangle &= \sum_{l_1m_1}\langle\hat{\mathbf{k}}|l_1m_1\rangle\langle p\,l_1m_1|\psi\rangle = \sum_{l_1m_1}Y_{l_1m_1}(\hat{\mathbf{k}})\langle k\,l_1m_1|\psi\rangle\,.\end{aligned} \tag{2.57}$$

Substituting these expansions into (2.48), we obtain

$$\frac{p^2}{2m_R}\sum_{l'm'}Y_{l'm'}(\hat{\mathbf{p}})\langle p\,l'm'|\psi\rangle+\int\frac{d^3k}{(2\pi)^3}\sum_{nm_n}\langle p\,nm_n|V_A|k\,nm_n\rangle Y^*_{nm_n}(\hat{\mathbf{k}})Y_{nm_n}(\hat{\mathbf{p}})$$
$$\times\left(\sum_{l_1m_1}Y_{l_1m_1}(\hat{\mathbf{k}})\langle k\,l_1m_1|\psi\rangle-\sum_{l'm'}Y_{l'm'}(\hat{\mathbf{p}})\langle p\,l'm'|\psi\rangle\right)=E\sum_{l'm'}Y_{l'm'}(\hat{\mathbf{p}})\langle p\,l'm'|\psi\rangle\,. \quad (2.58)$$

It is convenient to separate the integrand into two parts, which will then be treated individually.

$$\frac{p^2}{2m_R}\sum_{l'm'}Y_{l'm'}(\hat{\mathbf{p}})\langle p\,l'm'|\psi\rangle+\sum_{l_1m_1}\sum_{nm_n}\int_0^\infty\frac{dkk^2}{(2\pi)^3}\int d\hat{\mathbf{k}}\langle p\,nm_n|V_A|k\,nm_n\rangle$$
$$Y^*_{nm_n}(\hat{\mathbf{k}})Y_{nm_n}(\hat{\mathbf{p}})Y_{l_1m_1}(\hat{\mathbf{k}})\langle k\,l_1m_1|\psi\rangle-\sum_{l'm'}\sum_{nm_n}\int_0^\infty\frac{dkk^2}{(2\pi)^3}\int d\hat{\mathbf{k}}\langle p\,nm_n|V_A|k\,nm_n\rangle$$
$$Y^*_{nm_n}(\hat{\mathbf{k}})Y_{nm_n}(\hat{\mathbf{p}})Y_{l'm'}(\hat{\mathbf{p}})\langle p\,l'm'|\psi\rangle=E\sum_{l'm'}Y_{l'm'}(\hat{\mathbf{p}})\langle p\,l'm'|\psi\rangle\,. \quad (2.59)$$

In the first integrand, we use the orthogonality relation for spherical harmonics,

$$\int d\hat{\mathbf{k}}\,Y^*_{nm_n}(\hat{\mathbf{k}})Y_{l_1m_1}(\hat{\mathbf{k}})=\delta_{nl_1}\delta_{m_nm_1}\,, \quad (2.60)$$

and in the second we use $Y_{00}(\hat{\mathbf{k}})=1/\sqrt{4\pi}$ to write

$$\int d\hat{\mathbf{k}}\,Y^*_{nm_n}(\hat{\mathbf{k}})=\sqrt{4\pi}\int d\hat{\mathbf{k}}\,Y^*_{nm_n}(\hat{\mathbf{k}})Y_{00}(\hat{\mathbf{k}})=\delta_{n0}\delta_{m_n0}\,. \quad (2.61)$$

The sums over n and m_n can be carried out and give

$$\frac{p^2}{2m_R}\sum_{l'm'}Y_{l'm'}(\hat{\mathbf{p}})\langle p\,l'm'|\psi\rangle+\sum_{l_1m_1}\int_0^\infty\frac{dkk^2}{(2\pi)^3}\langle p\,l_1m_1|V_A|k\,l_1m_1\rangle Y_{l_1m_1}(\hat{\mathbf{p}})\langle k\,l_1m_1|\psi\rangle$$
$$-\sum_{l'm'}\int_0^\infty\frac{dkk^2}{(2\pi)^3}\langle p\,00|V_A|k\,00\rangle\sqrt{4\pi}Y_{00}(\hat{\mathbf{p}})Y_{l'm'}(\hat{\mathbf{p}})\langle p\,l'm'|\psi\rangle=E\sum_{l'm'}Y_{l'm'}(\hat{\mathbf{p}})\langle p\,l'm'|\psi\rangle\,. \quad (2.62)$$

In the second integrand, we can simplify again with $\sqrt{4\pi}Y_{00}(\hat{\mathbf{p}})=1$.

In order to project out the partial wave $\{lm\}$, we multiply this equation by $Y^*_{lm}(\hat{\mathbf{p}})$ and integrate over $\hat{\mathbf{p}}$. Orthogonality then yields

$$\frac{p^2}{2m_R}\langle p\,lm|\psi\rangle+\int_0^\infty\frac{dkk^2}{(2\pi)^3}\left(\langle p\,lm|V_A|k\,lm\rangle\langle k\,lm|\psi\rangle-\langle p\,00|V_A|k\,00\rangle\langle p\,lm|\psi\rangle\right)=E\langle p\,lm|\psi\rangle\,. \quad (2.63)$$

The potential V_A in partial-wave form

We need the partial-wave matrix elements

$$\langle p\,lm|V_A|k\,lm\rangle=2\pi\int_{-1}^1dxP_l(x)V_A(p,k,x)=2\pi(-8\pi\sigma)\int_{-1}^1dx\frac{P_l(x)}{(k^2+p^2-2pkx)^2}$$
$$=2\pi\frac{-8\pi\sigma}{(2pk)^2}\int_{-1}^1dx\frac{P_l(x)}{(\frac{k^2+p^2}{2pk}-x)^2}\,. \quad (2.64)$$

Introducing

$$y = \frac{p^2+k^2}{2pk}\,, \tag{2.65}$$

and using the Legendre functions of the second kind,

$$Q_l(y) = \frac{1}{2}\int_{-1}^{1} dx \frac{P_l(x)}{y-x}\,, \tag{2.66}$$

we can write

$$\int_{-1}^{1} dx \frac{P_l(x)}{(y-x)^2} = -\frac{\partial}{\partial y}\int_{-1}^{1} dx \frac{P_l(x)}{y-x} = -\frac{\partial}{\partial y} 2Q_l(y) = -2Q_l'(y)\,. \tag{2.67}$$

Let us calculate the case $l = 0$ explicitly:

$$Q_0(y) = \frac{1}{2}\ln\left|\frac{y+1}{y-1}\right| = \frac{1}{2}\ln\left(\frac{p+k}{p-k}\right)^2\,, \tag{2.68}$$

and

$$Q_0'(y) = \frac{1}{1-y^2} = -\frac{4p^2k^2}{(p^2-k^2)^2}\,. \tag{2.69}$$

Clearly, both $Q_0(y)$ and $Q_0'(y)$ are singular at $k = p$. In fact, when we go to $l \neq 0$, the only terms singular at $k = p$ ($y = 1$) come from $Q_0(y)$ and $Q_0'(y)$, which one can see from

$$Q_l(y) = P_l(y)Q_0(y) - w_{l-1}(y)\,, \tag{2.70}$$

where

$$w_{l-1}(y) = \sum_{m=1}^{l} \frac{1}{m} P_{l-m}(y) P_{m-1}(y) \tag{2.71}$$

is non-singular and contributes only for $l \geq 1$. The first few cases are

- $l = 1:\quad w_0(y) = 1,$
- $l = 2:\quad w_1(y) = \frac{3}{2}y,$
- $l = 3:\quad w_2(y) = \frac{5}{2}y^2 - \frac{2}{3},$
- $l = 4:\quad w_3(y) = \frac{35}{8}y^3 - \frac{55}{24}y.$

Putting everything together, we get

$$\begin{aligned}\langle p\,lm|V_A|k\,lm\rangle &= 2\pi\frac{-8\pi\sigma}{(2pk)^2}(-2)\left[P_l'(y)Q_0(y) + P_l(y)Q_0'(y) - w_{l-1}'(y)\right] \\ &= 2\pi(-8\pi\sigma)\left[\frac{2P_l(y)}{(p^2-k^2)^2} - \frac{P_l'(y)}{(2pk)^2}\ln\left(\frac{p+k}{p-k}\right)^2 + \frac{2w_{l-1}'(y)}{(2pk)^2}\right]\,.\end{aligned} \tag{2.72}$$

Substituting Eq.(2.72) into the partial-wave Schrödinger Eq.(2.63), and using the notation $\psi_l(p) = \langle p\,lm|\psi\rangle$ (note that the equation is independent of m because of rotational symmetry), yields

$$\begin{aligned}\frac{p^2}{2m_R}\psi_l(p) - \frac{2\sigma}{\pi}\int_0^\infty dk \Bigg\{ & Q_0'(y)\left[P_l(y)\psi_l(k) - \psi_l(p)\right] + P_l'(y)Q_0(y)\psi_l(k) \\ & - w_{l-1}'(y)\psi_l(k)\Bigg\} = E\,\psi_l(p)\,.\end{aligned} \tag{2.73}$$

or, more explicitly,

$$\frac{p^2}{2m_R}\psi_l(p) - \frac{2\sigma}{\pi}\int_0^\infty dk \left\{ \frac{2k^2}{(k^2-p^2)^2}\left[P_l(y)\psi_l(k) - \psi_l(p)\right] + \frac{w'_{l-1}(y)}{2p^2}\psi_l(k) \right. \\ \left. -\frac{1}{4p^2}\ln\left(\frac{p+k}{p-k}\right)^2 P'_l(y)\psi_l(k)\right\} = E\psi_l(p)\,. \quad (2.74)$$

In the following, we list a few important cases of the potential matrix elements and the resulting Schrödinger equation.

S-wave:

$$\langle p\,00|V_A|k\,00\rangle = 2\pi(-8\pi\sigma)\frac{2}{(p^2-k^2)^2}\,, \quad (2.75)$$

$$\frac{p^2}{2m_R}\psi_0(p) - \frac{4\sigma}{\pi}\int_0^\infty dk k^2 \frac{\psi_0(k)-\psi_0(p)}{(p^2-k^2)^2} = E\psi_0(p) \quad (2.76)$$

P-wave:

$$\langle p\,1m|V_A|k\,1m\rangle = 2\pi(-8\pi\sigma)\left[\frac{p^2+k^2}{2pk}\frac{2}{(p^2-k^2)^2} - \frac{1}{(2pk)^2}\ln\left(\frac{p+k}{p-k}\right)^2\right] \quad (2.77)$$

$$\frac{p^2}{2m_R}\psi_1(p) - \frac{2\sigma}{\pi}\int_0^\infty dk \left\{ \frac{2k^2}{(p^2-k^2)^2}\left[\frac{p^2+k^2}{2pk}\psi_1(k) - \psi_1(p)\right] - \right. \\ \left. \frac{1}{4p^2}\ln\left(\frac{p+k}{p-k}\right)^2\psi_1(k)\right\} = E\psi_1(p) \quad (2.78)$$

D-wave:

$$\langle p\,2m|V_A|k\,2m\rangle = 2\pi(-8\pi\sigma)\left[\left(\frac{3(p^2+k^2)^2}{(2pk)^2}-1\right)\frac{1}{(p^2-k^2)^2} + \frac{3}{(2pk)^2} - \right. \\ \left. -\frac{3\left(p^2+k^2\right)}{(2pk)^3}\ln\left(\frac{p+k}{p-k}\right)^2\right] \quad (2.79)$$

$$\frac{p^2}{2m_R}\psi_2(p) - \frac{2\sigma}{\pi}\int_0^\infty dk \left\{ \frac{2k^2}{(p^2-k^2)^2}\left[\frac{1}{2}\left(\frac{3(p^2+k^2)^2}{(2pk)^2}-1\right)\psi_2(k) - \psi_2(p)\right] + \right. \\ \left. +\frac{3}{4p^2}\psi_2(k) - \frac{3}{4p^2}\left(\frac{p^2+k^2}{2pk}\right)\ln\left(\frac{p+k}{p-k}\right)^2\psi_2(k)\right\} = E\psi_2(p) \quad (2.80)$$

In each case, the integral over k in the Schrödinger equation is to be understood as a principal value integral.

2.2.3 Two methods to deal with the singularities

Singularity-free integral equations

The kernel of Eq. (2.74) is singular at $k = p$. The first term of the integrand appears to have a double pole, but because the numerator goes to zero like $(k-p)$, as we will see, it is actually a single pole and the principal value integral exists. The singularity in the log-term is integrable even in the sense of an ordinary integral.

There exist standard numerical methods to solve integral equations with principal-value type singularities. However, they require special care and typically also more computing time. From the practical point of view it would be a considerable advantage to eliminate those singularities altogether. We will show now that this can be achieved by means of subtraction methods.

Removal of the principal value singularity

In this section we will outline the main steps required to remove the singularities. In the following it is important to distinguish between the ordinary integral and the Cauchy principal value integral, denoted here by the symbol "$⨍$".

Thus, considering the most singular part of Eq.(2.74), which appears in

$$I_1 \equiv ⨍_0^\infty dk \frac{2k^2}{(k^2-p^2)^2}\left[P_l(y)\psi_l(k) - \psi_l(p)\right]. \tag{2.81}$$

We expand the factor in brackets in a Taylor series around $k = p$:

$$\begin{aligned} P_l(y)\psi_l(k) - \psi_l(p) =& \psi_l(p) + (k-p)\left[P_l'(y)\frac{dy}{dk}\psi_l(k) + P_l(y)\psi_l'(k)\right]_{k=p} + \\ +(k-p)^2 R_l(k) - \psi_l(p) =& (k-p)\psi_l'(p) + (k-p)^2 R_l(k). \end{aligned} \tag{2.82}$$

Here we have used that $y = 1$ when $k = p$, $P_l(1) = 1$, $P_l'(1) = l(l+1)/2$, and $\frac{dy}{dk}|_{k=p} = 0$. The function $R_l(k)$ is the remainder of the Taylor series of $\psi_l(k)$ around $k = p$ after the constant and linear terms have been subtracted and $(k-p)^2$ has been factored out. The only important property of $R_l(k)$ in this context is that it is finite at $k = p$.

The integrand of Eq.(2.81) can thus be written as

$$\frac{2k^2}{(k^2-p^2)^2}\left[P_l(y)\psi_l(k) - \psi_l(p)\right] = \frac{2k^2}{(k+p)^2}\frac{\psi_l'(p)}{k-p} + \frac{2k^2 R_l(k)}{(k+p)^2}, \tag{2.83}$$

and in this form it is now explicit that the singularity is just a simple pole. We can rewrite it as

$$\frac{2k^2}{(k^2-p^2)^2}\left[P_l(y)\psi_l(k) - \psi_l(p)\right] = \frac{\psi_l'(p)}{k^2-p^2}\frac{2k^2}{k+p} + \frac{2k^2 R_l(k)}{(k+p)^2} \tag{2.84}$$

$$= \frac{\psi_l'(p)}{k^2-p^2}\left[\frac{2k^2}{k+p} - p + p\right] + \frac{2k^2 R_l(k)}{(k+p)^2} \tag{2.85}$$

$$= \frac{p\psi_l'(p)}{k^2-p^2} + \frac{\psi_l'(p)}{k^2-p^2}\left[\frac{(k-p)(2k+p)}{k+p}\right] + \frac{2k^2 R_l(k)}{(k+p)^2} \tag{2.86}$$

$$= \frac{p\psi_l'(p)}{k^2-p^2} + \psi_l'(p)\frac{2k+p}{(k+p)^2} + \frac{2k^2 R_l(k)}{(k+p)^2}. \tag{2.87}$$

The point of this reorganization is that the integrand is now separated into a singular term that can be integrated analytically and a non-singular remainder. We can write

$$I_1 = \int_0^\infty dk \left\{ \frac{2k^2}{(k^2-p^2)^2} \left[P_l(y)\psi_l(k) - \psi_l(p)\right] - \frac{p\psi_l'(p)}{k^2-p^2} \right\} + p\psi_l'(p) \int_0^\infty \frac{dk}{k^2-p^2}\,, \tag{2.88}$$

and applying the well-known result

$$\int_0^\infty \frac{dk}{k^2-p^2} = 0 \tag{2.89}$$

we arrive at

$$I_1 = \int_0^\infty \frac{dk}{k^2-p^2} \left\{ \frac{2k^2}{k^2-p^2} \left[P_l(y)\psi_l(k) - \psi_l(p)\right] - p\psi_l'(p) \right\}. \tag{2.90}$$

Note that the modified integrand is now regular at $k = p$, and Eq.(2.90) is no longer a principal-value but an ordinary integral. The price to pay for this simplification is that the derivative of the wave function enters the integrand. However, this is no significant complication if the method of solving the integral equation uses an expansion of $\psi_l(p)$ into a set of basis functions whose derivatives can be easily calculated.

Subtraction of the logarithmic singularity

The second singular integrand occurs in

$$I_2 \equiv -\frac{1}{4p^2} \int_0^\infty dk \ln\left(\frac{p+k}{p-k}\right)^2 P_l'(y)\psi_l(k) = -\frac{1}{2p^2} \int_0^\infty dk\, Q_0(y) P_l'(y)\psi_l(k)\,. \tag{2.91}$$

In this case, we can take advantage of the known result

$$\int_0^\infty dk \frac{Q_0(y)}{k} = \frac{\pi^2}{2}\,. \tag{2.92}$$

We can bring I_2 into the following form:

$$I_2 = -\frac{1}{2p^2} \int_0^\infty dk\, Q_0(y) \left[P_l'(y)\psi_l(k) - \frac{p}{k} P_l'(1)\psi_l(p) + \frac{p}{k} P_l'(1)\psi_l(p)\right] \tag{2.93}$$

$$= -\frac{1}{2p^2} \int_0^\infty dk\, Q_0(y) \left[P_l'(y)\psi_l(k) - \frac{p}{k}\frac{l(l+1)}{2}\psi_l(p)\right] - \frac{1}{2p^2}\frac{p\,l(l+1)}{2}\psi_l(p) \int_0^\infty dk\, \frac{Q_0(y)}{k} \tag{2.94}$$

$$= -\frac{1}{2p^2} \int_0^\infty dk\, Q_0(y) \left[P_l'(y)\psi_l(k) - \frac{p}{k}\frac{l(l+1)}{2}\psi_l(p)\right] - \frac{\pi^2 l(l+1)}{8p}\psi_l(p)\,. \tag{2.95}$$

It is easy to see that the factor in brackets in the integrand is proportional to $(k-p)$ near $k = p$, such that the product $(k-p)Q_0(y)$ goes to zero at that point. The subtracted integrand is therefore also non-singular.

Singularity-free form of the partial wave Schrödinger equation

Substitution of the reorganized forms for I_1 and I_2 into the partial wave Schrödinger Eq.(2.74) gives us the final result

$$\left[\frac{p^2}{2m_R}+\frac{\sigma\pi l(l+1)}{4p}\right]\psi_l(p)-\frac{2\sigma}{\pi}\int_0^\infty dk\left\{\frac{1}{k^2-p^2}\left[\frac{2k^2}{k^2-p^2}\Big(P_l(y)\psi_l(k)-\psi_l(p)\Big)-p\psi_l'(p)\right]+\right.$$
$$+\frac{w_{l-1}'(y)}{2p^2}\psi_l(k)-\frac{1}{4p^2}\ln\left(\frac{p+k}{p-k}\right)^2$$
$$\left.\times\left[P_l'(y)\psi_l(k)-\frac{l(l+1)}{2}\frac{p}{k}\psi_l(p)\right]\right\}=E\psi_l(p)\,. \qquad (2.96)$$

We list again the most important cases:

S-wave:

$$\frac{p^2}{2m_R}\psi_0(p)-\frac{2\sigma}{\pi}\int_0^\infty\frac{dk}{k^2-p^2}\left[\frac{2k^2}{k^2-p^2}\Big(\psi_0(k)-\psi_0(p)\Big)-p\psi_0'(p)\right]=E\psi_0(p)\,. \qquad (2.97)$$

P-wave:

$$\left[\frac{p^2}{2m_R}+\frac{\pi\sigma}{2p}\right]\psi_1(p)-\frac{2\sigma}{\pi}\int_0^\infty dk\left\{\frac{1}{k^2-p^2}\left[\frac{2k^2}{k^2-p^2}\left(\frac{p^2+k^2}{2pk}\psi_1(k)-\psi_1(p)\right)-p\psi_1'(p)\right]\right.$$
$$\left.-\frac{1}{4p^2}\ln\left(\frac{p+k}{p-k}\right)^2\left[\psi_1(k)-\frac{p}{k}\psi_1(p)\right]\right\}=E\psi_1(p)\,. \qquad (2.98)$$

D-wave:

$$\left[\frac{p^2}{2m_R}+\frac{3\pi\sigma}{2p}\right]\psi_2(p)-$$
$$-\frac{2\sigma}{\pi}\int_0^\infty dk\left\{\frac{1}{k^2-p^2}\left[\frac{2k^2}{k^2-p^2}\left(\frac{1}{2}\left(3\left(\frac{p^2+k^2}{2pk}\right)^2-1\right)\psi_2(k)-\psi_2(p)\right)-p\psi_2'(p)\right]\right.$$
$$\left.+\frac{3}{4p^2}\psi_2(k)-\frac{3}{4p^2}\ln\left(\frac{p+k}{p-k}\right)^2\left[\frac{p^2+k^2}{2pk}\psi_2(k)-\frac{p}{k}\psi_2(p)\right]\right\}=E\psi_2(p)\,. \qquad (2.99)$$

2.2.4 Numerical technique: expansion in splines

In order to solve the NRSE in momentum space for s-waves, p-waves and d-waves we have adopted a method where the wave functions are expanded into a sum of spline functions.

We use a set of cubic polynomial B-splines as our basis functions. Other choices are possible, but based on the literature, this set of functions has proven to possess high enough flexibility to reproduce the solutions we are interested in when solving the 1CS equation (in Chapter 3), especially in matching the high-momentum tail, where other basis functions (Laguerre polynomials in ref.[3]; generalized Yukawas, in ref.[8]) were less successful.

This way we applied them here first in the nonrelativistic domain and then used them again for the equations of the next Chapter.

In the splines method we pick a set of SN basis functions $\{\beta_n(p)\}$ and take the wavefunction to be a linear combination of them

$$\psi(p)=\sum_{n=1}^{SN}a_n\beta_n(p), \qquad (2.100)$$

where $a_j \in \Re$ are the coefficients to be determined. To construct a basis $\{\beta_n(p)\}$ on the interval $p \in [0,\infty[$, we start from a basis $\{b_n(x)\}$ on $x \in [0,1]$, and then perform an appropriate variable transformation from x to p.

The set $\{b_n(x)\}$ is defined to have finite support and continuous first and second derivatives. These requirements were achieved by piecing together four cubic polynomials, each defined over a finite region. The point were the polynomials join are called knots. The cubic $B-$spline $b_n(x)$, centered at knot x_n, with equal space h, between the knots, is defined in $x \in [0,1]$ by:

$$b_n(x) = \frac{1}{4}\begin{cases} \left(\dfrac{x-x_{n-2}}{h}\right)^3, & x \in [x_{n-2}, x_{n-1}] \\ 1+3\dfrac{x-x_{n-1}}{h}+3\left(\dfrac{x-x_{n-1}}{h}\right)^2-3\left(\dfrac{x-x_{n-1}}{h}\right)^3, & x \in [x_{n-1}, x_n] \\ 1+3\dfrac{x_{n+1}-x}{h}+3\left(\dfrac{x_{n+1}-x}{h}\right)^2-3\left(\dfrac{x_{n+1}-x}{h}\right)^3, & x \in [x_n, x_{n+1}] \\ \left(\dfrac{x_{n+2}-x}{h}\right)^3, & x \in [x_{n+1}, x_{n+2}] \\ 0, & \text{otherwise.} \end{cases} \tag{2.101}$$

If SN is the number of splines, then $h = \dfrac{1}{SN+1}$.

With the above definition of $\{b_n(x)\}$, one must now apply a mapping to transform $x \in [0,1]$ to $p \in [0,\infty[$ and impose the correct boundary conditions in $p = 0$.

For the $S-$wave basis, the derivative of the mapped functions must be zero at the origin and none of the knots may lie outside of the interval from 0 to 1, so the first spline, $b_1(x)$, is defined entirely by the third and fourth functions given in Eq.(2.101) and it has a zero slope at $x = 0$. The $b_2(x)$ spline was defined in a special way so that it too will have zero slope at $x = 0$. To accomplish this, the first sector, which lies between x_0 and x_1 is ''folded over'' onto the interval between $[x_1, x_2]$ so it becomes,

$$b_2(x) = \frac{1}{4}\left(1+3\frac{x-x_1}{h}+3\left(\frac{x-x_1}{h}\right)^2-3\left(\frac{x-x_1}{h}\right)^3+\left(\frac{x_2-x}{h}\right)^3\right). \tag{2.102}$$

With this definition, applying now the mapping

$$x = \frac{2}{\pi}\arctan\left(\frac{p}{\Lambda}\right), \tag{2.103}$$

where Λ is a scale parameter (in our calculations chosen to be $\Lambda = 1\,GeV$), we get the full $S-$wave basis

$$\beta_n(p) \equiv b_n(x(p)) \tag{2.104}$$

on the interval $p \in [0,\infty]$. As an example, for the case SN= 4 the basis functions $b_n(x)$ and $\beta_n(p)$ are shown in Figs.2.7 and 2.8 .

However, or the $P-$wave, $D-$wave, etc., the basis previously defined is not suitable since it does not reflect the correct low-momentum behavior near $p = 0$. It is known (see, for instance, ref.[21])

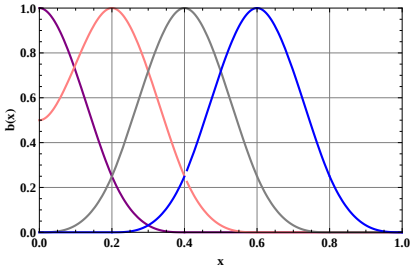

Figure 2.7: Plot of the spline basis functions $b_n(x)$ for SN=4.

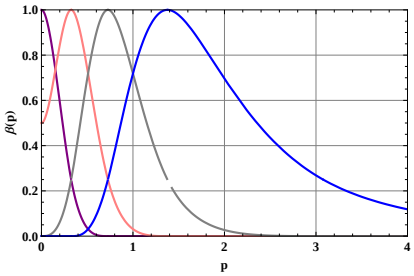

Figure 2.8: Plot of the transformed spline basis functions $\beta_n(p)$ for SN=4.

that for small momenta $\psi_l(p) \sim p^l$. A natural choice for the $P-$wave and the $D-$wave basis seems to be

$$\beta_p(p) = p\beta(p) \tag{2.105}$$

$$\beta_d(p) = p^2\beta(p) \tag{2.106}$$

Unfortunately, these basis functions are not satisfactory yet, since they don't fall off sufficiently fast when $p \to \infty$. However, a suitable choice is

$$\beta_p(p) = \frac{p}{E_p}\beta(p) = \frac{p}{\sqrt{m^2+p^2}}\beta(p), \tag{2.107}$$

$$\beta_d(p) = \left(\frac{p}{E_p}\right)^2 \beta(p) = \frac{p^2}{m^2+p^2}\beta(p), \tag{2.108}$$

because, the multiplying factor goes to 1 for $p \to \infty$, and the square root in the denominator becomes constant when $p \to 0$, resulting also in the right behavior.

In order to illustrate the two previously described methods we took here the NRSE for $l = 0$ after our procedure to transform it in a singularity-free equation, i.e,

$$\frac{p^2}{2m_R}\psi(p) - \frac{4\sigma}{\pi}\int_0^\infty dk \frac{k^2}{(k+p)^2(k-p)^2} \cdot \left[\psi(k) - \psi(p) - \frac{p^2}{2pk^2}(k+p)(k-p)\psi'(p)\right] = E\psi(p), \tag{2.109}$$

2.2.5 SSI Method (Splines single integration)

The **SSI Method** (Splines single integration) uses a set cubic splines $\beta_j(p)$ defined in order to have the appropriate boundary conditions for the different l states. It is called splines single integration method because it only requires single integrations.

Taking the expansion $\psi(p) = \sum_{j=1}^{SN} \alpha_j \beta_j(p)$, the first step involves choosing a proper mesh of points $p_i = 1, ..., SN$ so that Eq.(2.109) can be transformed into:

$$\sum_{j=1}^{SN} \frac{p_i^2}{2m_R}\beta_j(p_i)\alpha_j - \frac{4\sigma}{\pi}\sum_{j=1}^{SN}\int_0^\infty dp \frac{k^2}{(k+p_i)^2(k-p_i)^2}\cdot \\ \cdot\left[\beta_j(k) - \beta_j(p_i) - \frac{p^2(k+p_i)(k-p_i)}{2p_i k^2}\beta_j'(p_i)\right]\alpha_j = E\sum_{j=1}^{SN}\beta_j(p_i)\alpha_j. \quad (2.110)$$

The mesh was chosen so that the point were equally distributed in $x \in [0,1]$ and then mapped into $p \in [0,\infty[$, However, there's no unique choice and the results obtained are not completely independent from this.

Defining now

$$A_{ij} = \frac{p_i^2}{2m_R}\beta_j(p_i), \quad (2.111)$$

$$V_{ij} = -\frac{4\sigma}{\pi}\sum_{j=1}^{SN}\int_0^\infty \frac{k^2}{(k+p_i)^2(k-p_i)^2}\left[\beta_j(k) - \beta_j(p_i) - \frac{p^2(k+p_i)(k-p_i)}{2p_i k^2}\beta_j'(p_i)\right], \quad (2.112)$$

and

$$C_{ij} = \beta_j(p_i), \quad (2.113)$$

we get a generalized eigenvalue problem

$$(A_{ij} + V_{ij})\,\alpha_j = EC_{ij}\alpha_j, \quad (2.114)$$

where E are the eigenvalues and α_j the corresponding eigenvectors. Finding the set of Es and the corresponding α_j completely defines the problem of finding the binding energies and the wavefunctions for the bound states.

2.2.6 SDI Method (Splines double integration)

The **SDI method** (Splines double integration) also uses the cubic splines previously defined but now double integrations emerge from the fact that Eq.(2.109) is multiplied in both sides by the operator

$$\int p^2 \beta_l(p) dp. \quad (2.115)$$

This is motivated from the Quantum Mechanics' procedure to find the eigenvalues, using the orthogonality of the basis set of functions. In our case, the basis is not orthogonal so the diagonalizing procedure will not be complete. However, we reduce many of the resulting matrix entrances to zero, facilitating the numerical computation of the eigenvalues.

In this case, the generalized eigenvalue problem is

$$\int_0^\infty dp\frac{p^4}{2m_R}\beta_j(p)\beta_l(p)\alpha_j - \frac{4\sigma}{\pi}\int_0^\infty\int_0^\infty dpdk\frac{p^2k^2}{(k+p)^2(k-p)^2} \times\left[\beta_j(k)\beta_l(p)-\beta_j(p)\beta_l(p)-\frac{p^2(k+p)(k-p)}{2pk^2}\beta_j'(p)\beta_l(p)\right]\alpha_j = E\int_0^\infty dpp^2\beta_j(p)\beta_l(p)\alpha_j. \tag{2.116}$$

Defining now

$$A_{jl} = \int_0^\infty dp\frac{p^4}{2m_R}\beta_j(p)\beta_l(p)\alpha_j, \tag{2.117}$$

$$V_{jl} = -\frac{4\sigma}{\pi}\int_0^\infty\int_0^\infty dpdk\frac{p^2k^2}{(k+p)^2(k-p)^2} \times\left[\beta_j(k)\beta_l(p)-\beta_j(p)\beta_l(p)-\frac{p^2(k+p)(k-p)}{2pk^2}\beta_j'(p)\beta_l(p)\right] \tag{2.118}$$

and

$$C_{jl} = \int_0^\infty dpp^2\beta_j(p)\beta_l(p) \tag{2.119}$$

so

$$\left(A_{jl}+V_{jl}\right)\alpha_j = EC_{jl}\alpha_j \tag{2.120}$$

where once more the E are the eigenvalues and α_j the corresponding eigenvectors and the problem of finding the binding energies and wavefunctions is finished.

2.2.7 Results

In this section we present the results obtained for the solutions of the NRSE in momentum space.

We start with table 2.8 by analyzing the consistency between the results obtained in momentum space for the SSI and the SDI methods described in the text and our previous results of the r-space, for the first five excited states of the $l = 0$ case. Globally, we can state the results are consistent, even though the r- space and SDI method are closer to each other than the SSI method for the same number of splines.

In table 2.9 we make the same analysis for the p and d case. In this situation the method SSI did not provide stable results. But, considering the SDI method, we see that once more the results match in the two spaces.

Since the results for the $l = 0$ case are known and can be determined in terms of the *Airy* function, we investigated the accuracy of our two methods in table 2.10. The results clearly indicate the SDI method as the most accurate.

Another important issue to address when studying numerical methods of this type is to analyze the rate of convergence. For that one can see in Fig.2.9 and 2.10 the relative difference in percentage between the result computed with $SN = 48$ and $SN = 64$ splines as a function of the number of the state. We see that for the SSI Method from around $n = 7$ the values start diverging. On the other hand, for the SDI method, the convergence lasts until approximately $n = 13$. Another interesting feature is that almost cyclically some dips appear, indicating that convergence for some eigenvalues is more easy than others. However, they do not coincide so probably this is related with the intrinsic structure of the method.

E_n	r-space	*SSI*	*SDI*
E_1	2.338107	2.338108	2.338108
E_2	4.087949	4.087930	4.087949
E_3	5.520560	5.520397	5.520560
E_4	6.786793	6.786107	6.786708
E_5	7.947376	7.942539	7.944133

Table 2.8: First binding energies for the s-states. Comparison between the results obtained in the r-space and p-space, for both SSI and SDI method with $SN = 64$.

E_n	r-space	*SDI* ($l = 1$)	r-space	*SDI* ($l = 2$)
E_1	3.361254	3.361258	4.248182	4.248181
E_2	4.884452	4.884456	5.629709	5.629706
E_3	6.207632	6.207627	6.868961	6.688798
E_4	7.406265	7.405669	8.012763	8.009610
E_5	8.528377	8.515238	9.117374	9.076910

Table 2.9: First binding energies for the p-states and d-states. Comparison between the results obtained in the r-space and p-space with the SDI method with $SN = 64$ for the p case and d case.

Obviously, the general behavior is that the convergence worsens with increasing n and this has a physical reason behind it. This happens because the functions evaluated are successively more oscillant, making the integrations harder to converge. As an illustrative example we plot in Fig.2.11 and 2.12 the solutions of wavefunctions corresponding to the ψ_{11}, ψ_{12} and ψ_{13} computed with $SN = 16$ and $SN = 128$. What one notes is that with $SN = 16$ we do not have enough flexibility to represent the right solutions (wavefunctions with 11, 12 and 13 nodes as expected), so a higher number of splines is required. In this case one needs $SN = 128$ to have the desired result (the correct number of nodes).

As a final overall comment, we can say that the SDI Method, has proven to be a robust and efficient method to solve this type of integral equation and if we want to increase the precision or describe higher excited states, we simply have to increase the number of splines in the basis.

A larger set of results can be consulted on Appendix B.

E_n	*SSI*	*SDI*	-Airy zeros
E_1	2.33810847	2.33810761	2.33810741
E_2	4.08793008	4.08794940	4.08794944
E_3	5.52039730	5.52055962	5.52055983
E_4	6.78610688	6.78670794	6.78670809
E_5	7.94253855	7.94413344	7.94413359
E_6	9.01914089	9.02265121	9.02265085
E_7	10.0333347	10.0401766	10.04017434
E_8	10.9962901	11.0085333	11.00852430
E_9	11.9154774	11.9360443	11.93601556
E_{10}	12.7959345	12.8288595	12.82877675
E_{11}	13.6409344	13.6917101	13.69148904
E_{12}	14.4523266	14.5283875	14.52782995
E_{13}	15.2306641	15.3420908	15.34075514
E_{14}	15.9751412	16.1357142	16.13268516
E_{15}	16.6841443	16.9121212	16.90563400
E_{16}	17.3551871	17.6750887	17.66130011
E_{17}	17.9627796	18.4288721	18.40113260
E_{18}	18.5544209	19.1673236	19.16732359
E_{19}	19.2397772	19.9034692	19.83812989
E_{20}	19.4522432	20.7065084	20.53733291

Table 2.10: Accuracy of the SSI and SDI methods. The Airy zeros were found with the software Mathematica 7.0. The results were obtained *SSI* and *SDI* methods with $SN = 64$.

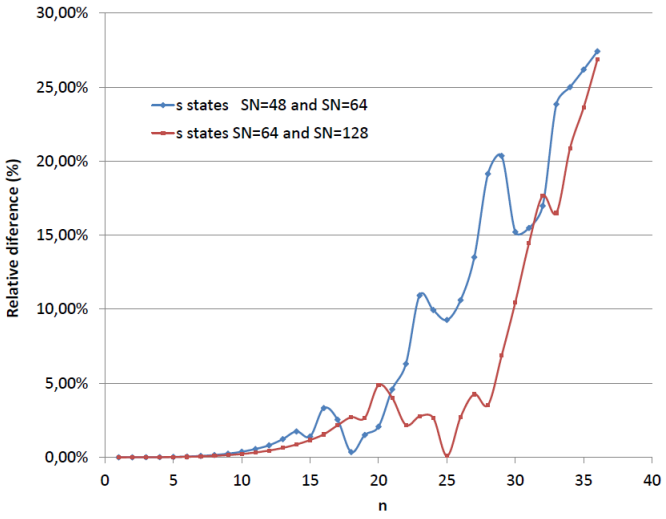

Figure 2.9: Study of convergence in SSI Method. This plot represents in the x axis the n principal quantum number of the state and in the y axis the relative differences in % between the binding energies computed with $SN = 48$ and $SN = 64$ (blue) and $SN = 64$ and $SN = 128$ (red).

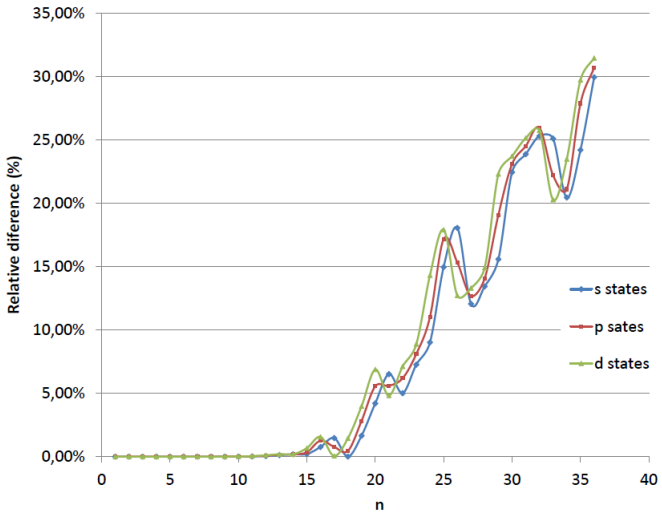

Figure 2.10: Study of convergence in SDI Method. This plot represents in the x axis the n principal quantum number of the state and in the y axis the relative differences in % between the binding energies computed with $SN = 48$ and $SN = 64$.

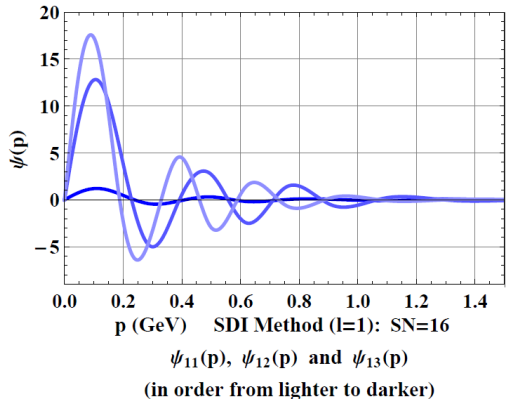

Figure 2.11: Normalized wavefunction of ψ_{11}, ψ_{12} and ψ_{13} with $SN = 16$.

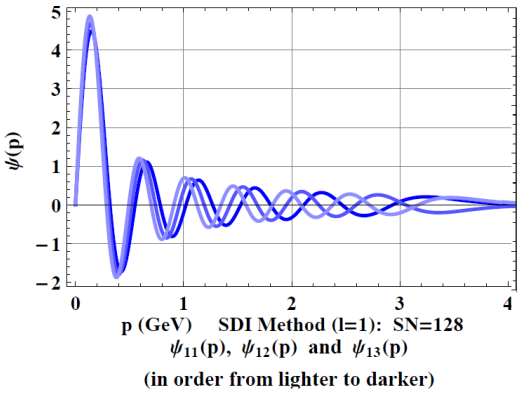

Figure 2.12: Normalized wavefunction of ψ_{11}, ψ_{12} and ψ_{13} with $SN = 128$.

Chapter 3

Relativistic calculation of the meson spectra

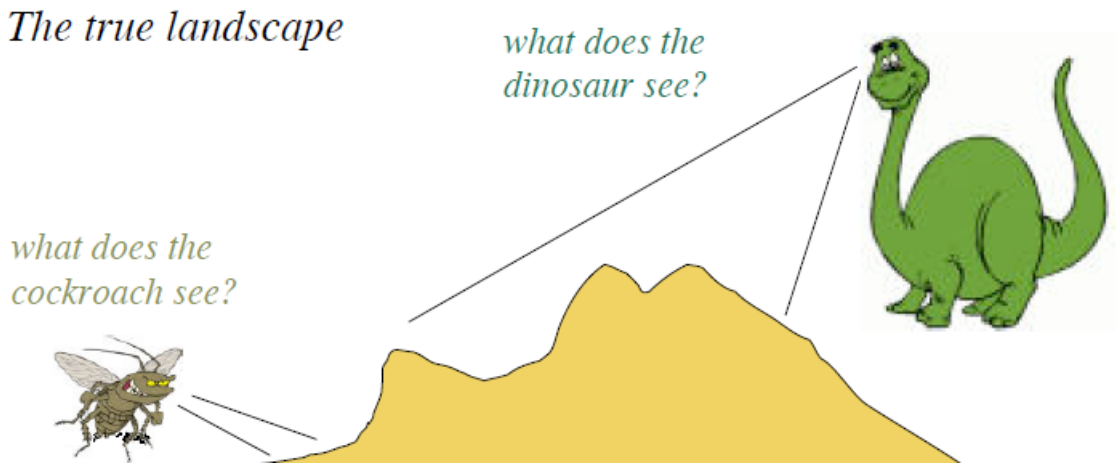

Figure 3.1: What does the dinosaur see?, from "Relativistic Effective Field Theory", Franz Gross, in "INT Program 03-3, Theories of Nuclear Forces and Nuclear Systems, 2003".

In the last chapter we developed a nonrelativistic study of mesons. We found exact solutions of the Schrödinger equation, both in configuration and momentum space, for a general angular momentum ($l = 0$ and $l \neq 0$) orbital state. The results for the momentum space equation were obtained by applying the splines method. Those results were compared and seen to be consistent with the results obtained for the equation in coordinate space. This first study provided us therefore with an opportunity to gain insight and test numerical techniques for calculations in momentum space. We acquired control on numerical methods which are suitable for calculations in momentum space, unavoidable in relativistic approaches. Moreover, this first set of calculations confirmed that a nonrelativistic description is adequate for the heavy mesonic sector, while it is not valid for mesons made of light quarks. The quality of the fits obtained in the light quark sector were substantially worse than those obtained in the heavy quark sector.

In this chapter we will now treat mesons within a Constituent-Quark formalism that is covariant. The importance of the work of the previous chapter will become clear as the details of this more complex approach, and our attempts to solve it, are revealed. As we will see, every time we stumbled with an apparent difficulty, our previous experience gained with the nonrelativistic approach will become

useful.

The formalism that we will concentrate upon is the so-called Covariant Spectator Theory (CST). CST is a relativistic Effective Quantum Field Theory which has been widely used in different types of physical systems, mainly in problems involving static and electromagnetic properties of systems of few nucleons. For bound-states the idea of the CST is to reorganize the manifestly covariant Bethe–Salpeter (BS) equation with its complete kernel to an equivalent form, in which a different propagator, and accordingly a modified kernel, is used. The practical advantage is that the new propagator is chosen such that the dimension of the integration over intermediate momenta reduces from four to three, while maintaining the covariance of the equation.

There are many ways to rearrange the BS equation leading to a dimensional reduction. The resulting equations are called "quasi-potential equations." While the CST belongs to this category, it has properties that not all of the other quasi-potential theories possess. For instance, it satisfies the property of cluster-separability, important to deal with scattering problems. It also has the correct one-body limit: when one particle is very massive compared to the other, the two-body equation reduces to a relativistic one body equation for the light particle moving in an effective potential created by the massive particle. The numerical check of this property of the CST equation provides a good test to our computational methods.

We start this chapter with a brief description of the formalism and the framework of CST (Covariant Spectator Theory), and a review of the Gross and Milana's model ref.[3], a first application of the CST to the study of mesons, with limitations that we will discuss. We present then our results for the the 1CS (One-channel two-body vertex Covariant Spectator) equation in the helicity space for a scalar confining potential. To verify the one-body limit we also investigate how our numeric results evolve in two specific limits:

1. When the mass ratio, $\kappa = \dfrac{m_1}{m_2}$, between the quark and the antiquark, goes to infinity;
2. When on top of the last limit for the mass ratio, the mass of the light particle is also taken to be large.

In the first case we checked that we obtain the results of the Dirac equation for light particle in the field produced by the heavy one. In the second case we checked that we obtain the nonrelativistic results corresponding to the Schrödinger equation.

3.1 Formalism

3.1.1 The Covariant Spectator Theory (CST)

The framework we are interested to work in is based on the CST. The idea behind this theory is that the relativistic series of Feynman diagrams describing any nuclear process can always be reorganized so that only the particles which are interacting are *off-mass-shell*, and all the other particles, which are *spectators* to the interaction, are considered *on-mass-shell*.

In the literature a first work that developed this idea is found in reference [4], where integral equations particularly suitable to the dynamical treatment of strongly interacting particles are derived. These equations were deduced from the Bethe-Salpeter equations following one major assumption:

All the particles of a system, but one, are on the-mass-shell for all the intermediate states. The on-mass-shell particles are viewed, and called, as "spectators" of an interaction vertex. It is the off-mass-shell particle that participates in the vertex of the interaction.

As a consequence of this assumption the complete kernel of the fourth dimensional Bethe-Salpeter equation is turned into an equivalent form, with a different propagator and a kernel modified accordingly. The new propagator is chosen such that, when the kernel of the reorganized equation is truncated to include ladder terms only, the dimension of the integration over intermediate momenta reduces from four to three, while maintaining the covariance of the equation.

This underlying principle of the CST is originally motivated by a very interesting observation: a partial but important *cancellation* occurs between the two-body box and crossed-box diagrams in scalar theories of ϕ^3-type. This cancellation implies that the only terms that survive in any iteration of the exact ladder and crossed kernel terms are the ladder diagrams with one particle on-mass-shell in all intermediate states. At the end, therefore, the integral equation that is obtained sums only ladder diagrams with one particle on-mass-shell in any intermediate state, and consequently is a 3-dimensional reduction of the 4-dimensional Bethe-Salpeter equation. This way, we overcome the impossibility of summing an infinite series of diagrams and get a better approximation by summing only ladder terms where one particle is on mass-shell in all internal loops.

To take a deeper look on this topic lets consider a ϕ^3-type theory including three types of particles: two charged scalar particles with masses m_1 and m_2, and the corresponding fields Φ_1 and Φ_2, and a neutral scalar one with mass μ and field ϕ . The scattering between them, to second order, will have only one contribution, represented in fig.3.2.

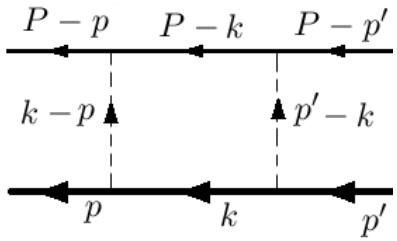

Figure 3.2: The box diagram. The thick line refers to particle 1, the thin line to particle 2 and the dashed lines to the particle being exchanged.

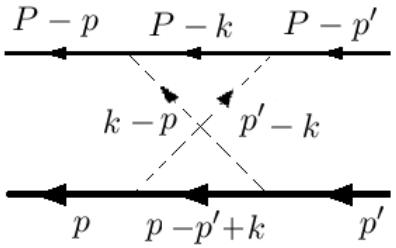

Figure 3.3: The crossed-box diagram. The notation is the same as in Fig.3.2.

It is shown in ref.([35]) that for the case of higher orders, for long range peripheral interactions, the ladder diagrams, i.e. those which replicate the structure of the (OBE) one boson exchange diagram, are the ones with a larger contribution (see fig.3.4).

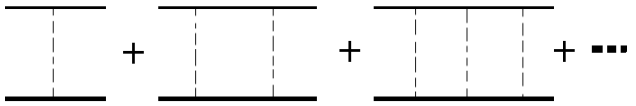

Figure 3.4: The ladder diagrams to sixth order.

Aplying the Feynaman rules for ϕ^3, the scattering amplitude for the box diagram is:

$$\mathscr{M}_{box} = i\lambda_1^2\lambda_2^2 \int \frac{d^4k}{(2\pi)^4} \frac{1}{D_1 D_2 D_0 D_0^{'}}, \tag{3.1}$$

where λ_1 and λ_2 are the coupling constants, assumed here to be small and the poles in the propagator are given by:

$$\begin{aligned}
D_1 = &\quad m_1^2 - (P-k)^2 - i\varepsilon = &\quad E_1^2(k) - (W-k_0)^2 - i\varepsilon \\
D_2 = &\quad m_2^2 - k^2 - i\varepsilon = &\quad E_2^2(k) - k_0^2 - i\varepsilon \\
D_0 = &\quad \mu^2 - (k-p)^2 - i\varepsilon = &\quad \omega^2 - (k_0 - E_2(p))^2 - i\varepsilon \\
D_0^{'} = &\quad \mu^2 - (k-p)^2 - i\varepsilon = &\quad \omega^{'2} - \left(k_0 - E_2(p^{'})\right)^2 - i\varepsilon
\end{aligned} \tag{3.2}$$

We also have $m_1 < m_2$ and $\mu \ll m_1$ and the external particles are on-shell. The diagram is taken to be in the center of mass frame so:

$$\begin{aligned}
E_i(k) &= \sqrt{m_i^2 + \mathbf{k}^2} & \omega &= \sqrt{\mu^2 + (\mathbf{k}-\mathbf{p})^2} \\
E_i(p) &= \sqrt{m_i^2 + \mathbf{p}^2} & \omega' &= \sqrt{\mu^2 + (\mathbf{k}-\mathbf{p}')^2} \\
W &= E_1(p) + E_2(p) \quad = E_1(p') + E_2(p')
\end{aligned} \tag{3.3}$$

Now, factoring the denominators in Eq.(3.1) and representing the poles in the k_0 complex plane we have eight poles, numerated as indicated as follows:

$$\begin{aligned}
D_1 = &\quad \underbrace{(E_1(k) - W - k_0 - i\varepsilon)}_{5} &\quad &\underbrace{(E_1(k) + W - k_0 - i\varepsilon)}_{4} \\
D_2 = &\quad \underbrace{(E_2(k) + k_0 - i\varepsilon)}_{8} &\quad &\underbrace{(E_2(k) - k_0 - i\varepsilon)}_{1} \\
D_0 = &\quad \underbrace{(\omega - E_2(p) + k_0 - i\varepsilon)}_{6} &\quad &\underbrace{(\omega + E_2(p) - k_0 - i\varepsilon)}_{2} \\
D_0^{'} = &\quad \underbrace{\left(\omega' - E_2(p') + k_0 - i\varepsilon\right)}_{7} &\quad &\underbrace{\left(\omega' + E_2(p') - k_0 - i\varepsilon\right)}_{3}
\end{aligned} \tag{3.4}$$

Evaluating the box diagram by choosing a contour in the lower half of the k_0 complex plane, pole 1 is the dominant one, because it is very close to the singularity at $k_0 = W - E_1$, pole 5 in the upper

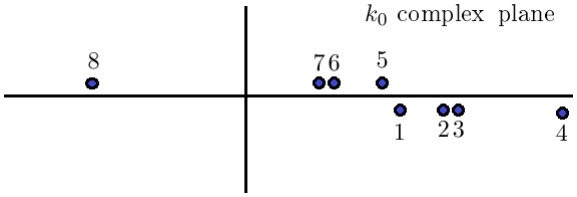

Figure 3.5: The location of the singularities of the box diagram in the complex k_0 plane, when $|\mathbf{k}|$ is small. As $|\mathbf{k}|$ increases, the singularities in the lower half plane move to the right and those in the upper half plane move to the left.

half plane. Keeping this term only, we have:

$$\begin{aligned}\mathscr{M}_{box} &\simeq -\lambda_1^2\lambda_2^2 \int \frac{dk^3}{(2\pi)^3}\frac{1}{2E_2(k)\left[E_1^2(k)-(W-E_2(k))-i\varepsilon\right]}\times \\ &\quad \frac{1}{\left[\omega^2-(E_2(k)-E_2(p))^2\right]\left[\omega'^2-(E_2(k)-E_2(p'))^2\right]} \\ &\simeq \frac{-\lambda_1^2\lambda_2^2}{4m_1m_2}\int\frac{dk^3}{(2\pi)^3}\frac{1}{[E_1(k)+E_2(k)-W-i\varepsilon]\,\omega^2\omega'^2},\end{aligned} \tag{3.5}$$

where $E_2(k)$ was approximated by $E_2(k)\sim m_2$ and $E_1(k)+W-E_2(k)\sim 2m_1$.

We can now estimate the value of the integral by taking the case when m_1 and m_2 are both very large and $\mathbf{p}=\mathbf{p}'$, corresponding to the scattering in the forward direction. The integral is cut off by the energies $\omega=\omega'$, and $k=|\mathbf{k}|\simeq\mu$, making it possible to expand the energies in the integrand as $E_1(k)\simeq m_1+\dfrac{k^2}{2m_1}$.

This way, for large m we have:

$$\begin{aligned}\mathscr{M}_{box} &\simeq \frac{-\lambda_1^2\lambda_2^2}{4m_1m_2}\int\frac{dk^3}{(2\pi)^3}\frac{2m}{(k^2-p^2-i\varepsilon)\left(\mu^2+(\mathbf{k}-\mathbf{p})^2\right)^2} \\ &= \frac{-\lambda_1^2\lambda_2^2}{4m_1m_2}\int_0^\infty\frac{k^2dk}{2\pi^2}\frac{2m}{(k^2-p^2-i\varepsilon)\left((k^2+p^2+\mu^2)^2+4k^2p^2\right)} \\ &= \frac{-\lambda_1^2\lambda_2^2}{16\pi}\frac{1}{(m_1+m_2)\,\mu^2}\left(\frac{1}{\mu-2ip}\right).\end{aligned} \tag{3.6}$$

where m is the reduced mass and the integral was evaluated in the last step by extending k to $-\infty$ and using the residues theorem.

However, if we now consider the crossed-box diagram as shown in fig.3.3 and follow the labeling suggested in it, the only difference from the the scattering amplitude of the box diagram Eq.(3.1) is the momentum of the internal propagator for particle 2, so

$$\mathscr{M}_{crossed-box}=i\lambda_1^2\lambda_2^2\int\frac{d^4k}{(2\pi)^4}\frac{1}{D_1D_2^\times D_0D_0'} \tag{3.7}$$

and D_1, D_0 and D_0' are identical to those defined on Eq.(3.1.1), but

$$\begin{aligned} D_2^{\times} &= m_2^2-(p+p'+k)^2-i\varepsilon \\ &= \underbrace{\left(E_2^{\times}(p)+2E_2(p)-k_0-i\varepsilon\right)}_{8_{\times}} \underbrace{\left(E_2^{\times}(p)+2E_2(p)+k_0-i\varepsilon\right)}_{1_{\times}} \end{aligned} \tag{3.8}$$

where

$$E_2^{\times}(p)=\sqrt{m_2^2+(\mathbf{p}+\mathbf{p}'+\mathbf{k})^2} \tag{3.9}$$

There are still eight poles in the complex k_0 plane, but two of the poles, $1_{\times}$ and $8_{\times}$, have different locations, as shown in fig.(3.6). Ignoring poles 8 and $8_{\times}$, which are negligible, the major difference between the boxed and crossed-box, is that the pole 1, which dominate the box, has moved from the lower half plane to the upper half plane. These two poles are located at:

- pole1: $k_0=E_2-i\varepsilon\cong m_2+\dfrac{k^2}{2m_2}-i\varepsilon$;
- pole $1_{\times}$: $k_0=2E_2(p)-E_2^{\times}\cong m_2+\dfrac{p^2}{2m_2}-\dfrac{(\mathbf{p}+\mathbf{p}'+\mathbf{k})^2}{2m_2}+i\varepsilon$.

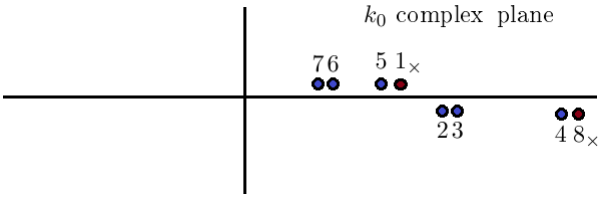

Figure 3.6: The location of the singularities of the crossed-box diagram in the complex k_0 plane.

Introducing $k_0=k_0'+E_2(p)$, these two denominators become

- box: $\dfrac{1}{D_2}\cong\dfrac{1}{2m_2\left(\dfrac{k^2-p^2}{2m_2}-k_0'\right)}$;
- crossed-box: $\dfrac{1}{D_2^{\times}}\cong\dfrac{1}{2m_2\left(\dfrac{(\mathbf{p}+\mathbf{p}'+\mathbf{k})^2}{2m_2}-\dfrac{p^2}{2m_2}+k_0'\right)}$.

If m_2 is very large, the terms in the denominators proportional to m_2^{-1} may be neglected compared to k_0' (which is equal to ω or ω' at the poles), and we see that

$$\frac{1}{D_2}\cong\frac{-1}{D_2^{\times}} \tag{3.10}$$

Hence, in this approximation the dominant contributions from the crossed-box are equal to the contributions of the box but have opposite sign, so that their sum (box plus crossed-box **cancels**).

In fact this cancellation is quite general (see ref.[35]) originating the following theorem:

Cancellation Theorem

In a theory in which a spin zero particle of mass m_1 interacts with a heavy particle of mass m_2 (which has no charge states) by exchanging a spin zero meson of mass μ, the meson pole contributions from the ladder diagram are canceled by the meson pole contributions from crossed-ladder diagrams, and this cancellation is exact in the limit as $m_2 \to \infty$.

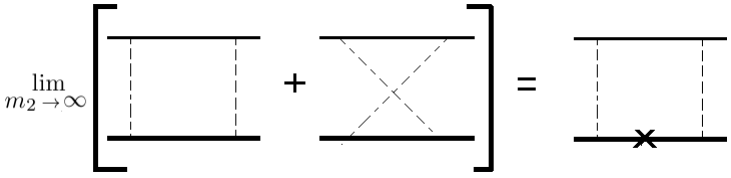

Figure 3.7: Illustration of the cancellation theorem. The cross means that the heaviest particle is on its mass shell.

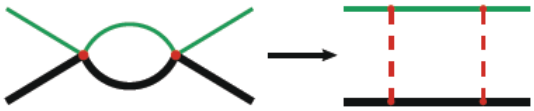

Figure 3.8: The relation of the s-channel bubble diagram to the box diagram when the four-point vertex is "opened" and transformed into a boson exchange

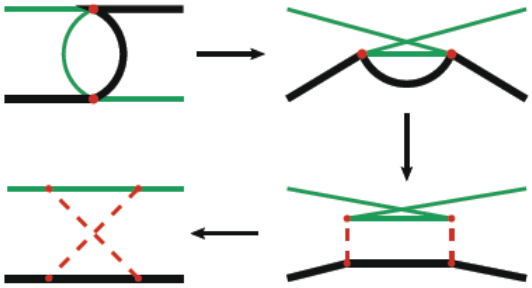

Figure 3.9: The relation of the u-channel bubble diagram to the box diagram when the four-point vertex is "opened" and transformed into a boson exchange

An interesting confirmation of this theorem was presented in ref.([7]) where now the authors considered, instead of ϕ^3-theory a ϕ^4-type theory, with two scalar fields, one neutral with mass M called ψ,and one charged with mass $m < M$ called ϕ, interacting through $\mathscr{L}_{\mathscr{I}} = -\lambda\phi^\dagger\phi\psi^2$. In fact the ϕ^4-type theory can be interpreted as limits of ϕ^3-type theories with an infinite mass being exchanged, as illustrated in fig.3.8 and fig.3.9. When the 4-point vertex function is "opened" to represent a one-boson exchange, the s-channel diagram becomes the box diagram, and the u-channel, after some additional deformation without changing its topology, becomes the crossed-box diagram.

We emphasize that the complete kernel of the CST equation contains an infinite number of irreducible diagrams, which makes it formally equivalent to the BS equation. It is only when the kernel is truncated, that exact equivalence to the full BS equation is lost. However, this would only be an

issue if one attempted to find an exact solution of a field theory for a given Lagrangian. Instead, the equations of CST can be taken as the starting point for a description of few-body systems that is in part phenomenological; they are based on certain physical mechanisms, such as one-boson exchange (OBE), but they have phenomenological aspects in the way integrations are regularized, and in the use of parameters, some of which have to be determined from fits to experimental data.

3.1.2 A CST model for mesons

The GM model (ref.[3]) is the first covariant model that appeared as an application of the CST to the bound state of a quark+antiquark system. We review here the main features of this model:

1. Mesons are interpreted as bound-states of a quark and an antiquark, either one of which can be *off-shell*. The model is a **relativistic** generalization of the nonrelativistic (or semirelativistic) models of Godfrey and Isgur (ref.[36]).

2. The relativistic bound state equation is written in momentum space, where nonlocalities and energy dependences of the interactions can be taken into account more easily.

3. The **confining potential** has a **linear part** that is known to emerge, in the quenched approximation, from lattice QCD calculations, and a **constant part** that enables an adjustment of the overall energy scale. In momentum space this potential has a leading term in q^{-4}, that is regularized by subtracting the leading singularity at $q^2 = 0$. This potential is multiplied by a $\lambda_1.\lambda_2$ factor to account for the color part.

4. The spin-dependent structure of the confining potential is chosen to be consistent with **chiral symmetry**. The authors explored the *simplest* case of chiral symmetry under the $SU(2) \times SU(2)$ group and also under the $U(1) \times U(1)$ group case.

5. Following the ideas of NJL models (ref.[37]) in which chiral symmetry is spontaneously broken, the constituent quark mass arises dynamically from its self-interaction with the confining forces. Considering the pion, its nonzero mass is theoretically a natural consequence of **chiral symmetry breaking** generating a sizable quark mass from the originally almost zero bare quark mass of the QCD Lagrangian. However, in the numerical calculations, this consistency between confinement and chiral symmetry was not yet fully implemented.

6. In the relativistic equation for the bound state the relative energy variable is constrained by restricting one of the quark to its positive energy mass-shell — this is called the one-channel case. This means that despite the fact that the equations are covariant, they depend, like nonrelativistic equations, on the relative three momentum only and have a smooth nonrelativistic limit so they are expected to describe most accurately the **heavy-light** deeply bound systems.

7. For the case of **not very deeply bound states**, two channels have to be included, one with the quark on its positive-energy mass-shell and one with the antiquark on its negative energy mass-shell. This point will be seen in more detail on the next section.

3.1.3 The one-channel vertex spectator 1CS equation

We will proceed now to consider in detail the case of the one-channel spectator equation. Following the features just described, we take here the meson as a bound state of a quark and an anti-quark, and write down the Feynman diagram for the bound state meson vertex equation has shown in Fig.(3.10).

Particle 1 is the quark, particle 2 the antiquark and $\mathscr{O}$ is a matrix in the Dirac space that describes how the confining force couples to the quark or antiquark. The kernel V contains the momentum dependent structure of the confining potential. The equations are derived in the center of mass rest frame, where $P = (\mu, \mathbf{0})$.

Later, the quark (particle 1) will be placed on shell, thus producing the single channel equation. The four momenta used in the diagram in terms of the total four-momentum $P = p_1 - p_2$, and the relative momentum $p = \frac{1}{2}(p_1 + p_2)$ are:

$$\begin{aligned} \text{final state:} \qquad & p_1 = p + \frac{1}{2}P \quad p_2 = p - \frac{1}{2}P, \\ \text{internal loop:} \qquad & k_1 = k + \frac{1}{2}P \quad k_2 = k - \frac{1}{2}P, \end{aligned} \tag{3.11}$$

where p_1 refers to the quark and p_2 refers to the anti-quark (which has a minus sign).

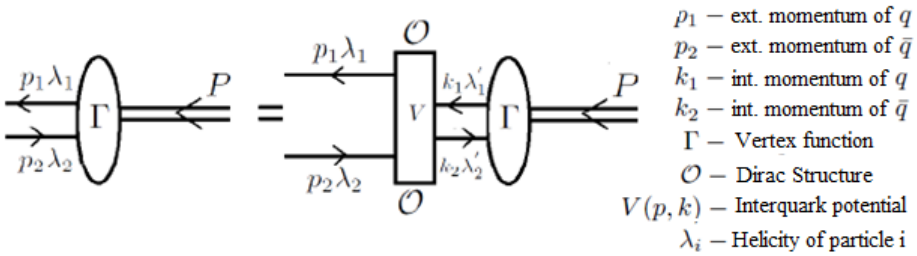

Figure 3.10: Diagrammatic representation of the Bethe-Salpeter equation for the meson bound-state vertex function Γ. The kernel, or potential, is denoted by V.

With this notation, the Bethe-Salpeter equation for the bound state vertex function of a meson, where the quark-antiquark interaction has a general Dirac vertex structure $\mathscr{O}$, is:

$$\Gamma(p) = i\int \frac{d^4k}{(2\pi)^4} V(p,k)\mathscr{O}\frac{m_1 + \not{k}_1}{m_1^2 - k_1^2}\Gamma(k)\frac{m_2 + \not{k}_2}{m_2^2 - k_2^2}\mathscr{O}. \tag{3.12}$$

Poles in the propagators

The two fermion propagators have poles that can be represented in the complex plane k_0. Factoring the denominators of the propagators as:

$$\frac{1}{m_i^2 - k_i^2} = G_i^+ G_i^-, \tag{3.13}$$

we have the following poles:

$$\begin{aligned}
&\text{pole 1} \quad \left(G_1^+\right)^{-1} = E_{k1} - \left(k_{10} + \frac{1}{2}\mu\right) - i\varepsilon \qquad k_{10} = E_{k1} - \frac{1}{2}\mu - i\varepsilon \\
&\text{pole 2} \quad \left(G_2^+\right)^{-1} = E_{k2} - \left(k_{20} - \frac{1}{2}\mu\right) - i\varepsilon \qquad k_{20} = E_{k2} + \frac{1}{2}\mu - i\varepsilon \\
&\text{pole 3} \quad \left(G_1^-\right)^{-1} = E_{k1} + \left(k_{30} + \frac{1}{2}\mu\right) - i\varepsilon \quad k_{30} = -E_{k1} - \frac{1}{2}\mu + i\varepsilon \\
&\text{pole 4} \quad \left(G_2^-\right)^{-1} = E_{k2} + \left(k_{40} - \frac{1}{2}\mu\right) - i\varepsilon \quad k_{40} = -E_{k2} + \frac{1}{2}\mu + i\varepsilon.
\end{aligned} \tag{3.14}$$

They are represented in Fig.(3.11).

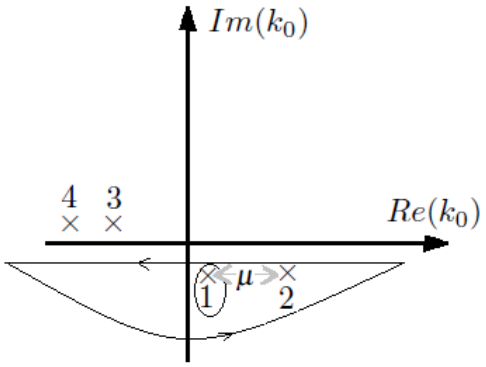

Figure 3.11: Position of the four poles associated with the four propagators G_i^ρ in the bound state equation.

Performing the k_0 integration in a closed contour in the lower half plane, we may keep only the residue from pole 1. This is a good approximation when μ small, since the pole 1 is in the close vicinity of pole 3 — where the integrand is large — and therefore 1 is the dominating contribution from the lower half plane poles.

$$\Gamma(p) = -\int \frac{d^3k}{2E_{k1}(2\pi)^3} V(p,k)\mathscr{O}(m_1 + \hat{\not{k}}_1)\Gamma(k)\frac{m_2 + \not{k}_2}{m_2^2 - k_2^2}\mathscr{O}, \tag{3.15}$$

where now $\hat{k}_1 = (E_{k1}, \mathbf{k})$[1] and $k_2 = (E_{k1} - \mu, \mathbf{k})$.

This is one form of the **One Channel Spectator equation**, labeled for short, the **1CS** equation.

Recalling that the projection operator (see ref.[35]) can be written[2]:

$$m_1 + \hat{\not{k}}_1 = \sum_{\lambda'} u\left(\mathbf{k}, \lambda'\right) \bar{u}\left(\mathbf{k}, \lambda'\right), \tag{3.16}$$

as a sum over on-shell u spinors, we have:

$$m_1 + \not{k}_1 = \sum_{\lambda'} u\left(\mathbf{k}, \lambda'\right) \bar{u}\left(\mathbf{k}, \lambda'\right). \tag{3.17}$$

[1] The hat on k_1 means the particle is on-shell.

[2] where $u(\mathbf{p}, \lambda) = \sqrt{E_p + m}\begin{pmatrix} 1 \\ \frac{\sigma.\mathbf{p}}{E_p + m} \end{pmatrix}\chi^\lambda$

Defining now the relativistic meson wave function as

$$\Psi(k,\lambda) = \frac{1}{\sqrt{2E_{k1}}}\bar{u}(\mathbf{k},\lambda)\,\Gamma(k)\,\frac{m_2 + \not{k}_2}{m_2^2 - k_2^2}, \tag{3.18}$$

Eq. (3.15) becomes:

$$\Psi(p,\lambda)\,(m_2 - \not{p}_2) = -\int \frac{d^3k}{(2\pi)^3}\frac{V(p,k)}{\sqrt{4E_{p1}E_{k1}}}\sum_{\lambda'}\bar{u}(\mathbf{p},\lambda)\,\mathscr{O}u\left(\mathbf{p},\lambda'\right)\Psi(k,\lambda')\mathscr{O}. \tag{3.19}$$

An important remark about how the vertex equation was deduced in the CST can now be done. The real question is always which poles should be kept. We are not aware of a simple prescription that satisfactorily determines all possible cases for all systems. The basic idea is to perform the energy integration in the Bethe-Salpeter equation by picking out only the dominant poles of the particle propagators in the intermediate states. Which and how many poles are dominant depends on the system under consideration. For instance, in an effective two-body description of nucleon-nucleus scattering one pole dominates, namely the positive-energy pole of the heavier nucleus, whereas in the case of light mesons the quark and antiquark poles can be very close to each other, such that there is no justification for neglecting one of them. In nucleon-nucleon scattering the positive-energy poles of both nucleons contribute for a different reason, namely because the equations have to be antisymmetric under particle interchange. Another example is charge conjugation symmetry: It is usually not of particular importance if the two-nucleon amplitudes are symmetric under charge conjugation, but a quark-antiquark bound-state wave functions definitely should be charge-conjugation invariant. To achieve this, poles in both half planes have to be included. Thus, already in these examples one can obtain one-, two-, or four-channel equations, all of which can be considered as CST equations, but with different properties.

The 1CS one-body (Dirac) limit

In this section we want to show the reduction of the 1CS equation to the one body Dirac equation, theoretically. At the end of the chapter we will show that our numerical results are consistent with this limit.

We start by defining:

$$\mathscr{O}^{++}_{\lambda\lambda'}(p,k) \equiv \bar{u}(\mathbf{p},\lambda)\,\mathscr{O}u\left(\mathbf{p},\lambda'\right), \tag{3.20}$$

and so:

$$\boxed{\Psi(p,\lambda)\,(m_2 - \not{p}_2) = -\int \frac{d^3k}{(2\pi)^3}\frac{V(p,k)}{\sqrt{4E_{p1}E_{k1}}}\sum_{\lambda'}\mathscr{O}^{++}_{\lambda\lambda'}(p,k)\Psi(k,\lambda')\mathscr{O}.}$$

Let us now rewrite this equation in a form closer to the Dirac form by taking its transpose and multiplying it by the Dirac charge conjugation matrix [3] C. One obtains

$$(m_2 + \not{p}_2)\,\hat{\Psi}(p,\lambda) = -\hat{\mathscr{O}}\sum_{\lambda'}\int \frac{d^3k}{(2\pi)^3}\hat{\Psi}(k,\lambda')\frac{V(p,k)}{\sqrt{4E_{p_1}E_{k_1}}}\bar{u}(\mathbf{p},\lambda)\,\mathscr{O}u\left(\mathbf{k},\lambda'\right), \tag{3.21}$$

[3] $C = \begin{pmatrix} 0 & -i\sigma_2 \\ -i\sigma_2 & 0 \end{pmatrix}$, and σ_2 is the usual Pauli matrix.

where

$$\hat{\Psi}(p,\lambda) = C\Psi^T(p,\lambda) \quad , \quad \hat{\mathscr{O}} = C\mathscr{O}^T C^{-1}. \tag{3.22}$$

We need now to compute the matrix element $\mathscr{O}^{++}_{\lambda\lambda'}(p,k) = \bar{u}(\mathbf{p},\lambda)\,\mathscr{O} u(\mathbf{k},\lambda')$ explicitly. We considered $\mathscr{O}$ to be the unit matrix and chose to work in the Helicity Space. A further discussion can be seen both in ref.[38] and in Appendix A of this thesis. Here we only give the result, namely:

$$\bar{u}(\mathbf{p},\lambda)\,\mathscr{O} u\left(\mathbf{k},\lambda'\right) = N_{p_1}N_{p_2}\left(\delta_{\lambda\lambda'}\cos\frac{1}{2}(\theta-\theta') - 2\lambda\,\delta_{\lambda,-\lambda'}\sin\frac{1}{2}(\theta-\theta')\right)\left(1+4\lambda'\lambda\tilde{p}_1\tilde{k}_1\right). \tag{3.23}$$

N_{p_1}, N_{p_2}, λ, λ', θ, θ', $\tilde{p}_1$ and $\tilde{k}_1$ are properly defined on Appendix A.

If we define now the following two independent linear combinations:

$$\begin{array}{l} \Phi^+(p) = \hat{\Psi}\left(p,\frac{1}{2}\right)\cos\frac{1}{2}\theta' - \hat{\Psi}\left(p,-\frac{1}{2}\right)\sin\frac{1}{2}\theta', \\ \Phi^-(p) = \hat{\Psi}\left(p,\frac{1}{2}\right)\sin\frac{1}{2}\theta' + \hat{\Psi}\left(p,-\frac{1}{2}\right)\cos\frac{1}{2}\theta', \end{array} \tag{3.24}$$

Eq.(3.21) becomes equivalent to the set of equations

$$\begin{cases} (m_2+\not{p}_2)\Phi^+(p) = -\hat{\mathscr{O}}\int\frac{d^3k}{(2\pi)^3}\frac{N_{p_1}N_{k_1}}{\sqrt{4E_{p_1}E_{k_1}}}V(p,k)\left(\Phi^+(p)\left[1+\tilde{p}_1\tilde{k}_1\cos(\theta-\theta')\right]+\Phi^-(k)\tilde{p}_1\tilde{k}_1\sin(\theta-\theta')\right), \\ (m_2+\not{p}_2)\Phi^-(p) = -\hat{\mathscr{O}}\int\frac{d^3k}{(2\pi)^3}\frac{N_{p_1}N_{k_1}}{\sqrt{4E_{p_1}E_{k_1}}}V(p,k)\left(\Phi^-(p)\left[1+\tilde{p}_1\tilde{k}_1\cos(\theta-\theta')\right]-\Phi^+(k)\tilde{p}_1\tilde{k}_1\sin(\theta-\theta')\right). \end{cases} \tag{3.25}$$

Now we can observe that taking the limit $m_1 \to \infty$ gives a Dirac equation for the light particle. The fixed source for the Dirac equation is the heavy quark. As $m_1 \to \infty$, $\tilde{p}_1 \to 0$ and $V(p,k) \to V(\mathbf{p}-\mathbf{k})$ and this gives

$$\left(m_2+\not{p}_2'\right)\Phi(p) = -\hat{\mathscr{O}}\int\frac{d^3k}{(2\pi)^3}V(\mathbf{p}-\mathbf{k})\Phi(k), \tag{3.26}$$

where the helicity of the heavy particle was dropped because the equation is independent of it and we introduced the physical momentum, $p_2' = -p_2 = (\mu - E_{p_1}, -p) \to (E_B, \mathbf{p}')$ with $E_B = \mu - m_1$.

We conclude that the 1CS has the proper on-body Dirac limit when the mass of the heaviest particle is taken to infinity: it gives the Dirac equation for the light anti-particle moving under the influence of a potential that is created by the heavy quark.

3.1.4 The two-channel vertex spectator 2CS equation

As explained in section 3.1.3 in the case of not deeply bound states, i.e., a very small bound state mass is (i.e. $\mu \ll m_i$), pole 2 in figure 3.11 is as important as pole 1, and two-channels must be included in the formalism, corresponding to quark and anti-quark taken on their positive mass-shell. In this case Eq. (3.12) becomes unsuitable for the description of the pion, given its very small mass. and there will then be two components of the vertex function, Γ_1 and Γ_2, corresponding respectively to the quark and the anti-quark on-mass-shell. The set of equations that define those components is represented in Fig.(3.12). One writes then

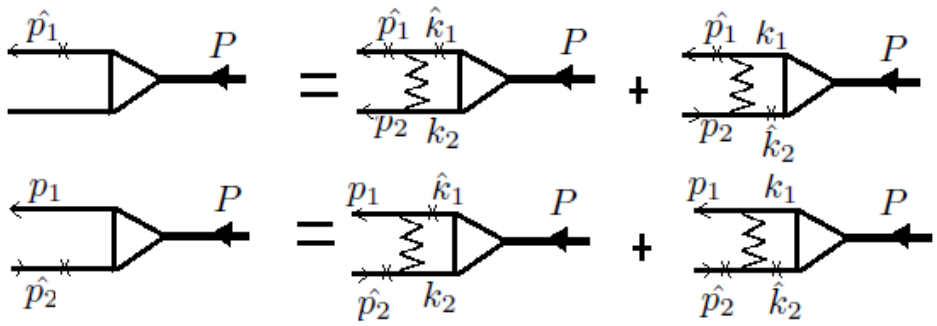

Figure 3.12: The zigzag line represents the kernel, which in this paper is the sum of a confining interaction and the exchange of another particle. A cross on a quark line indicates that the particle is on mass shell.

$$\begin{aligned}\Gamma_1(p,P) &= -\int \frac{d^3k}{(2\pi)^3}\left[V_{11}(p,k;P)\frac{\Gamma_1(k,P)}{2E_k-\mu}+V_{12}(p,k;P)\frac{\Gamma_2(k,P)}{2E_k+\mu}\right],\\ \Gamma_2(p,P) &= -\int \frac{d^3k}{(2\pi)^3}\left[V_{21}(p,k;P)\frac{\Gamma_1(k,P)}{2E_k-\mu}+V_{22}(p,k;P)\frac{\Gamma_2(k,P)}{2E_k+\mu}\right],\end{aligned} \tag{3.27}$$

For each of the four potential channels, $V_{11}, V_{12}, V_{21}, V_{22}$ the square of the four-momentum transfer $(p-k)^2$ is

$$\begin{aligned}q^2 &= (E_p-E_k)^2-(\mathbf{p}-\mathbf{k})^2 \text{ (for } V_{11} \text{and } V_{22});\\ q^2 &= (E_p-E_k-\mu)^2-(\mathbf{p}-\mathbf{k})^2 \text{ (for } V_{12});\\ q^2 &= (E_p+\mu-E_k)^2-(\mathbf{p}-\mathbf{k})^2 \text{ (for } V_{21}).\end{aligned} \tag{3.28}$$

Observable	Calculated (MeV)	Experimental (MeV)
m_π	140	139.6
m_η	320	
m_π^*	1118	1300 ± 100
m_K	495	495
m_χ	376	
$m_u=m_d$	360	
m_s	588	

Figure 3.13: Summary of ref.[10] results.

Finally, if the quark masses are identical, one has to impose invariance under charge-conjugation, or quark-antiquark exchange: interchange of the momenta $p_1 \to p_2$, together with taking the transpose of the vertex function. This originates 4 channel equations. It is out of the scope of this thesis to study and solve either the 2CS or its 4 channel charge-conjugated symmetric version. Just for reference, in ref.[10] the GM model, where a phenomenological quark mass function is used, solved both cases. Very reasonable results for pions and kaons were obtained in that reference as shown in the table. This is a motivation to proceed to the next stage — where the quark mass function is consistently calculated

—since the formalism, designed to work well in the heavy quark sectors, can also be extended to the light quark sector.

3.1.5 Choosing a convenient relativistic potential for the $q\bar{q}$ interaction

The confining potential has a linear and a constant part to set the scale. Lets consider first the linear part, that in the nonrelativistic case is simply given by:

$$V(r) = \sigma r. \tag{3.29}$$

From section 2.2.1, we already know how to treat this potential in the momentum space, so we will simply rewrite it here

$$V_L(\mathbf{q}) = \lim_{\varepsilon \to 0} \left[V_A(\mathbf{q}) - (2\pi)^3 \delta^{(3)}(\mathbf{q}) \int \frac{d^3\mathbf{q}'}{(2\pi)^3} V_A(\mathbf{q}') \right], \tag{3.30}$$

where $\mathbf{q}$ is the momentum transfer, and

$$V_A(\mathbf{q}) = -\frac{8\pi\sigma}{(\mathbf{q}^2 + \varepsilon^2)^2}. \tag{3.31}$$

Relatively to the the constant part, it appears to adjust the mass scale. In momentum space this corresponds to

$$V_C(\mathbf{q}) = (2\pi)^3 \delta(\mathbf{q}) 2 m_R C, \tag{3.32}$$

where m_R is the reduced mass of the $q\bar{q}$ system, and C is a dimensionless constant. The total potential V_T is then:

$$V_T = V_C + V_L. \tag{3.33}$$

A possible way to give this non-relativistic potential a relativistic form would be to replace the nonrelativistic $\mathbf{q}$ by the relativistic $q^2 = q_0^2 - \mathbf{q}^2$, with arbitrary q_0. However, if one of the two quarks is very massive, the energy q_0 transferred to it is expected to be small, so that the nonrelativistic limit should emerge. However this doesn't happen if q_0 is left unconstrained, and no assumption is made on its dependence on the heavy quark mass. In fact, one way to maintain covariance exactly, and also to allow the nonrelativistic limit to emerge naturally, is to restrict the heavy quark to its mass shell, so that the four-momentum transfer becomes

$$\mathbf{q} \to \mathbf{q^2} = (\mathbf{E_p} - \mathbf{E_k})^2 - (\mathbf{p} - \mathbf{k})^2, \quad \mathbf{E_p} = \sqrt{\mathbf{m_1^2} + \mathbf{p^2}}, \tag{3.34}$$

where m_1 is the mass of the heavy quark. The energy transfer now automatically approaches zero as $m_1 \to \infty$. As we have seen, to consider the quark on-mass-shell is justified even away from this mass limit, if poles 1 and 2 in fig.3.11 of the iterated potential (defining one loop diagrams) are sufficiently far apart, what happens when $\mu \ll m_i$. The generalization defined by Eq.3.34 is therefore also consistent with the choice made on which poles to be included in the iteration of the potential.

In reference [3] the potential used for the generalization of the relativistic case for spin-$\frac{1}{2}$ particles was:

$$V(p,k;P) = V_{eff}(p,k;P) \sum_i O_1^i O_2^i, \tag{3.35}$$

where the Dirac matrices O, which operate on the Dirac indices of particles 1 and 2, describe the spin-dependent structure of the kernel, and V_{eff}, a covariant scalar function, gives the momentum dependence of the effective confining potential and is given by

$$V_{eff}(p,k;P) = V_A(p,k) - E_k\delta(\mathbf{p}-\mathbf{k})\int \frac{d^3k'}{E_{k'}} V_A(p,k') + C(2\pi)^3 E_k\delta(\mathbf{p}-\mathbf{k}), \tag{3.36}$$

and

$$V_A(p,k) = -8\pi\sigma\frac{1}{(p-k)^4}, \tag{3.37}$$

Notice that the E_k and $E_{k'}$ energy factors ensure that the potential is explicitly covariant. This covariance is evident since an integral over $\int \frac{d^3k}{2E_k}$ can be expressed as $\int d^4k\delta_+(m_1^2-k_1^2)$.

3.1.6 Chiral Symmetry

It is believed that the pion, the lightest of mesons, is the Goldstone boson associated with the breaking of chiral symmetry of the QCD Lagrangian. The model tries to explain its emergence through a generalization of the Nambu-Jona-Lasinio (ref.[37]) mechanism. In fact, what the model guarantees is that the dynamical generation of quark mass in the limit when the "bare", or undressed, quark mass is exactly zero (the so called *chiral limit*) is be accompanied by the existence of a pseudoscalar bound state of zero mass (precisely the pion).

This occurs, as it will be explained in this section, because the Dyson equation for the dynamical generation of quark mass and the two equation for a pseudoscalar bound state of zero mass are **identical** in the limit when the current quark mass is zero, and hence the existence of a solution for one implies a solution for the other. This identity can be illustrated diagrammatically by realizing that the diagram for the 2-body vertex in Fig.(3.15) in the case of total four-momentum ($P = P_0, \vec{P} = 0$) reduces to the one-body diagram in Fig.(3.14). We will now present the analytical proof of this correspondence.

We start by considering the self-consistent Dyson equation for the quark self-energy, represented squematically in Fig.(3.14) and defined by:

$$\Sigma(p) = \not{p}\Sigma^v(p) + \Sigma^s(p), \tag{3.38}$$

From Fig.(3.14) this leads to

$$\not{p}\Sigma^v(p) + \Sigma^s(p) = i\int \frac{d^4k}{(2\pi)^4} V_{eff}(p-k)\sum_i \mathscr{O}_i^\pi \frac{1}{\not{k} - m_0 - \Sigma(k)}\mathscr{O}_i^\pi, \tag{3.39}$$

where m_0 is the "bare" mass of the quark.

We next write down the bound-state equation for two dynamical quarks using ladder approximation, shown schematically in Fig.(3.15). Defining the vertex function, $\Gamma(p,P)$, as:

$$\Gamma(p,P) = i\int \frac{d^4k}{(2\pi)^4} V_{eff}(p-k)\sum_i \mathscr{O}_i^\pi S\left[k+\frac{P}{2}\right]\Gamma(k,P)S\left[k-\frac{P}{2}\right]\mathscr{O}_i^\pi, \tag{3.40}$$

where

$$S(q) = \frac{1}{\not{q} - m_0 - \Sigma(q)}. \tag{3.41}$$

There is not however, one unique choice for the spinor structure, $\{\mathscr{O}^\pi\}$, of the interaction compatible with this condition. We can study two possible structures.

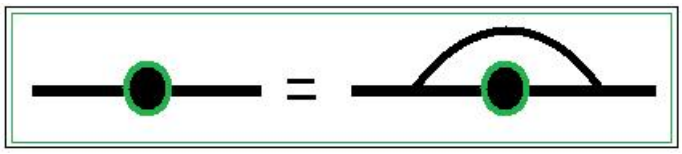

Figure 3.14: Self-consistent Dyson equation for the quark selfenergy. Blobs represent the full quark propagator, while the heavy thick line schematically represents the potential.

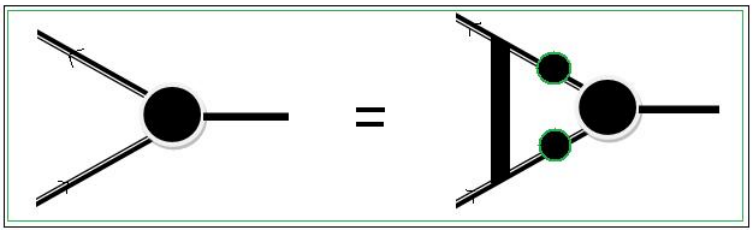

Figure 3.15: Equation for the vertex function.

Chiral symmetry with $\mathscr{O}^\pi$ symmetric under $SU(2)\times SU(2)$ group

Defining $\mathscr{O}^\pi$ by imposing that:

$$\sum \mathscr{O}_i^\pi \mathscr{O}_i^\pi = 1 - \gamma_1^5 \gamma_2^5 \tau_1 \tau_2, \tag{3.42}$$

i.e., the sum of scalar-isoscalar and pseudoscalar-isovector exchange terms. The self-energy equation then becomes

$$\begin{aligned} \Sigma^s(p) &= -2i \int \frac{d^4k}{(2\pi)^4} V_{eff}(p-k) \frac{m_0 + \Sigma^s(k)}{k^2 \left[1-\Sigma^v(k^2)\right]^2 - \left[m_0+\Sigma^s(k)\right]^2}, \\ p\Sigma^v(p) &= 4i \int \frac{d^4k}{(2\pi)^4} V_{eff}(p-k) \frac{p.k\left[1-\Sigma^v(k)\right]}{k^2 \left[1-\Sigma^v(k^2)\right]^2 - \left[m_0+\Sigma^s(k)\right]^2}. \end{aligned} \tag{3.43}$$

With the same interaction, the bound-state equation for a zero-mass ($(P_0,\vec{P}) = (0,0)$) pion with a vertex function of the form

$$\Gamma(p,0) = \Gamma_0(p)\tau\gamma^5 \tag{3.44}$$

is

$$\begin{aligned} \Gamma_0(p)\tau\gamma^5 =& i\tau \int \frac{d^4k}{(2\pi)^4} \frac{V_{eff}(p-k)}{\left\{k^2\left[1-\Sigma^v(k^2)\right]^2 - k^2\left[m_0+\Sigma^s(k^2)\right]^2\right\}^2} \times \\ & \times \left(\left\{\not{k}\left[1-\Sigma^v(k^2)\right] + m_0 + \Sigma^s(k^2)\right\}\Gamma_0(p)\gamma^5\left\{\not{k}\left[1-\Sigma^v(k^2)\right] + m_0 + \Sigma^s(k^2)\right\} + \right. \\ & \left. + \gamma^5\left\{\not{k}\left[1-\Sigma^v(k^2)\right] + m_0 + \Sigma^s(k^2)\right\}\Gamma_0(p)\gamma^5\left\{\not{k}\left[1-\Sigma^v(k^2)\right] + m_0 + \Sigma^s(k^2)\right\}\gamma^5\right). \end{aligned} \tag{3.45}$$

Passing all the $\gamma^5 s$ to the left we get, for $\Gamma_0(p)$,

$$\Gamma_0(p) = -2i \int \frac{d^4k}{(2\pi)^4} V_{eff}(p-k) \frac{\Gamma_0(k)}{k^2 \left[1-\Sigma^v(k^2)\right]^2 - \left[m_0 + \Sigma^s(k)\right]^2}. \tag{3.46}$$

A comparison of the self-energy, Eq.3.43, and the pion, Eq.3.50, equations shows that, in the case of the zero bare quark mass $m_0 = 0$ the pion equation is ensured of having a solution, namely,

$$\Sigma^s(p) = \Gamma_0(p). \tag{3.47}$$

Chiral symmetry with $\mathscr{O}^\pi$ symmetric under $U(1) \times U(1)$ group

Another possible choice, slightly more complex one, is

$$\sum_i \mathscr{O}_i^\pi \mathscr{O}_i^\pi = \frac{1}{2}\left(1 - \gamma_1^5 \gamma_2^5 - v \gamma_1^\mu \gamma_{2\mu}\right), \tag{3.48}$$

i.e., the sum of scalar, pseudoscalar and vector terms (all isoscalar), wher v is an arbitrary, nonzero, constant. This choice has the advantage of being **flavour independent** so perhaps it would be a more natural choice for fitting the mesonic mass spectrum. The vertex function however is much more difficult:

$$\Gamma(p,\mu) = \Gamma_1(p)\tau\gamma^5 + \Gamma_2(p)\tau\gamma^5 \not{P} + \Gamma_3(p)\tau\gamma^5 \not{p}. \tag{3.49}$$

We will consider here only the case $v = 1$.
In this case, the self-energy and the vertex functions, correspondingly, become:

$$\begin{aligned} \Sigma^s(p) &= -2i \int \frac{d^4k}{(2\pi)^4} V_{eff}(p-k) \frac{m_0 + \Sigma^s(k)}{k^2 \left[1-\Sigma^v(k^2)\right]^2 - \left[m_0 + \Sigma^s(k)\right]^2}, \\ p\Sigma^v(p) &= 2i \int \frac{d^4k}{(2\pi)^4} V_{eff}(p-k) \frac{p.k\left[1-\Sigma^v(k)\right]}{k^2 \left[1-\Sigma^v(k^2)\right]^2 - \left[m_0 + \Sigma^s(k)\right]^2}. \end{aligned} \tag{3.50}$$

and

$$\Gamma_0(p) = -2i \int \frac{d^4k}{(2\pi)^4} \frac{V_{eff}(p-k)\Gamma_0(k)}{D(+)D(-)} \left[\left[k^2 - \frac{P^2}{4}\right] A(+)A(-) - B(+)B(-)\right], \tag{3.51}$$

where

$$\begin{cases} A(\pm) &= 1 - \Sigma_v\left(k \pm \frac{1}{2}P\right), \\ B(\pm) &= m_0 + \Sigma_s\left(k \pm \frac{1}{2}P\right), \\ D(\pm) &= \left(k \pm \frac{1}{2}P\right)^2 A(\pm)^2 - B(\pm)^2. \end{cases} \tag{3.52}$$

Once again, if the pion mass is zero, $\Gamma_0(p)$ reduces identically to the scalar self-energy $\Sigma^s(p)$, reassuring the emergence of a Goldstone boson.

3.2 Numerical techniques and results

In this work we chose to solve both the Dirac and the 1CS equation with a **scalar linear potential**. Our computations were performed in helicity representation for the *s*-wave case. This choice was made in order to reproduce the results of ref.([38]).

Specifically, in Eq.(3.19) we have adopted

$$\mathscr{O} \equiv \mathbf{1} \tag{3.53}$$

and

$$V(p,k) = -8\pi\sigma \left\{ \frac{1}{(p-k)^4} - E_{p_1}\delta^3(p-k) \int \frac{d^3k'}{E_{k_1'}(p-k')^4} \right\}, \tag{3.54}$$

where the insertion of the energy factors is necessary to make the kernel covariant with the restriction of the heavy quark placed on its mass shell. The full 1CS also includes the covariant replacement $(p-k)^2 \to (E_{p_1} - E_{k_1})^2 - (\mathbf{p}-\mathbf{k})^2$, but in the numerical studies in this work we have neglected retardation and use the simplest replacement $(p-k)^2 \to -(\mathbf{p}-\mathbf{k})^2$ as the authors did in ref.([38]). This is usually called the **quasirelativistic approximation**.

3.2.1 Expansion in splines and matrix form for the 1CS and Dirac equations

In order to solve the Dirac equation and the 1CS equation numerically, we wrote it in the **helicity basis** states. This procedure is outlined in Appendix A. Here we just write down the final form of the equations.

Thus, the one-body or Dirac limit equation in this basis is

$$\begin{pmatrix} (E_B - E_{p_2}) & \psi_{1a}(p) \\ (E_B + E_{p_2}) & \psi_{1b}(p) \end{pmatrix} = \int_{\mathbf{k}} \bar{V} \begin{pmatrix} d_1 & d_2 \\ d_3 & d_4 \end{pmatrix} \begin{pmatrix} \psi_{1a}(p) \\ \psi_{1b}(p) \end{pmatrix}, \tag{3.55}$$

where

$$\bar{V} = V(p,k) \frac{N_{p_2} N_{k_2}}{\left(2\sqrt{E_{p_2} E_{k_2}}\right)},$$

$$E_{p_i} = \sqrt{m_i^2 + p_i^2}, \qquad N_{p_i} = (E_{p_i} + m_i)^{1/2}, \tag{3.56}$$

and $V(p,k)$ is given by Eq.3.54.

Also $d_i = a_i + b_i \cos\theta$, with

$$\begin{array}{ll} a_1 = 1, & b_1 = -\tilde{p}_2 \tilde{k}_2, \\ a_2 = \tilde{k}_2, & b_2 = \tilde{p}_2, \\ a_3 = \tilde{p}_2, & b_3 = \tilde{k}_2, \\ a_4 = \tilde{p}_2 \tilde{k}_2, & b_4 = -1, \end{array} \tag{3.57}$$

and $\tilde{p}_j = \dfrac{|\mathbf{p}|}{N_{p_j}^2}$.

And , the 1CS equation in the helicity form is:

$$\begin{pmatrix} (E_B - E_{p_2} - [E_{p_1} - m_1]) & \psi_{1a}(p) \\ (E_B + E_{p_2} - [E_{p_1} - m_1]) & \psi_{1b}(p) \end{pmatrix} = \int_{\mathbf{k}} \bar{V} \begin{pmatrix} D_1 & D_2 \\ D_3 & D_4 \end{pmatrix} \begin{pmatrix} \psi_{1a}(p) \\ \psi_{1b}(p) \end{pmatrix}, \tag{3.58}$$

with $D_i = A_i + B_i \cos\theta$,

$$\begin{array}{rr} A_1 = Q, & B_1 = -R, \\ A_2 = T_2, & B_2 = S_2, \\ A_3 = S_2, & B_3 = T_2, \\ A_4 = R \quad , & B_4 = -Q. \end{array} \tag{3.59}$$

and

$$\begin{array}{ll} Q = 1 + \tilde{p_1}\tilde{p_2}\tilde{k_1}\tilde{k_2}, & R = \tilde{p_1}\tilde{k_1} + \tilde{p_2}\tilde{k_2} \\ S_2 = \tilde{p_2} - \tilde{k_1}\tilde{k_2}\tilde{p_2}, & T_2 = \tilde{k_2} - \tilde{p_1}\tilde{p_2}\tilde{k_2}, \end{array} \tag{3.60}$$

In both equations

$$\int_{\mathbf{k}} = \int \frac{d^3}{(2\pi)^3}. \tag{3.61}$$

It is interesting to notice that equation 3.55 is obtained from equation 3.58 in the limit $m_1 \to \infty$.

For the numerical calculation and to obtain a discrete form of the equation, we applied the method of splines with double integration (SDI) described in Chapter 2. As explained there, in this method one starts by taking explicitly the expansion of the solution into cubic splines. Then one projects the equation into those splines, which is done by multiplying both sides of the equation by a spline of arbitrary order l, $\beta_l(p)$, and by integrating in p

$$\int p^2 \beta_l(p) dp. \tag{3.62}$$

Although this procedure involves a double integral and is more complicated than the method of splines with single integration (SSI), its results are more stable, because overlap integral of the two splines covers the whole region where the solution is defined, as we saw in chapter 2.

With discretization the indexes l, j that correspond respectively to to the spline onto which the projection is made and the summation index of the function expansion, the numerical discrete equations are

$$\left\{ \lambda \begin{pmatrix} A_{lj} & 0 \\ 0 & A_{lj} \end{pmatrix} + \begin{pmatrix} B_{lj}^{11} & 0 \\ 0 & B_{lj}^{22} \end{pmatrix} - \begin{pmatrix} V_{lj}^{11} & V_{lj}^{12} \\ V_{lj}^{21} & B_{lj}^{22} \end{pmatrix} \right\} \begin{pmatrix} \alpha_j^1 \\ \alpha_j^2 \end{pmatrix} = 0. \tag{3.63}$$

Dirac Equation

For the Dirac equation $\lambda = E_B$, i.e. gives the binding energies. And the other matrix elements are defined by

$$A_{lj} = \int_0^\infty p^2 dp \beta_l(p) \beta_j(p), \tag{3.64}$$

$$B_{lj}^{11} = -B_{lj}^{22} = -\int_0^\infty p^2 dp E_p \beta_l(p) \beta_j(p). \tag{3.65}$$

Setting $m_2 = m$ and defining

$$f_l(p) = \frac{N_p}{\sqrt{2E_p}} \beta_l(p), \tag{3.66}$$

we have:

$$\begin{pmatrix} V_{lj}^{11} & V_{lj}^{12} \\ V_{lj}^{21} & B_{lj}^{22} \end{pmatrix} = -\frac{4\sigma}{\pi} \int_0^\infty \int_0^\infty dp dk V_0(p,k) f_l(p) \left\{ f_j(k) \begin{pmatrix} \eta_1 & \eta_2 \\ \eta_3 & \eta_4 \end{pmatrix} - f_j(p) \begin{pmatrix} \eta_1' & \eta_2' \\ \eta_3' & \eta_4' \end{pmatrix} \right\} - \\ -\frac{4\sigma}{\pi} \int_0^\infty \int_0^\infty dp dk V_1(p,k) f_l(p) f_j(k) \begin{pmatrix} \zeta_1 & \zeta_2 \\ \zeta_3 & \zeta_4 \end{pmatrix}. \tag{3.67}$$

The functions η and ζ are

$$\eta_i = a_i + b_i, \qquad \zeta_i = b_i, \tag{3.68}$$

and a_i and b_i are the same of eq. (4). The prime on η' indicates that $\eta_i^{'} = \eta_i(p,p)$, whereas $\eta_i(p,k)$. The functions V_0 and V_1 are given by

$$V_0(p,k) = \frac{1}{2}\int_{-1}^{1} dz \frac{p^2k^2}{(p^2+k^2-2pkz)^2} = \frac{p^2k^2}{(p^2-k^2)^2}, \tag{3.69}$$

$$V_1(p,k) = \frac{1}{2}\int_{-1}^{1} dz \frac{p^2k^2(z-1)}{(p^2+k^2-2pkz)^2} = \frac{1}{2}\frac{pk}{(p+k)^2} - \frac{1}{8}\ln\left(\frac{(p+k)^2}{(p-k)^2}\right). \tag{3.70}$$

1CS Equation

For this equation, $\lambda = \mu = m_1 + E_B$. The $A_{lj}$are the same as in the Dirac case but the B_{lj} are now

$$B_{lj}^{11} = -\int_0^\infty p^2 dp\,(E_{p_1} + E_{p_2})\,\beta_l(p)\beta_j(p), \tag{3.71}$$

$$B_{lj}^{22} = -\int_0^\infty p^2 dp\,(E_{p_1} - E_{p_2})\,\beta_l(p)\beta_j(p). \tag{3.72}$$

The equivalent of $f_l(p)$ is

$$F_l(p) = \frac{N_{p_1}N_{p_2}}{\sqrt{4E_{p_1}E_{p_2}}}\beta_l(p), \tag{3.73}$$

and the potential matrix is written as

$$\begin{aligned}\begin{pmatrix} V_{lj}^{11} & V_{lj}^{12} \\ V_{lj}^{21} & B_{lj}^{22} \end{pmatrix} = &-\frac{4\sigma}{\pi}\int_0^\infty\int_0^\infty dpdk V_0(p,k)F_l(p)\left\{F_j(k)\begin{pmatrix} \bar{\eta}_1 & \bar{\eta}_2 \\ \bar{\eta}_3 & \bar{\eta}_4 \end{pmatrix} - \frac{E_{p_1}}{E_{k_1}}F_j(p)\begin{pmatrix} \bar{\eta}_1^{'} & \bar{\eta}_2^{'} \\ \bar{\eta}_3^{'} & \bar{\eta}_4^{'} \end{pmatrix}\right\} - \\ &-\frac{4\sigma}{\pi}\int_0^\infty\int_0^\infty dpdk V_1(p,k)F_l(p)F_j(k)\begin{pmatrix} \bar{\zeta}_1 & \bar{\zeta}_2 \\ \bar{\zeta}_3 & \bar{\zeta}_4 \end{pmatrix}.\end{aligned} \tag{3.74}$$

with $\bar{\eta}_i = A_i + B_i$ and $\bar{\zeta}_i = B_i$. The meaning of the prime is the same as before and $V_0$and V_1 have the same definitions.

As our potentials are Hermitian, i.e., $V_{ij}(p,k;P) = V_{ji}(k,p;P)$ the matrix arising from the linear potential is symmetric. This last feature is particularly advantageous as it avoided the generation of spurious complex solutions due to round-off errors.

In the next section we will present a discussion on the procedure to evaluate the double integrals, specially because of the singularities arising from the V_0 and V_1 potentials.

Procedure for integration over the singularities

Lets take as example the following double integral:

$$\int_0^\infty\int_0^\infty I(p,k)dpdk = \int_0^\infty\int_0^\infty V_0(p,k)F_1(p)\left(F_1(k)\eta_1(p,k) - F_1(p)\eta_1'(p)\right)dpdk, \qquad l=j=1 \tag{3.75}$$

and plot $I(p,k)$ for a fixed k, for example $k = 0.15$. The plot exhibits the singularity at point p (which moves as a function of k).

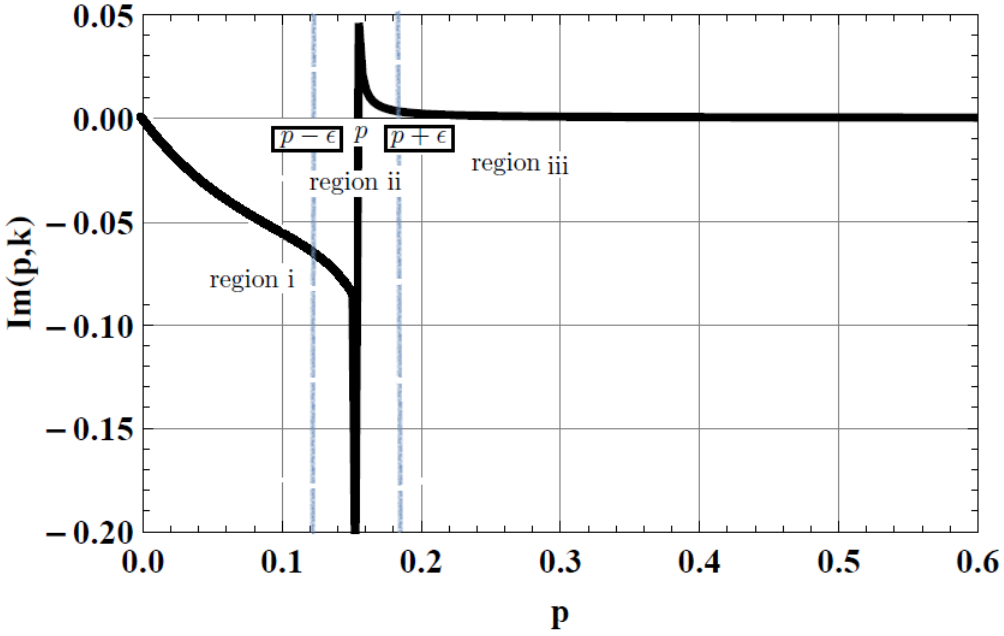

Figure 3.16: Plot $I(p,k)$ for $k = 0.15$.

Our strategy to compute the integral of $I(p,k)$ over p, was to subdivide it in 3 regions as suggested in the figure and, for small ε, to consider the integral in region ii as a Principal Value Integral (we used a symmetric mesh to perform the integration).

Gauss Legendre Quadrature

To compute the integrals numerically we used the Gauss-Legendre Quadrature in which any integral of an arbitrary function f can be calculated through

$$\int_{-1}^{1} f(x)dx \approx \sum_{i=1}^{n} \omega_i f(x_i), \tag{3.76}$$

for very large n, where x_i are the Gaussian points and ω_i the corresponding integration weights [3]. How large the value of n is needed for convergence depends on the behavior of the function.

As the figure suggest we divided the full integral into the integrals in regions I, II and III. Since the Gaussian points, x_i, are defined in the interval $[0,1]$ and $[-1,1]$ we made the following mappings for the different integration regions on the variable p (corresponding to the discrete variable y_i of a numerical mesh of points):

- region I: $x_i^I \in [0,1] \to y_i \in [0, p-\varepsilon[\qquad x_i \to y_i = x_i p;$
- region II: $x_i^{II} \in [-1,1] \to y_i \in [p-\varepsilon, p+\varepsilon[\qquad x_i \to y_i = p + x_i\varepsilon;$
- region III: $x_i^{III} = r_i \in [0,\infty[\to y_i \in [p+\varepsilon,\infty[\qquad x_i \to y_i = (p+\varepsilon)(r_i+1).$

In the last region r_i are defined as $x_i \in [0,1] \to r_i \in [0,\infty[\qquad x_i \to r_i = \tan\left(\frac{\pi x_i}{2}\right)$

Level	In this work	ref.([38])	In this work	ref.([38])
n	$SN = 12$	$SN = 12$	$SN = 20$	$SN = 20$
4	2.11225	2.113	2.10694	2.109
3	1.80699	1.808	1.80727	1.808
2	1.44224	1.443	1.44232	1.443
1	0.93876	0.939	0.93867	0.940
-1	-0.93630	-0.936	-0.93630	-0.936
-2	-1.08500	-1.084	-1.08406	-1.084
-3	-1.17043	-1.170	-1.17296	-1.173
-4	-1.25905	-1.259	-1.23379	-1.233

Table 3.1: Comparison with ref.([38]) results (in GeV) for the 1CS equation with $\sigma = 0.2GeV^2$, $\kappa = 5.0$ and m_2=0.325GeV/c^2.

Level	In this work	ref.([38])	In this work	ref.([38])
κ	$\kappa = 10.0$	$\kappa = 10.0$	$\kappa = 1.0$	$\kappa = 1.0$
n	$SN = 12$	$SN = 12$	$SN = 12$	$SN = 12$
4	2.07724	2.078	1.88090	1.881
3	1.78248	1.783	1.63183	1.632
2	1.43478	1.435	1.29244	1.293
1	0.96313	0.964	0.74397	0.745
-1	-1.09110	-1.009	-0.33407	-0.334
-2	-1.33336	-1.332	-0.34137	-0.341
-3	-1.51631	-1.515	-0.35430	-0.354
-4	-1.64306	-1.642	-0.37916	-0.379

Table 3.2: Comparison with ref.([38]) results (in GeV) for 1CS equation with $\sigma = 0.2GeV^2$ and m_2=0.325GeV/c^2 for $\kappa = 10.0$ and $\kappa = 1.0$.

3.2.2 Results for positive and negative energy states and wavefunctions

In this section we present the results obtained for the 1CS equation with the Splines+Gauss Legendre quadrature method to account for the principal value integration just described. We also solved the Dirac equation with the same method because, to check how numerically the 1CS equation tends to the one-body (Dirac) limit. First of all, on tables 3.3, 3.1 and 3.2 we compare our results for the energy states obtained with those from ref.([38]). For the CST case we show the results two cases of the quark mass ratio ($k = 1$ and $k = 10$). The first conclusion is that our results are in very good agreement with the ones published in the literature, and therefore our numerical method passed this first test. Positive and negative energy eigenvalues for the 2 quark bound state were found, since the two body equations are relativistic.

Besides the eigenvalues, we also calculated the eigenvectors of the Dirac and the 1CS equations. By the definition given in Eq.3.63, the eigenvalue problem for the case of SN number of splines has $2SN$ eigenvalues and eigenvectors. From now on, we will assume the following short-hand notation

Level	In this work	ref.([38])
4	1.94618	1.946
3	1.69508	1.695
2	1.39289	1.393
1	0.97542	0.976
-1	-1.24977	-1.248
-2	-1.57576	-1.574
-3	-1.83980	-1.838
-4	-2.08025	-2.078

Table 3.3: Comparison with ref.([38]) results (in GeV) for the Dirac equation with σ=0.2GeV^2, m_2=0.325GeV/c^2 and $SN = 12$.

for the eigenvectors

$$\left(\begin{array}{c} \left(\begin{array}{c} \alpha_1^1 \\ \alpha_2^1 \\ ... \\ \alpha_{SN}^1 \end{array} \right) \equiv \overrightarrow{\alpha}^+ \\ \left(\begin{array}{c} \alpha_1^2 \\ \alpha_2^2 \\ ... \\ \alpha_{SN}^2 \end{array} \right) \equiv \overrightarrow{\alpha}^- \end{array} \right), \tag{3.77}$$

$$\phi^+(p) = \sum_{j=1}^{SN} \alpha_j^+ \beta_j(p), \tag{3.78}$$

$$\phi^-(p) = \sum_{j=1}^{SN} \alpha_j^- \beta_j(p). \tag{3.79}$$

Since we are dealing with relativistic equations some of the eigenvalues are negative and the upper and lower wavefunction components denoted by ϕ^+ and ϕ^- exist for both positive and negative eigenvalues. In the non-relativistic limit ϕ^- becomes zero as it should - we checked this numerically - since they correspond to the projection of the two-body vertex function into the v-spinor part of the off-shell-quark propagator. We show a series of the Dirac wavefunctions in Figs. 3.17, 3.18, 3.19 and 3.20; and for the 1CS equation in Figs. 3.21, 3.22, 3.23, 3.24, 3.25 and 3.26. We remark that the number of nodes increases with the energy of the state, as it should. For positive-energy states ϕ^+ dominates over ϕ^-, while for negative-energy states ϕ^- dominates over ϕ^+.

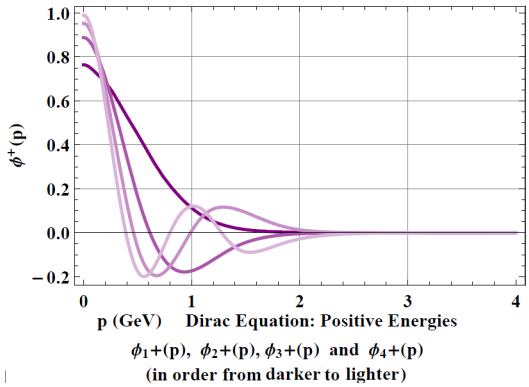

Figure 3.17: Dirac $\phi^+(p)$ wavefunctions for the first positive energies. The parameters used were: $\sigma = 0.2GeV^2$ and $m = 0.325GeV/c^2$.

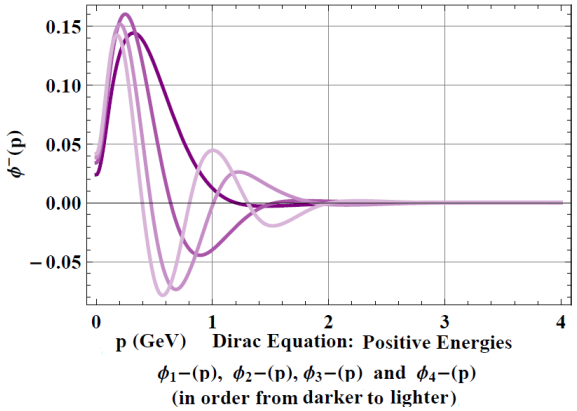

Figure 3.18: Dirac $\phi^-(p)$ wavefunctions for the first positive energies. The parameters used were: $\sigma = 0.2GeV^2$ and $m = 0.325GeV/c^2$.

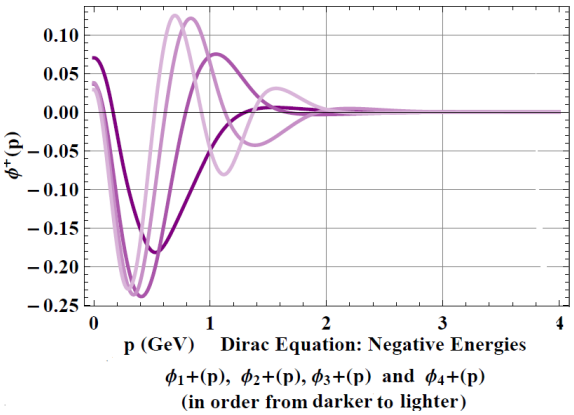

Figure 3.19: Dirac $\phi^+(p)$ wavefunctions for the first negative energies. The parameters used were: $\sigma = 0.2GeV^2$ and $m = 0.325GeV/c^2$.

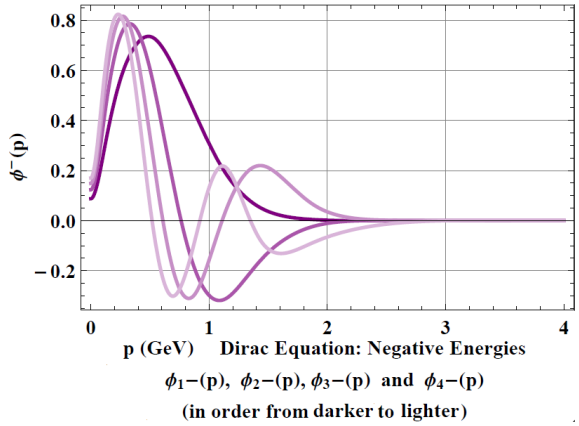

Figure 3.20: Dirac $\phi^-(p)$ wavefunctions for the first negative energies. The parameters used were: $\sigma = 0.2GeV^2$ and $m = 0.325GeV/c^2$.

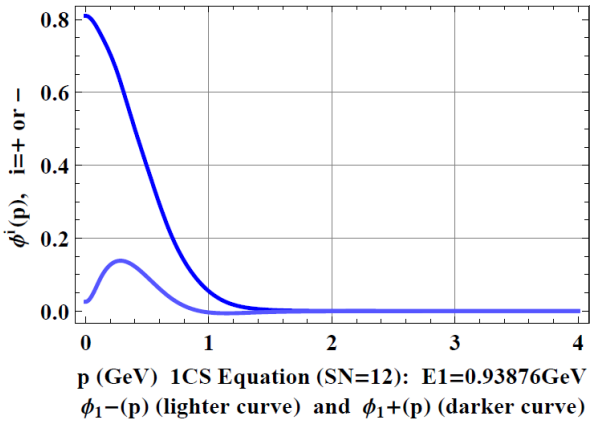

Figure 3.21: 1CS $\phi^+(p)$ and $\phi^-(p)$ wavefunctions for E_1. The parameters used were: $\sigma = 0.2GeV^2$ and $m = 0.325GeV/c^2$.

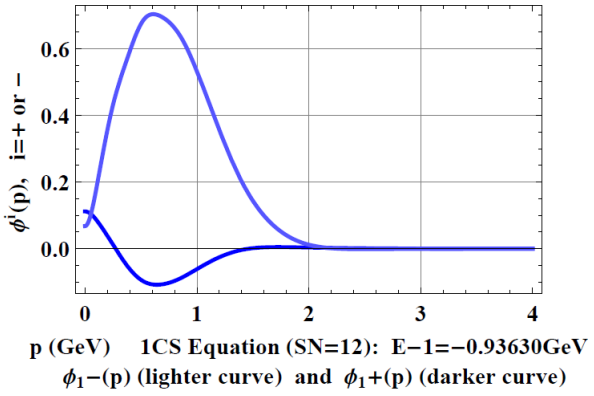

Figure 3.22: 1CS $\phi^+(p)$ and $\phi^-(p)$ wavefunctions for E_{-1}. The parameters used were: $\sigma = 0.2GeV^2$ and $m = 0.325GeV/c^2$.

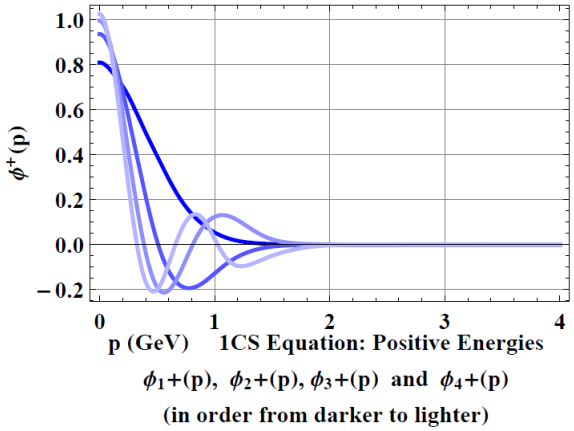

Figure 3.23: 1CS $\phi^+(p)$ wavefunctions for the first positive energies. The parameters used were: $\sigma = 0.2GeV^2$, $\kappa = 5.0$ and $m_2 = 0.325GeV/c^2$.

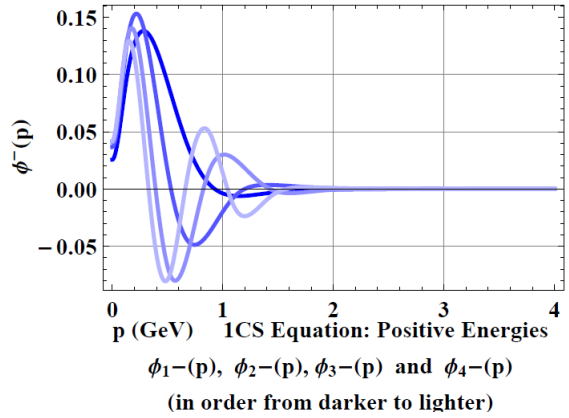

Figure 3.24: 1CS $\phi^-(p)$ wavefunctions for the first positive energies. The parameters used were: $\sigma = 0.2GeV^2$, $\kappa = 5.0$ and $m_2 = 0.325GeV/c^2$.

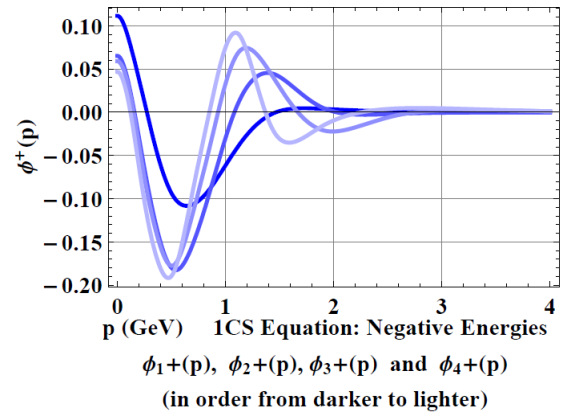

Figure 3.25: 1CS $\phi^+(p)$ wavefunctions for the first negative energies. The parameters used were: $\sigma = 0.2GeV^2$, $\kappa = 5.0$ and $m_2 = 0.325GeV/c^2$.

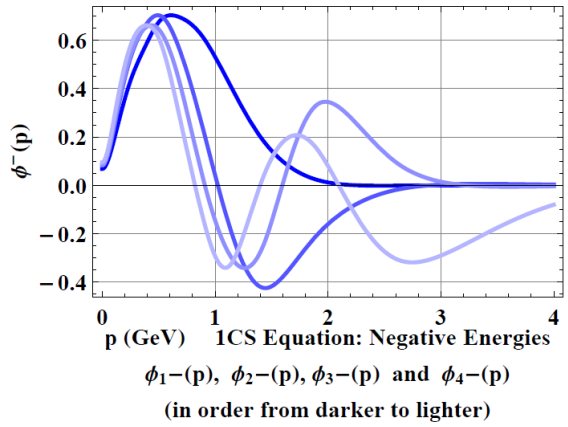

Figure 3.26: 1CS $\phi^-(p)$ wavefunctions for the first negative energies. The parameters used were: $\sigma = 0.2GeV^2$, $\kappa = 5.0$ and $m_2 = 0.325GeV/c^2$.

Convergence of the 1CS results

We analyse here very briefly the convergence of the solutions obtained for the 1CS equation. We decided to check it by fixing the parameters: $\kappa = 5.0$ and $m_2 = 0.325GeV/c^2$ and varying the number of splines. Tables 3.4 and 3.5 show the results obtained and on plot 3.27 we registered the difference between the first eigenvalues computed with $SN = 24$ and $SN = 36$. The higher energy level demand more caution for convergence with the number of splines. For the splines considered, although the results are good, the convergence is not so good as for the *SDI* method for the NRSE in momentum space. The reason is that we have not implemented procedures to remove the singularities from the kernel of equations yet, as we did with the subtraction methods of Chapter 2 for the non-relativistic case.

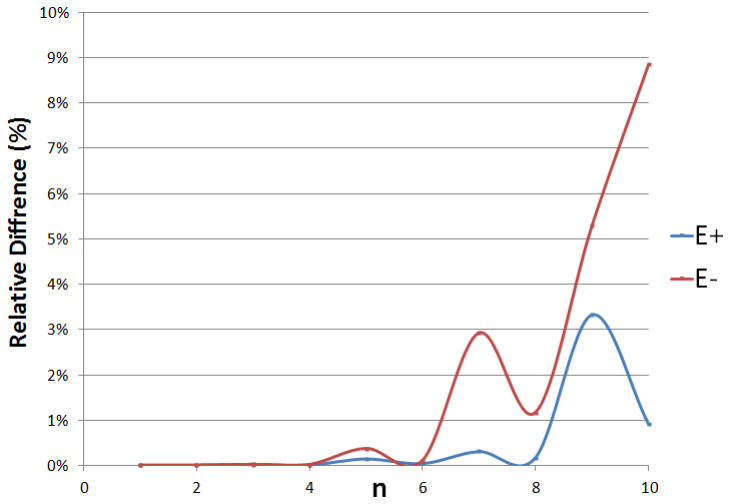

Figure 3.27: Study of convergence for the 1CS equation. This plot represents in the x axis the n principal quantum number of the state and in the y axis the relative differences in % between the binding energies computed with $SN = 24$ and $SN = 36$. The curve in blue refers to the positive energies and in red to the negative.

Level E_n	$SN = 8$	$SN = 12$	$SN = 16$	$SN = 20$	$SN = 24$	$SN = 36$
36						38.1145942
35						20.0729985
34						16.7049198
33						15.7648817
32						14.0993175
31						11.6024919
30						11.1861743
29						10.8555549
28						10.5152114
27						9.2870255
26						8.3836147
25						8.0995645
24					25.2693254	7.0438661
23					10.8251524	6.6618381
22					10.5596630	6.0637717
21					8.5755602	5.5317100
20				20.9942414	7.2630647	5.2993690
19				8.8753511	7.1243854	5.1998769
18				8.8342537	6.3447416	4.6593971
17				6.9751274	5.5583593	4.6337476
16			16.7265183	5.8505350	5.2649128	4.2729295
15			7.0968303	5.7870880	4.8803692	4.0893409
14			6.9370091	4.9754331	4.4227815	3.7161481
13			5.4891908	4.3189851	4.1578734	3.6671803
12		12.4732195	4.5207315	4.2570958	3.9098239	3.3210493
11		5.3248963	4.4695719	3.7562447	3.5065532	3.2281931
10		5.0217462	3.7413943	3.3970389	3.4285409	2.9741776
9		3.9343332	3.3063672	3.2967678	3.1907196	2.8140910
8	8.2560359	3.2216499	3.1435465	3.0042649	3.0095363	2.5918884
7	3.5754572	3.1146194	2.7968488	2.8216146	2.8129097	2.3669719
6	3.1696573	2.6128892	2.6135514	2.5995324	2.6007084	2.1071024
5	2.5348226	2.3903388	2.3676555	2.3707630	2.3672803	1.8721491
4	2.1103270	2.1122511	2.1071361	2.1069555	2.1066746	1.8075597
3	1.8263340	1.8069905	1.8071113	1.8073761	1.8078660	1.4419878
2	1.4419153	1.4422402	1.4421523	1.4420646	1.4418909	1.0370765
1	0.9387625	0.9387569	0.9387657	0.9387507	0.9386402	0.9387535

Table 3.4: Accuracy of our method for solving the 1CS Equation. Positive Eigenergies up to $SN = 36$.

Level E_n	$SN = 8$	$SN = 12$	$SN = 16$	$SN = 20$	$SN = 24$	$SN = 36$
-1	-0.9361628	-0.9362966	-0.9362966	-0.9363082	-0.9362978	-0.6716749
-2	-1.0929114	-1.0850072	-1.0841616	-1.0840662	-1.0840613	-0.8997735
-3	-1.1711214	-1.1704344	-1.1731693	-1.1729599	-1.1727269	-0.9363099
-4	-1.3456090	-1.2590466	-1.2381929	-1.2337902	-1.2335810	-1.0840120
-5	-1.4454967	-1.3127071	-1.2922883	-1.2830259	-1.2782671	-1.1735096
-6	-1.9850379	-1.4270717	-1.3388811	-1.3095924	-1.3082196	-1.2338045
-7	-2.8269357	-1.6001257	-1.4708601	-1.3881263	-1.3486912	-1.2776596
-8	-5.0103426	-2.0292152	-1.4822570	-1.4343209	-1.4177746	-1.3118599
-9		-2.6001656	-1.7627270	-1.5002432	-1.4247932	-1.3420469
-10		-3.3416160	-2.1327396	-1.6544335	-1.5198316	-1.3732911
-11		-4.4089398	-2.6081641	-1.9491895	-1.6081976	-1.3877307
-12		-7.3509439	-3.2077240	-2.3060457	-1.8451127	-1.4318024
-13			-3.9458226	-2.7314994	-2.1141866	-1.4818083
-14			-4.8561189	-3.2231635	-2.4543694	-1.4876623
-15			-6.0508905	-3.7854028	-2.8720972	-1.5536191
-16			-9.6752572	-4.4705401	-3.3587185	-1.6358861
-17				-5.2258807	-3.8794290	-1.8489583
-18				-6.3161068	-4.3838287	-2.0188938
-19				-7.6211149	-5.0089355	-2.2835073
-20				-11.9743115	-5.7791542	-2.6880544
-21					-6.6971410	-3.1681939
-22					-7.7429823	-3.5557290
-23					-9.2999136	-3.7286811
-24					-14.2693220	-4.1158862
-25						-4.6659391
-26						-5.4889149
-27						-6.4233767
-28						-7.4506469
-29						-8.6049824
-30						-9.8674012
-31						-10.2825782
-32						-10.9049592
-33						-12.5008710
-34						-14.7813571
-35						-19.9230530
-36						-21.1316267

Table 3.5: Accuracy of our method for solving the 1CS Equation. Negative energies up to $SN = 36$.

E_n	$\kappa = 1.0$	$\kappa = 5.0$	$\kappa = 10$	$\kappa = 50$	$\kappa = 100$	$\kappa = 1000$	Dirac
E_4	1.88090	2.11225	2.07724	1.98091	1.96405	1.94787	1.94396
E_3	1.63183	1.80699	1.78248	1.72044	1.70839	1.69657	1.69493
E_2	1.29244	1.44224	1.43478	1.40555	1.39956	1.39364	1.39375
E_1	0.74397	0.93876	0.96313	0.97463	0.97516	0.97543	0.97554
E_{-1}	-0.33407	-0.93630	-1.09110	-1.21929	-1.23466	-1.24828	-1.24894
E_{-2}	-0.34137	-1.08501	-1.33336	-1.53120	-1.55378	-1.57353	-1.57651
E_{-3}	-0.35430	-1.17043	-1.51631	-1.78123	-1.81106	-1.83700	-1.83933
E_{-4}	-0.37916	-1.25905	-1.64306	-2.01380	-2.04839	-2.07741	-2.06676

Table 3.6: Dirac limit of the 1CS equation. The light quark mass is varied in the CST equation. Comparison of the 1CS results for 6 increasing mass ratios with the Dirac results (last column).For these computations m_2 was fixed with $m_2 = 0.325 GeV/c^2$. The number of splines used were $SN = 12$.

1CS One-body (Dirac) Limit

In table 3.6 we show the results of the CST for the excited states as one increases the mass ratio $\kappa = m_1/m_2$. The values, just as expected, tend to the one-body limit Dirac results, for both positive and negative energies. This is illustrated in Figs. 3.28 and 3.29.

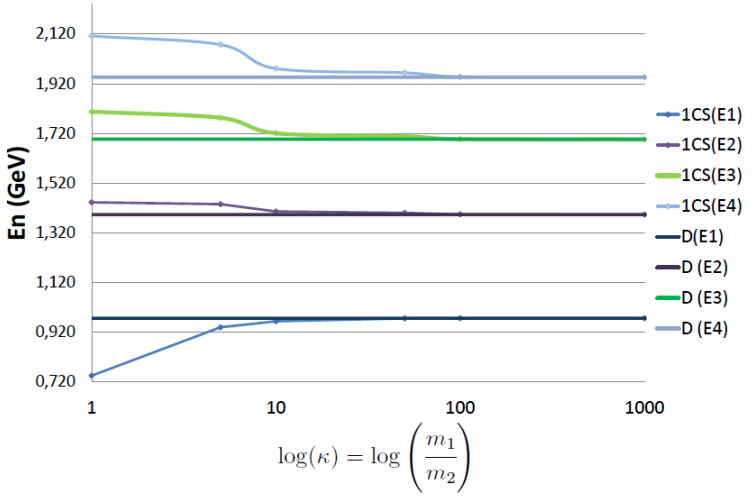

Figure 3.28: Dirac limit of the 1CS Equation for the positive states. The heavy quark mass is varied in the CST equation. Comparison of the 1CS with the Dirac results as a function of the quark mass ratio.

Non-relativistic reduction of the 1CS and Dirac equations

Dirac case Another interesting limit to be investigated is when the particle's mass in the Dirac equation increases. We did that and compared it with the NRSE equation results obtained in Chapter 2 through the same SDI Method, for matching parameters. The results are given on tables 3.7 and 3.8 and in Fig.3.30, where the relative difference between the predicted masses in one and the other methods are plotted in terms of the $log(m)$. There is one important note in the study of this limit: the values which are being compared are the predicted masses corresponding to the positive solutions of the Dirac equation. The negative eigenvalues still appear in our numerical solutions, but the corresponding eigenvectors tend to zero, as expected. Fig.3.31 illustrates precisely this.

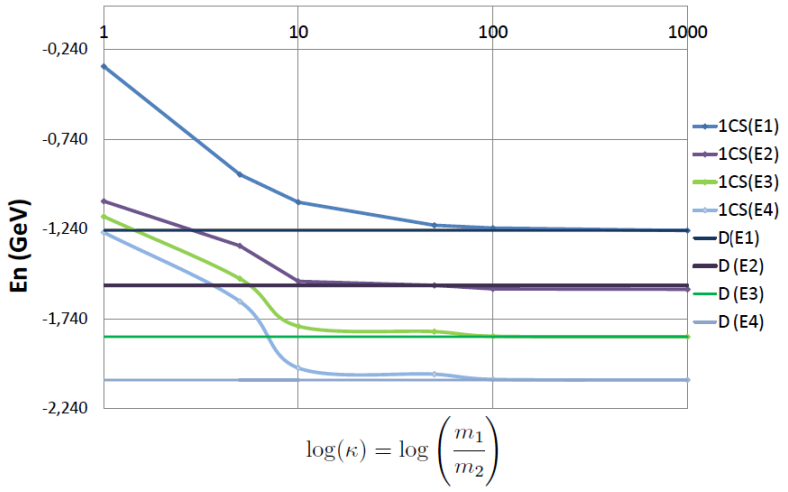

Figure 3.29: The same as Fig. 3.28 but for the negative states.

	SDI	$m_R = 4.65$	$m_R = 10$	$m_R = 20$	$m_R = 100$	$m_R = 1000$
1	2.338108	9.779071	20.37115	40.29458	200.17227	2000.36596
2	4.087949	10.13761	20.64892	40.51505	200.30120	2000.40182
3	5.520560	10.43115	20.87633	40.69555	200.40676	2000.43117
4	6.786708	10.69058	21.07732	40.85507	200.50005	2000.45711

Table 3.7: Meson masses (in GeV/c^2) according to the NRSE: SDI $SN = 64$.

	$m = 4.65$	$m = 10$	$m = 20$	$m = 100$	$m = 1000$
1	10.27543	20.58412	40.46599	200.28892	2000.14181
2	10.69364	21.02098	40.81371	200.56634	2000.31190
3	10.99657	21.37684	41.12727	200.81554	2000.58749
4	11.24787	21.69625	41.53684	201.03196	2000.96253

Table 3.8: Meson masses (in GeV/c^2) according to the Dirac equation for increasing m. Parameters: $\sigma = 0.2 GeV^2$ and $SN = 12$.

	$m_2 = 4.65$	$m_2 = 10$	$m_2 = 20$	$m_2 = 100$	$m_2 = 1000$
1	9.38050	20.58430	40.46615	200.28900	2000.14185
2	9.41501	21.02132	40.81397	200.56646	2000.31192
3	9.44001	21.37737	41.12751	200.81595	2000.58750
4	9.46075	21.69668	41.53699	201.03214	2000.96253

Table 3.9: Meson masses (in GeV/c^2) according to the 1CS equation or increasing m_2 and with fixed $\kappa = 1000$. Parameters: $\sigma = 0.2 GeV^2$ and $SN = 12$.

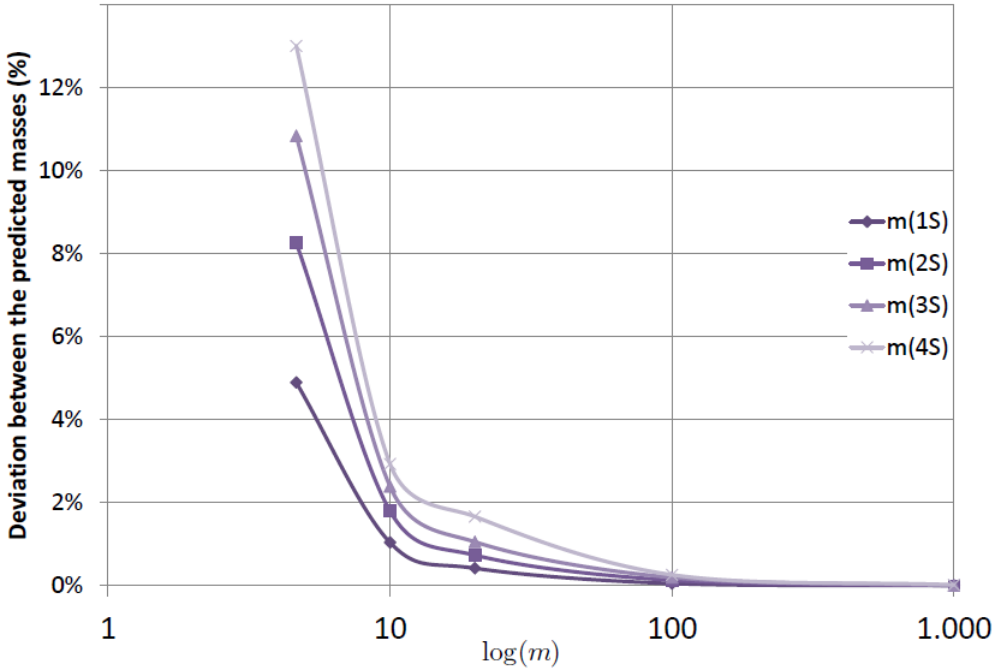

Figure 3.30: Non-relativistic reduction of the Dirac Equation. Relative deviations between the Dirac and the Schrödinger equation as a function of the "light" mass for several states.

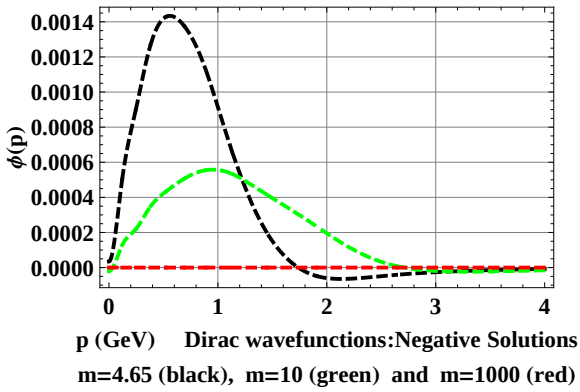

Figure 3.31: Dirac wave functions for negative energy states with increasing mass values.

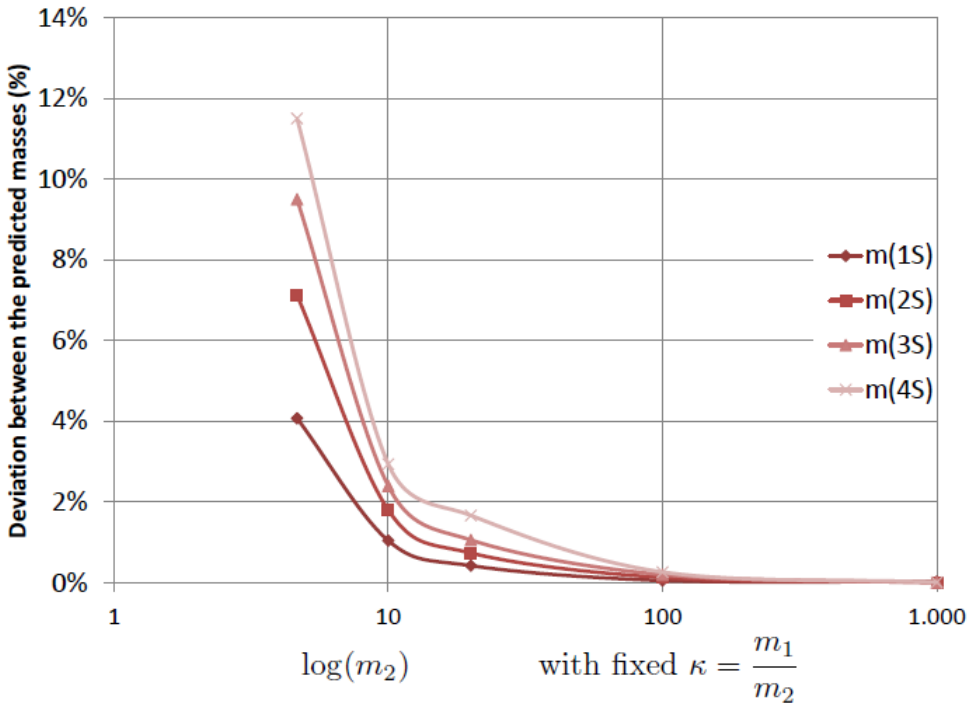

Figure 3.32: Non-relativistic reduction of the 1CS Equation. Relative deviations between the 1CS and the Schrödinger equation as a function of the mass for several states

1CS case Since we have already shown the one-body (Dirac) reduction of the 1CS equation, to show the non-relativistic limit we only have to increase in the last one the second quark mass. The final results are explicitly shown on table 3.9 and fig.3.32.

Chapter 4

Conclusions and Outlook

This work is the first phase of a phenomenological study of mesons within a relativistic framework, the CST, where the dynamical equation is a quasi-potential equation in momentum space, that is to say, a three-dimensional reduction of the Bethe-Salpeter equation. Quark confinement is obtained by using a linear quark-antiquark potential, whose momentum-space representation is somewhat subtle, but leads to a rather elegant final equation. Although the fundamental theory QCD is used only to suggest the form of the confining interaction between quarks, the formalism also satisfies another very important feature of hadronic structure: chiral symmetry breaking.

The CST has already been applied to the study of mesons in the past, however, so far the constituent quark mass has been treated as a constant (ref.[3, 8, 9]), or as a phenomenological function not related to the kernel (ref.[10]), and therefore these model calculations are not entirely satisfactory. A consistent implementation of the dynamical breaking of chiral symmetry requires that the dressed quark mass is calculated from the self-interaction of the bare quark through the same confining interaction that acts between the different quarks in a meson. For the special case of the pion, it was shown analytically that, in the chiral limit of vanishing bare quark mass, the two-body CST equation yields a massless pion solution, while the quarks acquire a non-zero dressed mass through dynamical chiral symmetry breaking.

A first step in the implementation of this program was performed in a very recent paper (ref.[39]), where the quark self-energy in CST was studied for a simple toy model. The next step will be the calculation of the quark self-energy with more realistic interaction models that will then be used to calculate the meson spectrum and the meson wave functions. Moreover, we expect that by connecting the dressed quark mass and the confining interaction we obtain additional useful constraints on the parameters of the interaction model that do not emerge automatically from fits to the spectroscopic data.

A very important part of this program is the development of reliable numerical techniques to solve the CST equations, which have the form of integral equations with a singular kernel in momentum space. The best way to test numerical methods is to apply them to problems where an exact solution is known. For the CST equations no analytic solutions have been found so far, but the numerical solution of integral equations with similar singularities can also be studied with the non-relativistic Schrödinger equation in its momentum-space form. Apart from serving as test problems, the results can also be interesting by themselves, because for heavy-quark systems the non-relativistic description is known to be a good approximation, and a comparison with experimental data becomes meaningful.

In this work, we started with a series of tests of numerical algorithms by solving the non-relativistic differential Schrödinger equation for a linear confining interaction in coordinate space. For *s*-waves the exact solutions are known analytically, which allows us to estimate the quality of our numerical solutions. The same algorithm is then applied to obtain solutions for higher partial waves, for which no analytic solutions exist, and which can then be used as benchmark values for our numerical solutions of the corresponding integral equation in momentum space.

We proceeded with the solution of the Schrödinger equation in momentum space for the same linear potential. Since its direct Fourier transform does not exist, the linear potential has been used in previous work mostly in a modified, screened form, which introduces a dependence on a screening parameter. An unscreened formulation has been achieved as well in the context of CST calculations. However, in all cases the resulting equations contain a singular kernel. The singularity is of principal-value type and can be integrated, but it requires special treatment and complicates the numerical solution considerably.

The main new contribution of this work is the reformulation of the Schrödinger equation with an unscreened linear potential in momentum space into a form where all singularities are eliminated from the kernel. The numerical solution of this equation requires less effort and computing time than the singular versions. For this purpose we used two different techniques, called SSI and SDI, based on the expansion of the wave function in a basis of B-splines, and compared the results to the corresponding values already obtained in coordinate space. SSI requires single integrations over the kernel multiplied with spline functions, whereas SDI demands the evaluation of double integrals. SSI is much faster than SDI, but for the same number of spline basis functions its results are less accurate then the ones of SDI, which in turn shows a very impressive rate of convergence and overall stability. For some cases with higher partial waves, SSI did not reach a converged result. However, there are ways to improve SSI which we did not yet have time to explore.

We are confident that the method that eliminated the singularities from the nonrelativistic kernel can also be used to do the same in the relativistic kernel of the CST equation. This task is planned for the near future. In this work, we decided to revisit first the work of ref.[38] where the relativistic quark-antiquark bound-state problem was solved in a somewhat simplified form (retardation was neglected) with the Dirac and 1CS equations. We obtained very good agreement of our results for the bound-state energies, which in the relativistic case are both positive and negative, with the results reported in ref.[38].

In addition to these tests that confirm the validity of our numerical methods, we checked whether the solutions of the 1CS and Dirac equations behave as expected in certain limits. First, in the limit of one mass tending to infinity, the 1CS results should become equal to the Dirac results. This is called the one-body limit, and by fixing one quark mass and making the other one heavier and heavier, i.e. by increasing the mass ratio, we see that the bound-state energies indeed converge towards the Dirac energies. In fact, the 1CS equation works particularly well for the description of heavy-light quark systems, where it is expected to be a very good approximation for the more general two-channel CST equation.

Second, in the limit of all quark masses becoming very large, both relativistic equations should approach the same nonrelativistic limit, namely the Schrödinger equation. Again, we find that the numerically obtained energies of the Dirac and 1CS equations indeed tend towards the Schrödinger energies when the quark masses are increased. It also confirms that our relativistic generalization of the linear potential behaves correctly in the nonrelativistic limit.

We believe that this work will enable us to increase the efficiency of computer codes required to solve more realistic models involving a linear confining interaction within the CST framework in the near future. We are particularly interested in the light quark systems, where relativistic effects are large, and where a two-channel CST equation (2CS) has to be applied. Once a parametrization of the interaction model is found that provides a good description of the meson spectrum, the corresponding meson wave functions can be used to calculate many interesting properties of the mesons themselves or of reactions in which they participate.

Appendix A

1CS and Dirac equations in Helicity Representation

In this Appendix we present the steps followed to get the helicity form of the Dirac and 1CS equations.

We start by rewriting Eq.3.19 here for convenience:

$$\Psi(p,\lambda)\,(m_2 - \not{p}_2) = -\int \frac{d^3k}{(2\pi)^3}\frac{V(p,k)}{\sqrt{4E_{p1}E_{k1}}}\sum_{\lambda'}\bar{u}\,(\mathbf{p},\lambda)\,\mathscr{O}u\left(\mathbf{p},\lambda'\right)\Psi(k,\lambda')\mathscr{O}. \tag{A.1}$$

We can now expand the wavefunction and the projection operator in terms of the helicity spinors (tableA.1) given by

$$u^{+}\,(\mathbf{p},\lambda_j) \equiv u\,(\mathbf{p},\lambda_j) = N_{p_j}\begin{pmatrix} 1 \\ 2\lambda\tilde{p}_j \end{pmatrix}\chi^{\lambda_j}, \tag{A.2}$$

and

$$u^{-}\,(\mathbf{p},\lambda_j) \equiv v\,(-\mathbf{p},\lambda_j) = N_{p_j}\begin{pmatrix} -2\lambda\tilde{p}_j \\ 1 \end{pmatrix}\chi^{\lambda_j}, \tag{A.3}$$

with

$$N_{p_j} = (E_p + m)^{1/2}, \qquad \tilde{p}_j = \frac{|\mathbf{p}|}{N_{p_j}^2}. \tag{A.4}$$

The wavefunction can be expanded using the decomposition of the propagator into ρ spin contributions (ref.[35]):

$$\frac{(m_2 + \not{k}_2)}{m_2^2 - k_2^2} = \frac{1}{2E_k}\sum_{\lambda_2}\left[\frac{u\,(\mathbf{k},\lambda_2)\,\bar{u}\,(\mathbf{k},\lambda_2)}{E_{k_2} - k_{20} - i\varepsilon} - \frac{v\,(-\mathbf{k},\lambda_2)\,\bar{v}\,(-\mathbf{k},\lambda_2)}{E_{k_2} + k_{20} - i\varepsilon}\right]. \tag{A.5}$$

External quarks		Internal quarks	
$\lambda_i = \frac{1}{2};$	$\begin{pmatrix} 1 \\ 0 \end{pmatrix}$	$\lambda_i^{'} = \frac{1}{2};$	$\begin{pmatrix} \cos(\theta/2) \\ \sin(\theta/2) \end{pmatrix}$
$\lambda_i = -\frac{1}{2};$	$\begin{pmatrix} 1 \\ 0 \end{pmatrix}$	$\lambda_i^{'} = -\frac{1}{2};$	$\begin{pmatrix} -\sin(\theta/2) \\ \cos(\theta/2) \end{pmatrix}$

Table A.1: Helicity spinors.

Using this in

$$\Psi(k,\lambda) = \frac{1}{\sqrt{2E_{k1}}}\bar{u}(\mathbf{k},\lambda)\Gamma(k)\frac{m_2 + \not{k}_2}{m_2^2 - k_2^2}, \tag{A.6}$$

it can be shown that the wavefunction has the following form

$$\Psi(p,\lambda) = \sum_{\rho\lambda_2} \Psi^{\rho}_{\lambda\lambda_2} \bar{u^{\rho}}(\mathbf{p},\lambda_2). \tag{A.7}$$

Furthermore, the most general form of the pseudoscalar vertex function with particle 1 on shell is

$$\bar{u^{+}}(\mathbf{p},\lambda)\Gamma(p) = \bar{u^{+}}(\mathbf{p},\lambda)\left\{\Gamma_1\gamma^5 + \Gamma_1\gamma^5(m_2 - \not{p}_2)\right\} \tag{A.8}$$

and these Dirac operators are built only from the 2×2 matrices $\mathbf{1}$ and $\sigma.\mathbf{p} = 2\lambda p$. Therefore in helicity space the helicity is conserved and an explicit calculation shows that

$$\bar{u^{+}}(\mathbf{p},\lambda)\Gamma(p)u^{\rho}(\mathbf{p},\lambda_2) = \delta_{\lambda\lambda_2}(2\lambda)^{\delta_{+p}}\Gamma^{\rho}(p), \tag{A.9}$$

where $\Gamma^{\rho}(p)$ are independent of the helicity. Hence Eq.A.7 can be writen as

$$\sqrt{2E_{p_2}}\Psi(p,\lambda) = \frac{1}{\sqrt{4E_{p_2}E_{p_1}}}\left\{\psi_{1a}(p)\bar{u^{-}}(\mathbf{p},\lambda) + 2\lambda\,\psi_{1b}(p)\bar{u^{+}}(\mathbf{p},\lambda)\right\}, \tag{A.10}$$

where

$$\psi_{1a} = -\frac{\Gamma^{-}}{E_{k_2} + E_{k_1} - \mu}, \qquad \psi_{1b} = \frac{\Gamma^{+}}{E_{k_2} - E_{k_1} + \mu}. \tag{A.11}$$

Bringing all of these elements together gives the helicity form of the single channel spectator equation

$$\begin{pmatrix} (E_B - E_{p_2} - [E_{p_1} - m_1]) & \psi_{1a}(p) \\ (E_B + E_{p_2} - [E_{p_1} - m_1]) & \psi_{1b}(p) \end{pmatrix} = \int_{\mathbf{k}} \bar{V} \begin{pmatrix} D_1 & D_2 \\ D_3 & D_4 \end{pmatrix} \begin{pmatrix} \psi_{1a}(p) \\ \psi_{1b}(p) \end{pmatrix}, \tag{A.12}$$

with,

$$\begin{array}{ll} A_1 = Q, & B_1 = -R, \\ A_2 = T_2, & B_2 = S_2, \\ A_3 = S_2, & B_3 = T_2, \\ A_4 = R. & B_4 = -Q. \end{array} \tag{A.13}$$

and

$$\begin{array}{ll} Q = 1 + \tilde{p_1}\tilde{p_2}\tilde{k_1}\tilde{k_2}, & R = \tilde{p_1}\tilde{k_1} + \tilde{p_2}\tilde{k_2} \\ S_2 = \tilde{p_2} - \tilde{k_1}\tilde{k_2}\tilde{p_2}, & T_2 = \tilde{k_2} - \tilde{p_1}\tilde{p_2}\tilde{k_2}. \end{array} \tag{A.14}$$

The Dirac equation, Eq.3.55,

$$\begin{pmatrix} (E_B - E_{p_2}) & \psi_{1a}(p) \\ (E_B + E_{p_2}) & \psi_{1b}(p) \end{pmatrix} = \int_{\mathbf{k}} \bar{V} \begin{pmatrix} d_1 & d_2 \\ d_3 & d_4 \end{pmatrix} \begin{pmatrix} \psi_{1a}(p) \\ \psi_{1b}(p) \end{pmatrix}, \tag{A.15}$$

and $d_i = a_i + b_i\cos\theta$, with

$$\begin{array}{ll} a_1 = 1, & b_1 = -\tilde{p_2}\tilde{k_2}, \\ a_2 = \tilde{k_2}, & b_2 = \tilde{p_2}, \\ a_3 = \tilde{p_2}, & b_3 = \tilde{k_2}, \\ a_4 = \tilde{p_2}\tilde{k_2}, & b_4 = -1. \end{array} \tag{A.16}$$

is obtained from equation 3.58 in the limit $m_1 \to \infty$.

Appendix B

Results of the NRSE in p-space

In this appendix we present the results for the binding energies and some wavefunctions obtained as a solution of the NRSE in momentum space. The complete discussion is on Chapter 2 of this thesis.

For all the plots in the figures we have adopted the convention that the wavefuntions are organized from darker to lighter in color, according to increasing n.

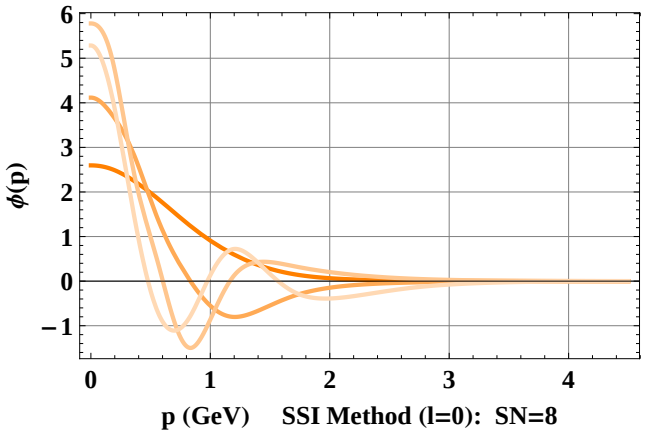

Figure B.1: SSI method: wavefunctions of s-state for the first 4 excited states: $\phi_1(p)$, $\phi_2(p)$, $\phi_3(p)$ and $\phi_4(p)$. The wavefunctions are normalized and computed for SN=8.

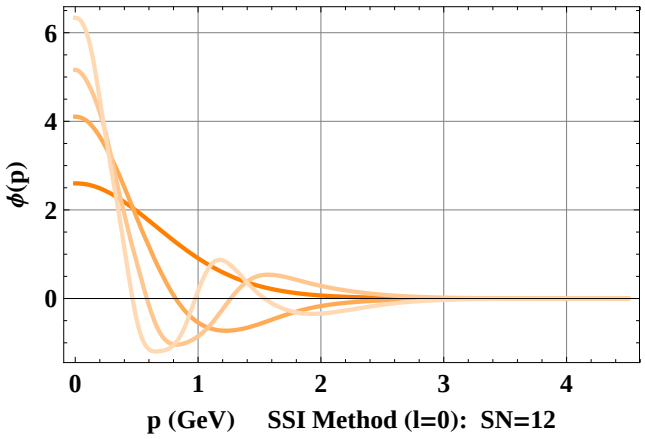

Figure B.2: SSI method: wavefunctions of s-state for the first 4 excited states: $\phi_1(p)$, $\phi_2(p)$, $\phi_3(p)$ and $\phi_4(p)$. The wavefunctions are normalized and computed for SN=12.

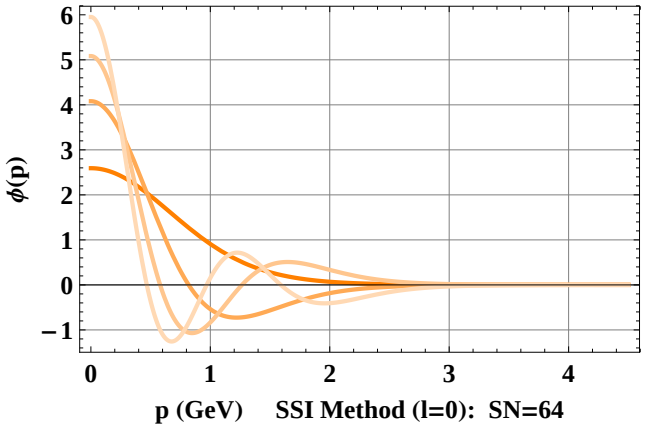

Figure B.3: SSI method: wavefunctions of s-state for the first 4 excited states: $\phi_1(p)$, $\phi_2(p)$, $\phi_3(p)$ and $\phi_4(p)$. The wavefunctions are normalized and computed for SN=64.

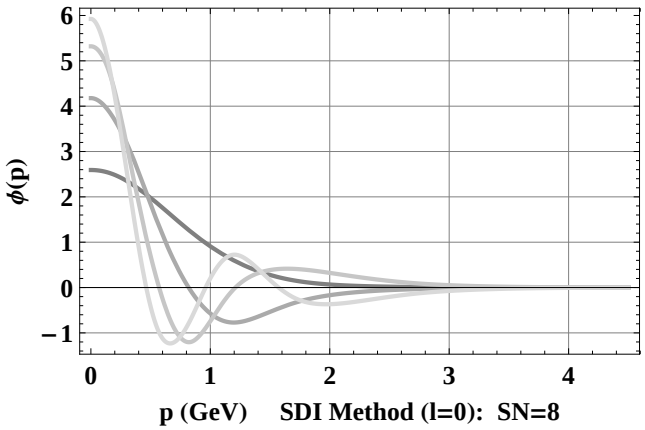

Figure B.4: SDI method: wavefunctions of s-state for the first 4 excited states: $\phi_1(p)$, $\phi_2(p)$, $\phi_3(p)$ and $\phi_4(p)$. The wavefunctions are normalized and computed for SN=8.

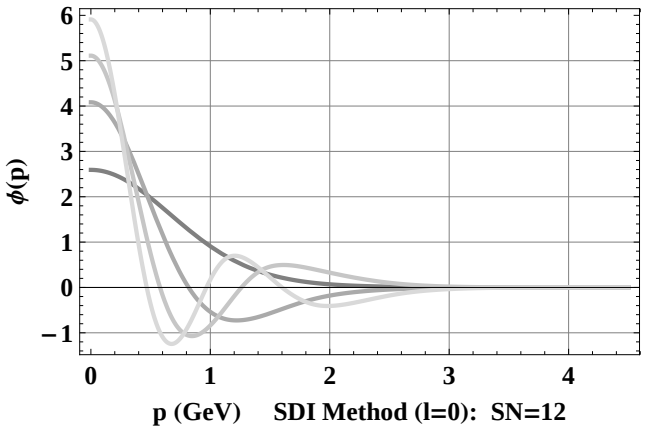

Figure B.5: SDI method: wavefunctions of s-state for the first 4 excited states: $\phi_1(p)$, $\phi_2(p)$, $\phi_3(p)$ and $\phi_4(p)$. The wavefunctions are normalized and computed for SN=12.

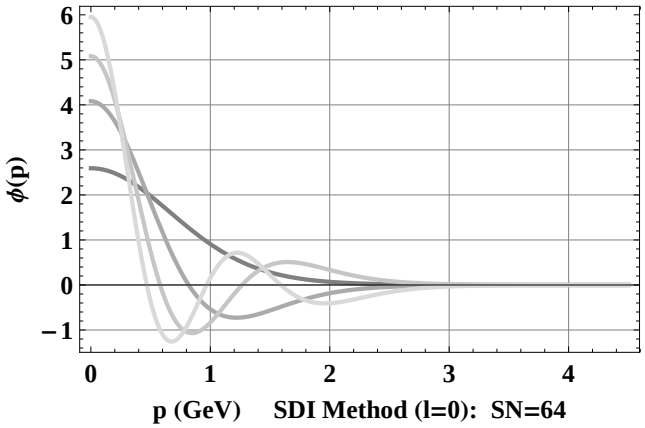

Figure B.6: SDI method: wavefunctions of s-state for the first 4 excited states: $\phi_1(p)$, $\phi_2(p)$, $\phi_3(p)$ and $\phi_4(p)$. The wavefunctions are normalized and computed for SN=64.

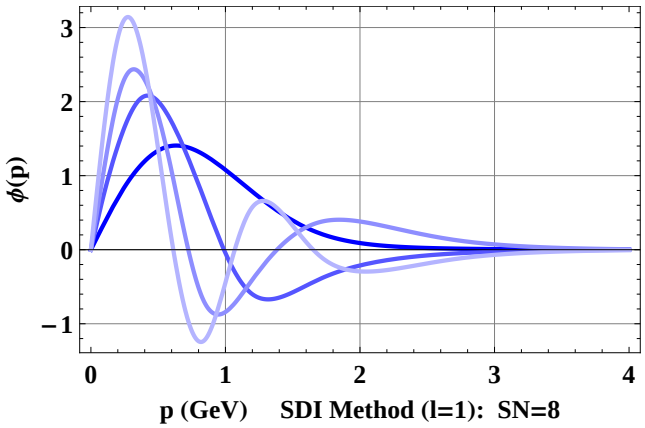

Figure B.7: SDI method: wavefunctions of p-state for the first 4 excited states: $\phi_1(p)$, $\phi_2(p)$, $\phi_3(p)$ and $\phi_4(p)$. The wavefunctions are normalized and computed for SN=8.

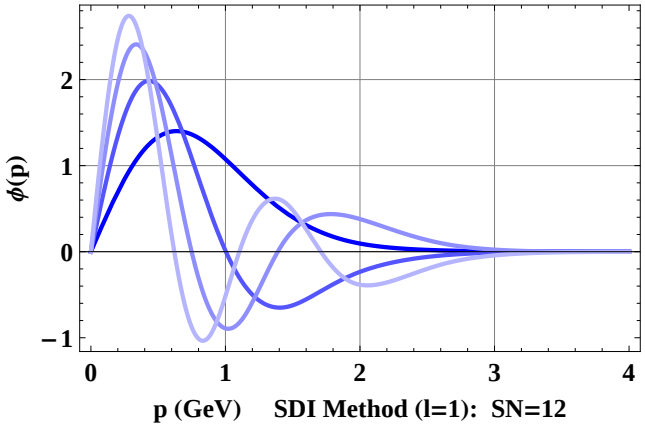

Figure B.8: SDI method: wavefunctions of p-state for the first 4 excited states: $\phi_1(p)$, $\phi_2(p)$, $\phi_3(p)$ and $\phi_4(p)$. The wavefunctions are normalized and computed for SN=12.

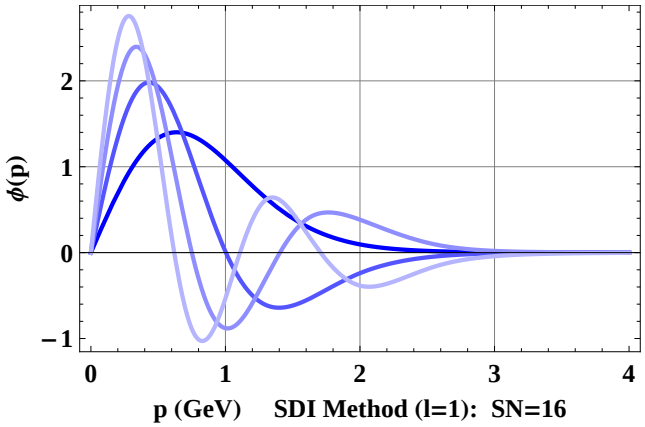

Figure B.9: SDI method: wavefunctions of p-state for the first 4 excited states: $\phi_1(p)$, $\phi_2(p)$, $\phi_3(p)$ and $\phi_4(p)$. The wavefunctions are normalized and computed for SN=16.

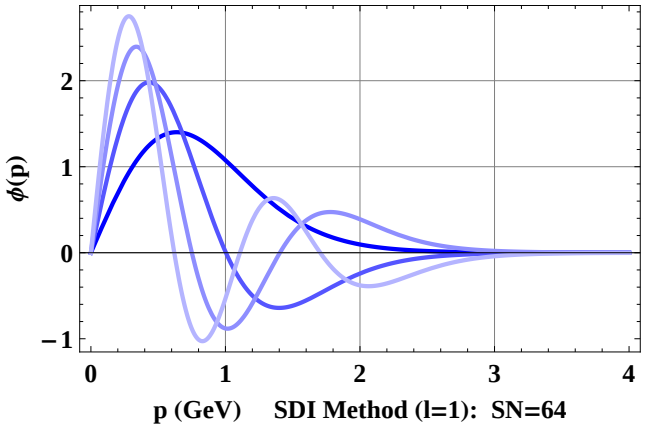

Figure B.10: SDI method: wavefunctions of p-state for the first 4 excited states: $\phi_1(p)$, $\phi_2(p)$, $\phi_3(p)$ and $\phi_4(p)$. The wavefunctions are normalized and computed for SN=64.

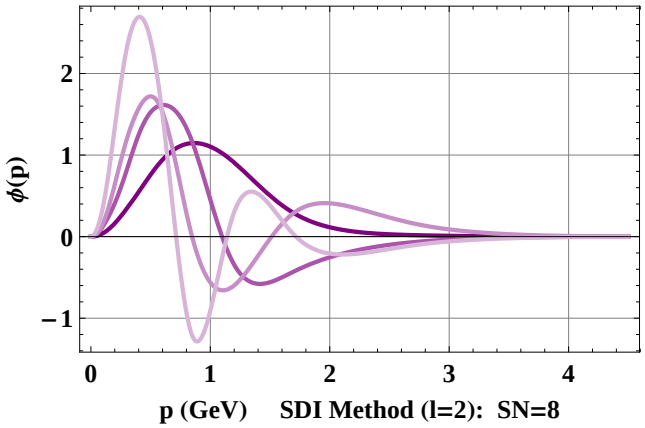

Figure B.11: SDI method: wavefunctions of d-state for the first 4 excited states: $\phi_1(p)$, $\phi_2(p)$, $\phi_3(p)$ and $\phi_4(p)$. The wavefunctions are normalized and computed for SN=8.

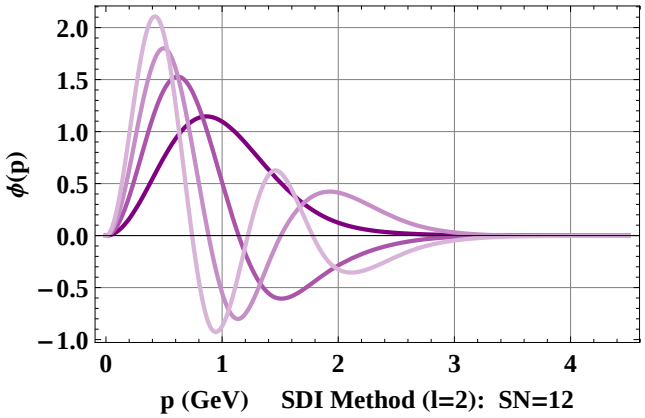

Figure B.12: SDI method: wavefunctions of d-state for the first 4 excited states: $\phi_1(p)$, $\phi_2(p)$, $\phi_3(p)$ and $\phi_4(p)$. The wavefunctions are normalized and computed for SN=12.

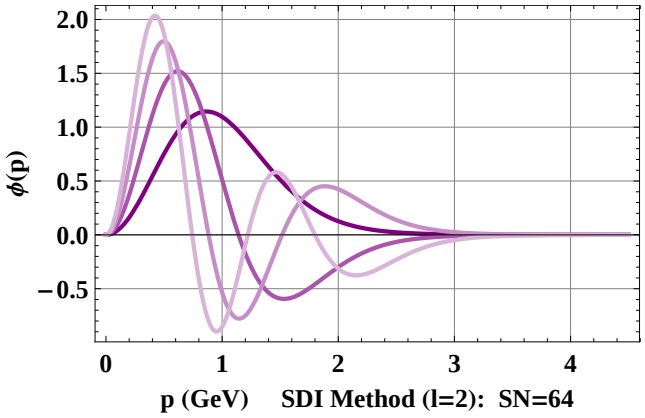

Figure B.13: SDI method: wavefunctions of d-state for the first 4 excited states: $\phi_1(p)$, $\phi_2(p)$, $\phi_3(p)$ and $\phi_4(p)$. The wavefunctions are normalized and computed for SN=64.

Eigenvalues SSI Method for the s-sates (l=0)

En	SN=8	SN=12	SN=16	SN=20	SN=24	SN=36	SN=48	SN=64	SN=128
1	2,3384020597595	2,337773115545	2,338164064854	2,33813803124	2,33812577370	2,338113158792	2,338109894513	2,3381084752377	2,3381075463083
2	4,0783737455097	4,084287309334	4,086822448649	4,08736493260	4,08760729356	4,087845067194	4,087904454220	4,0879300820659	4,0879469328103
3	5,5272928297424	5,498804704734	5,511068342230	5,51561391379	5,51766911030	5,519681269103	5,520181769503	5,5203973016507	5,5205387744622
4	6,6554600447390	6,739238924299	6,752453890811	6,76799567972	6,77580798926	6,783437674101	6,785306934805	6,7861068790652	6,7866302186971
5	7,5524534941881	7,636142464821	7,842378784548	7,89199368955	7,91424576852	7,935361390988	7,940402941359	7,9425385541273	7,9439272899154
6	10,459592591898	8,627944862582	8,719247110596	8,89078637841	8,95334530954	9,003030396867	9,014395427188	9,0191408921972	9,0221984002601
7	16,826974262827	10,51738196664	9,841122172538	9,83777108206	9,90911639081	10,00107962734	10,02396089403	10,033334689880	10,039297596080
8	18,168023938449	12,24293461056	10,98527791900	10,7655586757	10,7883564710	10,93644072286	10,97922082528	10,996290065901	11,006968757996
9		13,11660428370	11,48032440390	11,1589393730	11,3626372307	11,81100480396	11,88616692342	11,915477358823	11,933432582033
10		17,03522605846	13,51112206389	12,6083494315	12,3686364687	12,63069389829	12,74772679426	12,795934534223	12,824703724284
11		24,94569787268	15,99902764075	14,4097845614	13,7964505416	13,34479374741	13,56437270311	13,640934365945	13,685327112180
12		38,08735195186	19,14681127027	15,8380953630	14,0607560315	13,96576104115	14,33493186987	14,452326618823	14,518818928662
13			20,42071832680	16,5070815080	15,4717723668	14,91005941592	15,04360050453	15,230664133359	15,327944939007
14			23,76494675848	18,9294872384	17,3705679426	15,44406143100	15,69631140784	15,975141236720	16,114903276009
15			33,03505414184	21,7861034256	19,4996139360	16,11591208774	16,44892102567	16,684144259585	16,881448050657
16			65,37048409944	25,3636152394	21,8896009359	17,47536616144	16,77760644795	17,355187140643	17,628974506670
17				30,5476537533	21,9537583646	18,97585198445	17,50593841001	17,962779625719	18,358578030672
18				30,9623803545	24,5904615708	19,86757761730	18,61996233119	18,554420936449	19,071094472801
19				41,0782895875	27,7379872151	20,60880452996	19,53057487788	19,239777168758	19,767126309132
20				99,9770805518	31,6854156280	22,37186879457	19,85573863512	19,452243231864	20,447057201081
21					37,3459739049	24,26824254899	21,19373920056	20,264156449951	21,111056069643
22					43,8070298232	26,30142397689	22,62687248340	21,283708586909	21,759070472117
23					49,0980936327	28,48113843846	24,15228640326	21,772069498405	22,390807589672
24					141,893368671	28,64004492127	24,62172285617	22,393813234089	23,005699068231
25						30,81632229007	25,76858315342	23,580779716260	23,602849411301
26						33,32675543159	27,47653163533	24,838590398534	24,180972597116
27						36,03501662024	29,27680544985	25,791490799291	24,738067461293
28						38,98960782017	31,17229582888	26,164007880671	25,271554477172
29						42,27562408939	33,16496964121	27,555024488816	25,784622207820
30						46,10082644827	33,42594028621	29,010802915448	26,260012921457
31						47,24296722217	35,25977563756	30,530765959086	26,674097081211
32						50,94688180170	37,46005664151	32,022242408808	27,216893323699
33						57,72028280862	39,77348245237	32,115214431717	27,566697146361
34						73,07549985733	42,20582924934	33,764287018845	27,932821205853
35						95,98499884821	44,76939520409	35,479055369932	28,694492478719
36						311,4528986379	47,47604157893	37,260103751210	29,370933344316
37							49,50517787059	39,109174439459	29,517882434454
38							50,34889793270	41,027190744523	30,387516457626
39							53,41969898977	41,807614597996	31,297816420885
40							56,75087917437	43,016589614417	31,934097514400
41							60,46573058213	45,078628018387	32,245252868369
42							64,83736166129	47,216551314647	33,227513841177
43							70,37450448459	49,432062376238	34,242980573382
44							78,01031703391	51,729436465956	35,290440723612
45							82,64480619784	54,111144493008	35,318846221998
46							96,98850738747	56,582919766053	36,369004444019
47							168,5116689963	57,920535508045	37,477964342991
48							546,6941285430	59,148779293184	38,616808354336
49								61,816886185782	39,712395587161
50								64,594732950626	39,785108562655
51								67,495639941039	40,982580916630
52								70,536078096232	42,208970449409
53								73,744129039809	43,464146347649
54								77,165525363116	44,747969007243
55								80,886623384768	45,409153701050
56								85,078987299698	46,060419817532
57								86,700971990577	47,401440290919
58								90,063636616394	48,771100249235
59								96,322095056548	50,169400387601
60								104,93967761838	51,596484912218
61								128,82689572880	52,851863892962
62								145,39687716659	53,052398758874
63								296,78602988505	54,537352402478
64								962,49612288683	56,051424284341
65									57,594886897025
66									59,167844122259
67									60,770628887793
68									62,403364243158
69									62,713951329396
70									64,066443911035
71									65,760005151838
72									67,484504292894
73									69,240088939019
74									71,027280941905
75									72,846235441821
76									74,697543567036
77									76,050400858214
78									76,581366379004
79									78,498368636753
80									80,448717202324
81									82,433155204824
82									84,451857157773
83									86,505649505544
84									88,594718928927
85									90,719980225150
86									92,881640374414
87									94,583495834644

88	95,080707692533
89	97,317422489731
90	99,592892248992
91	101,90741027983
92	104,26219033137
93	106,65760742918
94	109,09499226278
95	111,57484284939
96	114,09862534720
97	116,66702011782
98	119,28166346277
99	121,27793633304
100	121,94350506540
101	124,65441819816
102	127,41575473688
103	130,22975548263
104	133,09839168225
105	136,02453143587
106	139,01115487856
107	142,06229341508
108	145,18271792289
109	148,37880341012
110	151,65889305513
111	155,03458357007
112	158,52246253766
113	161,59545418249
114	162,14740477638
115	165,94840991755
116	169,98913609604
117	174,37491434102
118	179,27056872179
119	184,89785884771
120	191,53519095890
121	199,73041377275
122	211,85220420130
123	226,53397038539
124	256,01257089367
125	341,10415390562
126	573,26379077447
127	1170,2998882305
128	3792,9741246228

Eigenvalues SDI Method for the s-sates (l=0)

En	SN=8	SN=12	SN=16	SN=20	SN=24	SN=36	SN=48	SN=64
1	2,338641911571	2,338121145436	2,338108071695	2,338107476391	2,338107319344	2,338106842481	2,338107082028	2,3381076139052
2	4,104605406173	4,088498155613	4,087975685912	4,087952262194	4,087949927110	4,087947303853	4,087948766025	4,0879494012161
3	5,636686643236	5,527016818404	5,520928028822	5,520600545822	5,520567975834	5,520558825578	5,520558192518	5,5205596161544
4	6,851432578553	6,794183309139	6,788207811763	6,787046383013	6,786786356487	6,786709863026	6,786706451331	6,7867079447365
5	8,601678802416	8,002341776532	7,956597879148	7,947219120766	7,944766321339	7,944146073199	7,944134735283	7,9441334370254
6	11,76086845608	9,626868191655	9,156257589949	9,046240808031	9,026387769003	9,022726161627	9,022656526553	9,0226512089781
7	17,40854569062	11,43507938292	10,27339451995	10,08341475071	10,04866914482	10,04051039192	10,04019998986	10,040176685550
8	32,97639062054	12,09983455352	11,14756505821	11,02755595659	11,02885416214	11,00986716602	11,00862461387	11,008533313462
9		14,99345285926	12,94173593323	12,31832339885	12,10528204098	11,94006778316	11,93634316218	11,936044261476
10		19,12242065620	15,30924859364	13,99754171539	13,13804707193	12,83900171678	12,82976902604	12,828859455181
11		26,28313014134	18,20705509677	14,48775525493	13,80088912336	13,73222294402	13,69417946922	13,691710139353
12		67,95036395969	18,70315748598	16,17722120768	15,32285244232	14,62556088101	14,53495748873	14,528387460491
13			21,84566970366	18,60985206889	17,22789329380	15,36908620543	15,35980446632	15,342090811871
14			26,66624733017	21,45802084723	19,39535669399	16,31503104652	16,16614255371	16,135714226960
15			35,08759399488	24,82803144415	19,56451247957	17,61213380809	16,94683776623	16,912121178910
16			115,8548936859	28,04345359213	21,89064227260	18,40664908020	17,80992192952	17,675088662107
17				28,94523452191	24,69982841160	19,16110202018	18,70009371661	18,428872142894
18				34,32652508943	27,91691837939	20,83139125428	19,16649971454	19,167323590164
19				43,84951474722	31,67072039365	22,66758413944	20,23175176680	19,903469145873
20				176,6162762657	36,20828892112	24,66277732512	21,57564733198	20,706508430655
21					39,49991798534	25,50973027063	22,78777278905	21,394946610965
22					42,06732653964	26,82347681845	23,05689685091	21,957743274871
23					52,58175627162	29,16009385517	24,63912273294	22,972066989127
24					250,2107495644	31,68914717595	26,33402882572	24,156337873160
25						34,43270198396	28,13731415690	24,476314141718
26						37,42110173447	30,04990248134	25,456974869430
27						40,69695958819	30,06359756293	26,829250711645
28						41,29526905298	32,07857844523	28,280740120350
29						44,32247675098	34,22549531397	29,613038905981
30						48,39330236424	36,49845055230	29,808345582528
31						53,06595029596	38,90591227139	31,410704936008
32						58,61412073538	41,45838909145	33,088357002891
33						65,58759205825	43,58484876267	34,842088675274
34						78,66728848522	44,16894455129	36,673375097803
35						86,17242399425	47,05397029790	37,888076447775
36						547,9113460738	50,13435805241	38,584210773278
37							53,43730126679	40,577082752371
38							56,99915472546	42,654980640596
39							60,87010629149	44,821425471997
40							65,12204242950	47,080525876505
41							69,86208132564	49,437055557508
42							71,94694119911	51,560013261992
43							75,25625996012	51,896561928425
44							81,57585479045	54,465509830224
45							89,35573902230	57,151472775349
46							104,6563636347	59,963390429427
47							151,1206955331	62,911914197347
48							960,9289618203	66,009885207108
49								69,272997051948
50								72,720742394388
51								75,984271354399
52								76,377782450942
53								80,27596905441
54								84,45738426603
55								88,97895976769
56								93,91954507516
57								99,39084868044
58								105,5555395127
59								112,6670856884
60								121,2273302542
61								126,3685637776
62								139,2304054680
63								266,0324623615
64								1690,959191755

Eigenvalues SDI Method for the p-sates (l=1)

En	SN=8	SN=12	SN=16	SN=20	SN=24	SN=36	SN=48	SN=64	SN=128
1	3,3629581233162	3,361313498663	3,361258899168	3,36125579460	3,36125710940	3,361258447767	3,361257886853	3,3612581587507	3,3612560529089
2	4,9275156189940	4,886359031196	4,884552338872	4,88446308413	4,88445601380	4,884455949545	4,884455574861	4,8844557966980	4,8844533142443
3	6,3685832786372	6,220271335625	6,208522363056	6,20773572329	6,20764916454	6,207627592586	6,207627360664	6,2076271225431	6,2076250027691
4	7,5189688277315	7,407860842544	7,408076087756	7,40649535405	7,40587129492	7,405674452817	7,405669742940	7,4056691183365	7,4056674604223
5	9,7047616575053	8,702469383179	8,554389205507	8,52353796862	8,51678111304	8,515269990782	8,515241309248	8,5152381797407	8,5152366739009
6	13,334877991555	10,55401665845	9,792736322343	9,59970902909	9,56431143542	9,557774056647	9,557632762803	9,5576208223840	9,5576184522207
7	19,738503317373	11,80921089448	10,68467659097	10,5699777793	10,5557022494	10,54718825874	10,54657793333	10,546530736931	10,546524790764
8	34,501949899507	13,20832214765	11,89573406856	11,5971351101	11,5492404355	11,49382623823	11,49161027856	11,491447281443	11,491429971704
9		16,51839169314	13,96058364303	13,0898022942	12,6924209925	12,40538257173	12,39978892812	12,399270428987	12,399220760086
10		21,19115669380	16,53863684009	14,5065831571	13,4469618230	13,29373105127	13,27672385744	13,275234247505	13,275099150999
11		29,50951772365	18,91284359057	15,0629480446	14,4602639780	14,19476874968	14,12737761724	14,123463154289	14,123114679939
12		69,40763713912	19,70589752745	17,2554428194	16,1910037127	15,03017615080	14,95808402957	14,947352609362	14,946497342898
13			23,68046843121	19,8584372356	18,2216408961	15,78689841586	15,77536200220	15,749873742443	15,747875657793
14			29,13122479972	22,9063051946	19,6698108141	16,91963286733	16,56455943366	16,533823876986	16,529425311978
15			39,19191572805	26,5365909168	20,5371939730	18,27909531463	17,36316957674	17,302274547424	17,292973688296
16			117,2797580413	28,2543098053	23,1510942031	18,53309107958	18,28736084688	18,059829834566	18,040075908226
17				31,0336565866	26,1249809941	19,94623171343	18,95232558939	18,807321468231	18,772071298372
18				37,1157478893	29,5465352110	21,69723046804	19,62613121439	19,537046143083	19,490127414242
19				48,8210444445	33,5732954289	23,60746814903	20,87130121792	20,298495566861	20,195275076560
20				178,022490160	38,5146347650	25,59015126005	22,27998572497	21,107703656715	20,888438223217
21					39,6992097550	25,68037148455	22,84471589466	21,634812464869	21,570460783278
22					45,1268956971	27,91950004858	23,81308682566	22,425056148299	22,242132936494
23					58,4152433890	30,34280740024	25,45102905330	23,543668227336	22,904218148385
24					251,604903867	32,96725715153	27,19752158556	24,497719333536	23,557483003271
25						35,81797365601	29,05300519075	24,796477818630	24,202730011941
26						38,92955194730	30,12289305414	26,121019696792	24,840829676831
27						41,40298135985	31,02035358638	27,532270452535	25,472733476095
28						42,35094248940	33,10391684467	29,020665003779	26,099517002173
29						46,15431087861	35,30965311862	29,653850093318	26,722553643117
30						50,45198318823	37,64504532131	30,584490633743	27,342625544607
31						55,43104690317	40,11941409074	32,223222924392	27,958659578521
32						61,43542228052	42,74429729850	33,937492422721	28,577301247933
33						69,24191134072	43,65764575910	35,728469838318	29,206391537412
34						86,35111350891	45,53407416975	37,597879451836	29,788896801603
35						87,07664964263	48,50683907317	37,934058438445	30,355188677107
36						549,2861624773	51,68579915930	39,547948133275	31,078090566386
37							55,10134334327	41,581392202073	31,697867601449
38							58,79439597590	43,701441534217	32,006706404647
39							62,82189845047	45,911879225907	32,898559141324
40							67,26609534109	48,217106329944	33,875508352572
41							72,04393285441	50,622233470003	34,427832600878
42							72,25093517793	51,612903409672	34,901197000030
43							77,97362693958	53,133200985494	35,966908559513
44							84,77506673196	55,756940380839	37,070760464934
45							93,40966786058	58,501592064182	38,201589401762
46							115,6430016560	61,376792965050	38,210814728162
47							151,2886166302	64,394064869009	39,385233972434
48							962,2945138601	67,567352029140	40,593689628587
49								70,913772080185	41,835395943866
50								74,454689859927	43,109937974578
51								76,048700386193	43,204946349665
52								78,217260661295	44,417045004259
53								82,236725163211	45,756558003072
54								86,559877819239	47,128409939453
55								91,250395628751	48,532610083858
56								96,397225332281	49,791111338768
57								102,12849723247	49,969233268867
58								108,63643000819	51,438411571092
59								116,23487445716	52,940328172701
60								125,65504377350	54,475214065553
61								126,45707964811	56,043345073902
62								153,66349823931	57,645038081564
63								266,19218199081	58,528250012764
64								1692,3179941152	59,280650232902
65									60,950577989355
66									62,655257026070
67									64,395162586993
68									66,170807713292
69									67,982745519629
70									69,831571778094
71									70,312829787870
72									71,717924002941
73									73,642483736939
74									75,605978491746
75									77,609186410730
76									79,652936107887
77									81,738109881655
78									83,865651383629
79									86,036565888671
80									86,604342430267

81	88,251925989820
82	90,512877356967
83	92,820648169616
84	95,176547870624
85	97,581984040704
86	100,03846655992
87	102,54761718488
88	105,11118550007
89	107,73105944444
90	109,90170305056
91	110,40928027531
92	113,14806441928
93	115,94981903322
94	118,81717029024
95	121,75299110262
96	124,76043427802
97	127,84297591813
98	131,00445220696
99	134,24913531271
100	137,58177111750
101	141,00769694468
102	144,53290964112
103	144,78700945865
104	148,16421802006
105	151,90934915069
106	155,77718117555
107	159,77792143999
108	163,92344895414
109	168,22759603534
110	172,70664432929
111	177,37986512131
112	182,27018757280
113	187,40513877703
114	192,81787198102
115	198,54861526689
116	200,48242031700
117	204,64653967581
118	211,17211348508
119	218,20074068383
120	225,82906236356
121	234,19013732158
122	243,51045216192
123	254,57834532423
124	298,18557832292
125	305,49117590341
126	497,84034266072
127	1048,8584287729
128	6661,8174777996

Eigenvalues SDI Method for the d-sates (l=2)

En	SN=8	SN=12	SN=16	SN=20	SN=24	SN=36	SN=48	SN=64
1	4,2520897453043	4,2483844710846	4,2481891548817	4,2481793187968	4,2481785562427	4,2481784794502	4,2481801240373	4,2481806450717
2	5,7146542994160	5,6346776567837	5,6299917579000	5,6297311671880	5,6297082656717	5,6297041986715	5,6297049114711	5,6297054942542
3	7,0406666461968	6,8865327058748	6,8705248985409	6,8691263310376	6,8689337803288	6,8688796438764	6,8688791293811	6,8688797641230
4	8,2819176886344	8,0199571254161	8,0148471554549	8,0116551446804	8,0101779583218	8,0097101850207	8,0096998323095	8,0096995132936
5	10,864255384922	9,4698747027127	9,1701084568362	9,0959735944250	9,0803072577894	9,0770626379648	9,0770044965994	9,0769996674388
6	14,936393101229	11,500189531672	10,389430028720	10,141703545272	10,095922412047	10,086751917926	10,086479360292	10,086457928488
7	22,065928867660	12,194624482697	11,149276754627	11,056751265957	11,061992857210	11,049958949156	11,048827598545	11,048744933981
8	36,077250443303	14,435449424880	12,755471993571	12,251080895536	12,104531362078	11,975383200807	11,971806772200	11,971529201401
9		18,103639236524	15,027805180369	13,905772506210	13,226340312298	12,869724807639	12,861418389443	12,860564578391
10		23,349784046507	17,812077032373	14,736883710485	13,815032240354	13,755621330509	13,722662693276	13,720321581219
11		32,776920232748	19,185321853664	15,999791380130	15,226520401205	14,655084328171	14,560575630993	14,554419912893
12		70,899877514923	21,238602125026	18,372518794560	17,096647514311	15,404057743102	15,382886402075	15,365930022950
13			25,600466014319	21,146206870456	19,244207067256	16,295810733297	16,189027981543	16,157653876801
14			31,776274310181	24,402652591047	19,834961244263	17,570787125150	16,964716973140	16,932361992311
15			43,390523731558	28,311743875143	21,686877126008	18,551239214811	17,812827868235	17,693681470302
16			118,73043061083	28,498875030036	24,445792115506	19,105462141179	18,734575356842	18,446247924679
17				33,232234067359	27,591529476822	20,759061284847	19,194818248182	19,184274782746
18				40,195993074875	31,230814423820	22,583314872145	20,203438169196	19,915417315690
19				53,948027261717	35,555178624920	24,566342087150	21,537764760003	20,713791916477
20				179,44896457868	39,926297126958	25,700828819443	22,903442760078	21,430253390817
21					40,952197163555	26,713793741570	23,019686281837	21,960083631100
22					48,603957468753	29,035512479671	24,588202351930	22,954297278943
23					64,470202102566	31,547195956281	26,277187838037	24,135151989962
24					253,01567419605	34,269697389520	28,074548426084	24,560529017260
25						37,231459245261	29,981971268603	25,429512060487
26						40,471842550234	30,205395704821	26,798221039813
27						41,534968905611	32,003193182853	28,246554863734
28						44,047022905218	34,143109306279	29,712270186251
29						48,040745671868	36,408364937129	29,771423105703
30						52,585037967489	38,807202175656	31,370534783899
31						57,903938283104	41,349838965320	33,045220528573
32						64,436172547157	43,751096608525	34,795941556058
33						73,756484340771	44,048927367490	36,624131351263
34						86,548564654683	46,920262004086	37,997872936767
35						95,921192452078	49,983829070806	38,531746985904
36						550,67170110921	53,265396005541	40,521235340853
37							56,798957624151	42,595543315277
38							60,630630006950	44,758141312196
39							64,825093880032	47,013083135586
40							69,476560130176	49,365073775558
41							72,159252128334	51,682739960233
42							74,728613484404	51,819571965328
43							80,815624547990	54,382938759052
44							88,197705391211	57,062608765525
45							98,821780207242	59,867327727024
46							127,28676660459	62,807485439265
47							151,47069917089	65,895556787725
48							963,66795531735	69,146683170174
49								72,579568077997
50								76,128740025667
51								76,217641713239
52								80,090850291380
53								84,238256473134
54								88,711981316659
55								93,583291270593
56								98,952438317887
57								104,96589660912
58								111,85647409608
59								120,09469106109
60								126,55940163194
61								132,14741265105
62								169,05005962257
63								266,36257513236
64								1693,6826217631

Appendix C

Numerical procedure to solve the NRSE in r-space

In order to solve the NRSE in r-space for a Pure linear potential,

$$-\frac{d^2u_{nl}}{d\rho^2}+\left[\frac{l(l+1)}{\rho^2}+\rho\right]u_{nl}=\varepsilon_{nl}u_{nl}\,, \tag{C.1}$$

we made use of the simple Finite difference method, by approximating the second derivative of Eq.C.1, by

$$\frac{d^2u_{nl}}{d\rho^2}\equiv u_i^{''}=\frac{u_{i-1}-2u_i+u_{i+1}}{h^2}, \tag{C.2}$$

where h is the incrementation step. We discretized the variable ρ such that

$$\rho_i=-Nh+10; \qquad N=-npt+1,-npt+2,...npt-2,npt-1; \qquad i=1,2,...npt. \tag{C.3}$$

where npt is the number of points of our mesh (we used $npt=2000$). The choice of the mesh was motivated by the knowledge that the wavefunctions go to zero when ρ goes to infinity. From a practical point of view, this limit is already achieved when $\rho=10$.

This way we were able to find a set of $2N+1$ unknowns for $2N+1$ equations:

$$-\left[\frac{u_{i-1}-2u_i+u_{i+1}}{h^2}+\frac{l\,(l+1)}{\rho_i^2}+\rho_i\right]=\varepsilon u_i \tag{C.4}$$

which is a matrix problem, that can be easily solved by diagonalizing the matrix and finding the eigenvalues ε and the corresponding eigenvectors $u=(u_0,u_1,...,u_{2N+1})$.

The problem for the Pure Coulomb-type Potential, Eq.2.28 was solved in a completely analogue way. We just modified Eq.C.4 in order to be consistent with this new potential.

Bibliography

[1] F. Jegerlehner, A. Nyffeler, Phys.Rept. **477**, 1–110 (2009)

[2] B. Friman, C. Höhne, J. Knoll, S. Leupold, J. Randrup, R. Rapp, *The CBM Physics Book: Compressed Baryonic Matter in Laboratory Experiments. Lecture Notes in Physics* (Springer,2011)

[3] F. Gross, J. Milana, *Covariant, chirally symmetric, confining model of mesons*, Phys. Rev. D **43**, 2401 (1991)

[4] F. Gross, *Three-Dimensional Covariant Integral Equations For Low-Energy Systems*, Phys. Rev. D **186**, 1448 (1969)

[5] F. Gross, *Relativistic few-body problem. I. Two-body equations*, Phys. Rev. C **26**, 2203 (1982)

[6] F. Gross, *Relativistic few-body problem. II. Three-body equations and three-body forces*, Phys. Rev. C **26**, 2226 (1982)

[7] A. Stadler, F. Gross, *Covariant Spectator Theory: Foundations and Applications*, Few-Body Syst. **49**, 91 (2011)

[8] F. Gross, J. Milana, *Decoupling confinement and chiral symmetry breaking: An explicit model*, Phys.Rev. D **45**, 969 (1992)

[9] F. Gross, J. Milana, *Goldstone pion and other mesons using a scalar confining interaction*, Phys.Rev. D **50**, 3332 (1994)

[10] C. Savkli, F. Gross, *Quark-antiquark bound states in the relativistic spectator formalism*, Phys.Rev. C **63**, 035208 (2001)

[11] P. Higgs, *Broken Symmetries and the Masses of Gauge Bosons* Physical Review Letters **13**, 508 (1964)

[12] S. Neddermeyer, C. Anderson, *Note on the Nature of Cosmic-Ray Particles*, Phys. Rev. **51**, 884 (1937)

[13] C. M. G. Muirhead, H. Occhialini ,C. M. G. Powell, *Processes Involving Charged Mesons Lattes*, C. F. Nature **159**, 694 (1947)

[14] G. S. Adams, et al., Phys. Rev. Lett. **81**, 5760 (1998)

[15] M. Alekseev, et al., Phys. Rev. Lett. **104**, 241803 (2010)

[16] $http://www.gluex.org$

[17] $http://www-panda.gsi.de/framework/index.php$

[18] $http://www.gsi.de/fair/overview/accelerator/index.html$

[19] C. Amsler, et al., Phys. Lett. B **639**, 165 (2006)

[20] A. Abele, et al., Phys. Lett. B **446**, 349(1999)

[21] D. J. Griffiths, *Introduction to Quantum Mechanics*, 2nd Edition (Willey, 2005)

[22] K. Nakamura et al. (Particle Data Group), *PDG Live Particle Summary Quarks (u, d, s, c, b, t, b', t', Free)*. Particle Data Group. Retrieved 2011-08-08

[23] N. Fabiano, *Top Mesons*, Eur.Phys.J.C **2**, 345 (1998)

[24] Y. Ikeda, H. Iida, *The potential from Bethe-Salpeter amplitudes on lattice*, Proceedings of Science, The XXVIII International Symposium on Lattice Field Theory, Lattice 2010 June 14-19, 2010 Villasimius, Italy, (2010)

[25] E. Hairer, S. Nørsett, G. Wanner, *Solving ordinary differential equations I: Nonstiff problems*, Berlin, (New York: Springer-Verlag, 1993)

[26] $http://pdg.lbl.gov/2012/tables/contents_tables_mesons.html$

[27] R. H. Landau, Phys. Rev. C **27**, 2191 (1983)

[28] A. Martin, *A fit of upsilon and charmonium spectra*, Phys. Lett. B **93**, 338 (1980)

[29] E. Eichten, K. Gottfried, T. Kinoshita, K. D. Lane, T. M. Yan, *Charmonium: The model*, Physical Review D **17**, 3090 (1978)

[30] J. L. Richardson, *The heavy quark potential and the upsilon, J / psi systems*, Phys. Lett. B **82**, 272 (1979)

[31] C. W. Bernard et al., *The static quark potential in three flavor QCD*, Phys.Rev. D **62**, 034503 (2000)

[32] E. Eichten et al., *The spectrum of charmonium*, Phys. Rev. Lett. **34**, 369 (1975)

[33] F. Gross, J. W. Van Orden, and K. Holinde, Phys. Rev. C **41**, R1909 (1990).

[34] C. D. Roberts, R. T. Cahill, J. Praschifka, Ann. Phys. (N.Y.) **188**, 20 (1988)

[35] F. Gross, *Relativistic Quantum Mechanics and Field Theory*, (Willey -InterScience, 1999)

[36] S. Godfrey, N. Isgur, Phys. Rev. D **32**, 189 (1985)

[37] Y. Nambu, G. Jona-Lasinio, Phys. Rev. **122**, 345 (1964); Phys. Rev. **124**, 246 (1961)

[38] M. Uzzo, F. Gross, *Stability of the spectator, Dirac, and Salpeter equations for mesons*, Phys. Rev. C **59**, 1009 (1999)

[39] E. Biernat, F. Gross, T. Peña, A. Stadler, *Scalar-Particle Self-Energy Amplitudes and Confinement in Minkowski Space*, Few-Body Systems, 2012 .